UCID-19650

Throttle Coil Operation of TMX-U

D. L. Correll, J. A. Byers, T. A. Casper, F. H. Coensgen,
R. H. Cohen, W. F. Cummins, C. C. Damm, J. H. Foote,
D. P. Grubb, E. B. Hooper, Jr., B. G. Logan, Y. Matsuda,
A. W. Molvik, W. E. Nexsen, M. E. Rensink, T. D. Rognlien
T. C. Simonen, G. R. Smith, W. C. Turner, and R. L. Wong

Manuscript date: January 1983

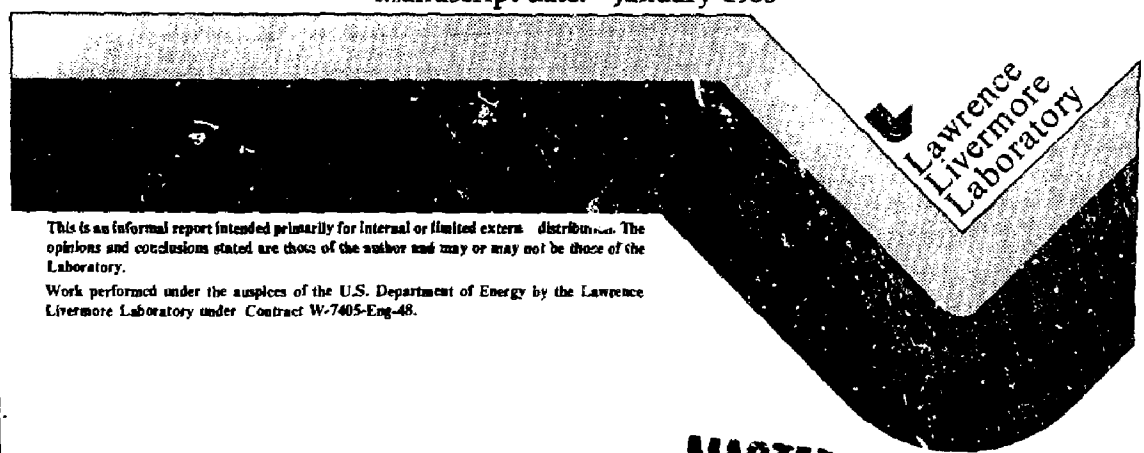

UCID-19650

UCID--19650

DE83 009801

THROTTLE COIL OPERATION OF TMX-U

D. L. Correll, J. A. Byers, T. A. Casper, F. H. Coensgen, R. H. Cohen, W. F. Cummins, C. C. Damm, J. H. Foote, D. P. Grubb, E. B. Hooper, Jr., B. G. Logan, Y. Matsuda, A. W. Molvik, W. E. Nexsen, M. E. Rensink, T. D. Rognlien, T. C. Simonen, G. R. Smith, W. C. Turner, and R. L. Wong

January 1983

THROTTLE COIL OPERATION OF TMX-U

ABSTRACT

A tandem-mirror configuration with an axisymmetric central cell, similar to the geometry of MARS (Mirror Advanced Reactor Study) or the Kelley-TDF mode of MFTF-B, can be generated by inserting a 6-tesla, throttle coil in each end of the TMX-U central cell. The throttle coil geometry of TMX-U will test the physics issues associated with axisymmetric tandem-mirror reactors, such issues as (a) increased radial confinement time for central-cell ions confined by axisymmetric mirror cells and electrostatic potentials, (b) theoretical limits set by the trapped particle instability for the required passing density between the central cell and the end-cell anchor, and (c) pumping of trapped particles within the thermal barrier and transition regions with methods other than neutral beams. The central-cell plasma parameters for the throttle coil geometry are evaluated for two operating points. The first requires heating hardware (neutral beams and ECRH) and vacuum performance at the TMX-U proposal level, yielding plasma parameters, central-cell betas, and plasma confinement exceeding those of the original TMX-U proposal. The second operating point, requiring approximately half the ECRH end-cell performance of the first, is predicted to equal the beta and to exceed the plasma pressure and confinement time of the central cell in the standard TMX-U geometry.

THROTTLE COIL OPERATION OF TMX-U

CONTENTS

LIST OF FIGURES

LIST OF TABLES

1. INTRODUCTION

D. L. Correll

Comparative studies[1.-1] of end plug configurations for tandem mirror fusion reactors with thermal barriers led to the selection of the axicell[1.-2] configuration as the reactor geometry for further detailed design.[1.-3] Both the engineering[1.-4] and physics[1.-5] aspects of converting MFTF-B from an A-cell to an axicell geometry have been documented.

The purpose of this present document is to discuss the physics issues of adding a 6-tesla axisymmetric-coil insert (see Fig. 1 -1) to both ends of the central cell of TMX-U.[1.-6] This throttle coil insert also includes an accompanying low-field transition coil to minimize the geodesic curvature of the transition between the central cell and end cell. Smaller geodesic curvature will in turn lower the amplitude of parallel current in equilibrium and reduce the resonant-particle radial transport associated with the quadrupole magnetic fields within the transition. The throttle coil geometry will not only improve the axial confinement of the central cell by the electrostatic enhancement factor exp $(\frac{\phi}{T})$ but also will reduce radial losses, associated with nonsymmetric magnetic fields, by the axisymmetric mirror ratio R_{Th}. The axial magnetic-field profile for the throttle coil geometry is given in Fig. 1 -2.

The objectives of the TMX-U throttle coil experiment are:

- To generate data bases relevant to axicell tandem mirrors: radial transport, MHD equilibrium, low-frequency stability, and microstability.
- To demonstrate improved central-cell performance by both axisymmetric-mirror and electrostatic confinement.
- To evaluate thermal-barrier end-cell power requirements for tandem mirrors with throttle coils.

The throttle coil geometry will allow future investigations into methods of trapped particle pumping other than neutral beams.

The central cell length for the throttle geometry is equal to the axisymmetric section of the standard geometry. This design constraint precluded the addition of a complete axicell, similar to MFTF-B and to Mirror Advanced Reactor Study (MARS), for TMX-U. More recent geometries for the MARS

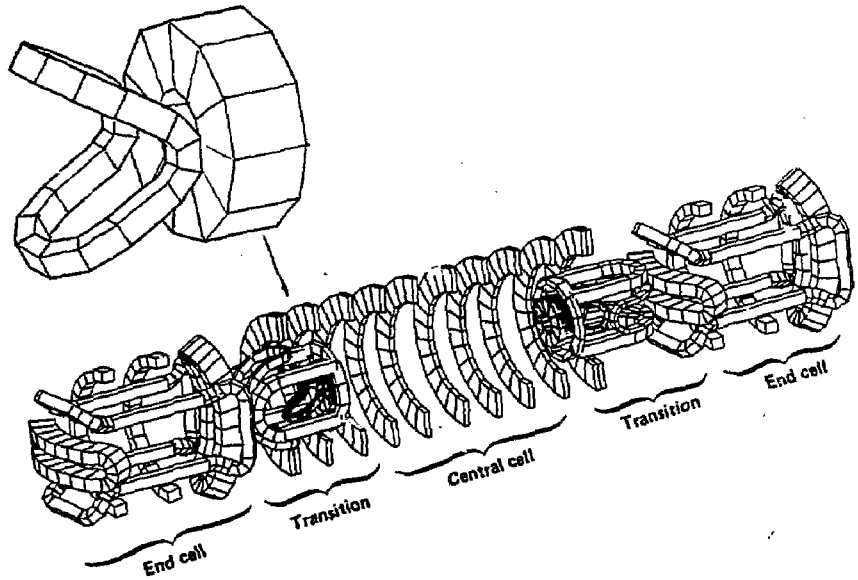

Fig. 1 -1. The TMX-U magnet set with throttle coil insert.

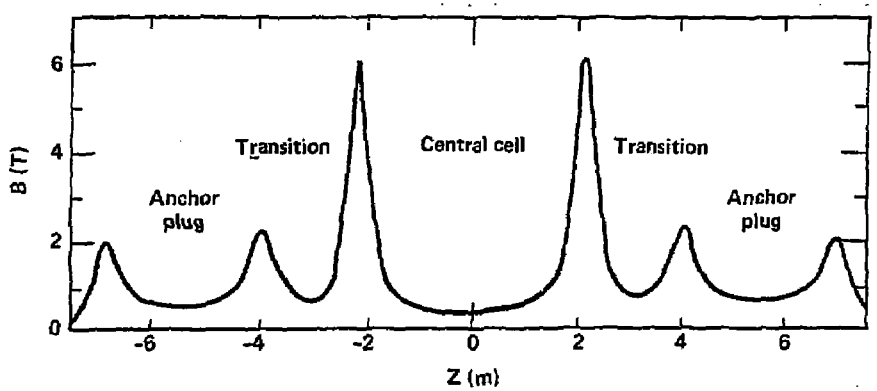

Fig. 1 -2. Axial magnetic field profile for throttle coil geometry of TMX-U.

study use a throttle coil exclusively. As seen in Fig. 1 -3, the axial magnetic-field profile for the throttle geometry is very similar to the Kelley-TDF mode of MFTF-B. The plasma potential (ϕ) and density (n) profiles for the throttle coil geometry and standard geometry of TMX-U will qualitatively be the same as the previously calculated Kelley-TDF and TMX-U operating modes of MFTF-B (see Fig. 1 -3).

Generation of a potential bump in the TMX-U central cell that is similar to the axicell bump in the MARS mode of MFTF-B will not be possible. The throttle coil geometry however, will allow investigation of most physics issues required for the design of a thermal-barrier tandem reactor incorporating axisymmetric geometries. These physics issues are addressed individually in Section 3 of this document. Reference 1.-5, entitled Physics Basics for an Axicell Design for the End Plugs of MFTF-B, presents a detailed introduction to the theory of these physics constraints. Section 3 does not include issues already being tested in TMX-U, issues such as, (a) start-up and generation of hot, mirror-confined electrons, (b) electron microstability, (c) hot electron stability (MHD), and (d) ion microstability of the end cells. These topics are reviewed in Section 2.3. Table 1 -1 lists the axicell physics issues addressed in Section 3, the means of control, and the theoretical limits expected in the TMX-U throttle coil geometry.

The central-cell physics parameters in Section 2.2 of this report were arrived at by satisfying the constraints of particle and power balance (see Appendix A), by meeting the theoretical limits given in Table 1 -1, and utilizing the neutral beams, the ICRH, and the ECRH that were available on TMX-U. With respect to neutral-beam heating of the central cell, we compare in Table 1 -2 the standard geometry reference cases A and B with cases C and D having TMX-U throttle coil geometry. Case C requires heating hardware (neutral beams and ECRH) and vacuum performance at the TMX-U proposal level that will yield plasma parameters, central-cell betas, and plasma confinement exceeding those of the original TMX-U proposal. Case D performance, requiring approximately half the ECRH end-cell performance of Case C, equals the predicted beta and exceeds the plasma pressure and confinement time for the central cell with the standard geometry of TMX-U.

The most obvious improvement in the throttle geometry compared to the standard geometry is the increase in the radial confinement, $(n\tau)_{ic}^{radial}$, because of the reduction in the number of central-cell

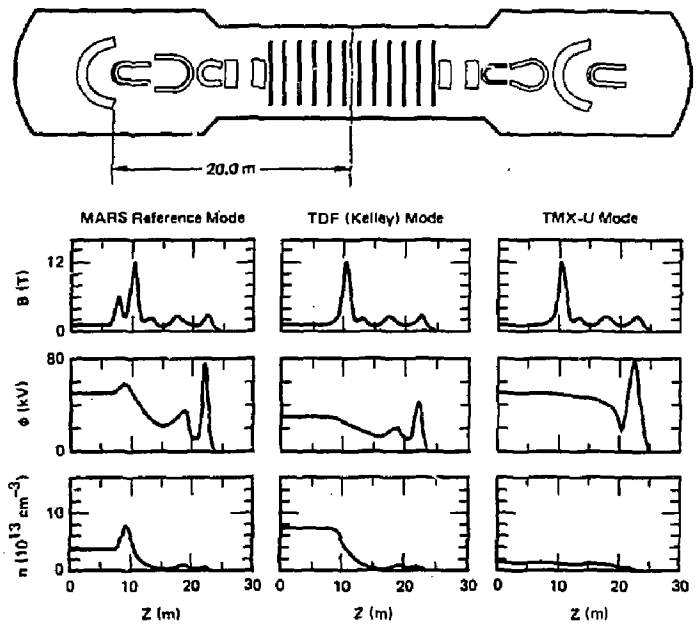

Fig. I -3. Magnetic field strength (B), plasma potential (ϕ), and plasma density (n) profiles for the three modes of operation of MFTF-B.

Table 1 -1. Physics issues of axisymmetric tandem mirrors.

Section	Means of Control	Theoretical Scaling for Case C	Reference Case C Parameters
3.1 MHD stability	$\beta_c \propto \beta_e^{-2}$ $\beta_A \propto \beta_e^{hot}$	$\beta_c < 1.2\ \beta_A$	$\beta_c = 0.5$ $\beta_A = 0.4$
3.2 Parallel currents	B_c (T) κ, Geodesic curvature	$J_c^{\parallel}\ (A/cm^2) = 20\left(\frac{0.3}{B_c}\right) \times \left(\frac{\int \kappa ds}{0.2}\right)$	$B_c = 0.4$ T $\int \kappa ds \leq 0.2$
3.3 Electrostatic ballooning	$n_{pass} \propto \frac{1}{\beta_{Th}}$	$n_{pass} > \frac{n_c}{25}$	$\frac{\beta_A \beta_{Th}}{\beta_c^2} > 20$ $\beta_{Th} \leq 6$ T
3.4 Central-cell micro-stability	I_{beam}, I_{gas}, θ_{inj}	$f(v_{\parallel})$ monotonic Pitch-angle width > 22°	$I_{gas} = 2$ amps $\theta_{inj} = 65°$ $B_c = 0.5$
3.5 Radial transport	E^r (V/cm)	$\tau_{Ic}^{\perp}$ (s) = 0.5 $\frac{100}{E^r}$	$E^r < 100$ V/cm
3.6 Trapped-particle pumping	n_{pass} (cm^{-3}) T_{pass} (keV)	I^{pump} (A) = 100 $\times \left(\frac{n^{pass}}{2 \times 10^{13}\ T_{pass}^{3/2}}\right)$	$n_{pass} = 1.2 \times 10^{13}$ $T_{pass} > 1$ keV
3.7 Drift surfaces/ adiabaticity	$E^r \times B$ drift $E_{\perp}$ (keV) θ_{inj}	closed $r_A^{drift} < 26$cm $\tau_A^{adiabatic}$ (s) = 60 exp $\left[\frac{-4}{3}\ v\ (10^8 cm/s)\right]$	$r_A = 25$ cm $v \approx 10^8$cm/s (10 keV D^+)

Table 1-2. Central-cell parameters for TMX-U.

Parameter	Standard Geometry		Throttle coil geometry	
	Case A	Case B	Case C	Case D
Plasma Species	H_2	D_2	D_2	D_2
Density, n_{ic} ($10^{13}cm^{-3}$)	1.7(warm), 0.6(hot)	3.1	4.0	3.0
Ion Energy, E_{ic} (keV)	1.4(warm), 4.7(hot,$\perp$)	2.0	5.5	3.0
Ion Temp., $T_{ic}^{\perp}$, $T_{ic}^{\parallel}$ (keV)	0.9, 0.9(warm)	1.5, 1.0	4.3, 2.4	2.3,1.4
Electron Temp., T_{ec} (keV)	0.6	0.35[a]	0.7[a]	0.5[a]
Magnetic Field, B_c, B_c^{mirror} (T)	0.3, 2.0	0.3, 2.0	0.4, 6.0	0.4,6.0
Ion Beta, β_{ic} ($\perp$)	0.07(warm), 0.13(hot)	0.21	0.43	0.23
Total Beta, β_c ($\perp$)	0.26	0.26	0.50	0.27
Confining Potential ϕ_{ic} (kV)	2.2	2.2	2.2	2.2
Central Cell Potential ϕ_{ec} (kV)	2.6	1.6	3.1	2.3
Axial Confinement, $(n\tau)_{ic}^{axial}$ ($10^{11}cm^{-3}\cdot s$)	10	12	11	11
Radial Confinement, $(n\tau)_{ic}^{radial}$ ($10^{11}cm^{-3}\cdot s$)	5	6.7	200	60
Pumping Confinement, $(n\tau)_{ic}^{pumping}$ ($10^{11}cm^{-3}\cdot s$)	3	4	50	13
Total Confinement, $(n\tau)_{ic}^{total}$ ($10^{11}cm^{-3}\cdot s$)	(3.3)[b]	2.1(4.3)[b]	8.6[b]	5.4[b]
Beam Current, I_{beam}^{incid}, I_{beam}^{ioniz} (Atom A)	180, 27	180, 37	170, 22	90,10
Gas Feed, I_{gas}^{c-x}, I_{gas}^{ioniz} (Atom A)	84, 42	170, 57	6, 2	39,13
Plasma Radius & Length, r_c, L_c (cm)	26, 510	22, 510	17, 260	17,260
Plasma Density at B_c^{mirror}, $n_{passing}^{mirror}$ ($10^{13}cm^{-3}$)	not calculated	2.2	1.2	1.5
Passing Temp. at B_c^{mirror}, $T_{passing}^{mirror}$ (keV)	not calculated	0.6	1.3	1.0

[a]Does not include additional power input to the central-cell electrons through the end-cell electrons from ECRH.

[b]Values in parentheses are without pumping losses $(\tau_{ic})^{-1} = (\tau_{ic}^{axial})^{-1} + (\tau_{ic}^{radial})^{-1}$. Values with no parentheses include pumping losses, $(\tau_{ic})^{-1} = (\tau_{ic}^{axial})^{-1} + (\tau_{ic}^{radial})^{-1} + (\tau_{ic}^{pumping})^{-1}$.

ions that experience radial resonant transport associated with nonsymmetric (quadrupole) magnetic fields. The throttle coil magnetically confines approximately $(1-\frac{1}{2R_{Th}})$ fraction of the central cell ions to axisymmetric field regions. Only electrostatically confined central-cell ions experience any quadrupole fields. Thus the central-cell ions confined to the machine, i.e., those not lost axially at the Pastukhov confinement rate, $(n\tau)_{ic}^{axial}$, fall into two classes: first, ions magnetically trapped between the two throttle coils (trapped population) and second, ions electrostatically stoppered between the peak end-cell potentials (passing population).

Ion-particle losses from the central-cell passing population that are either collisionally trapped or are charge-exchange pumped within the end cell and transition cell are known as pumping losses. Because only the passing population is subject to the pumping losses, the effective confinement parameter, $(n\tau)_{ic}^{pumping}$, for the total central cell ions (trapped plus passing) is larger than the pumping confinement parameter of the passing-particle population by a factor, $\frac{n_{ic}}{n_{ic}^{passing}} \simeq 2R_{Th}$.

Improvements in density and ion energy give higher central-cell plasma pressure, which demands the central-cell magnetic field change from 0.3 to 0.4 T to meet MHD beta limits. Figure 1 -4 gives the axial variation of B, ϕ, and n that corresponds to Case C of the throttle coil geometry.

Unlike Kelley-TDF scenarios where $T_{ic}^{\perp} > T_{ic}^{\parallel} \simeq \phi_{ic}$, in the MARS mode of MFTF-B and in reactor scenarios where central-cell ion confinement is on the order of 100 times the ion-ion collision times, the improvement in central-cell confinement by mirror effects must be replaced solely by electrostatic confinement, where $T_{ic}^{\perp} \simeq T_{ic}^{\parallel} < \phi_{ic}$. The throttle geometry could address physics issues associated with the

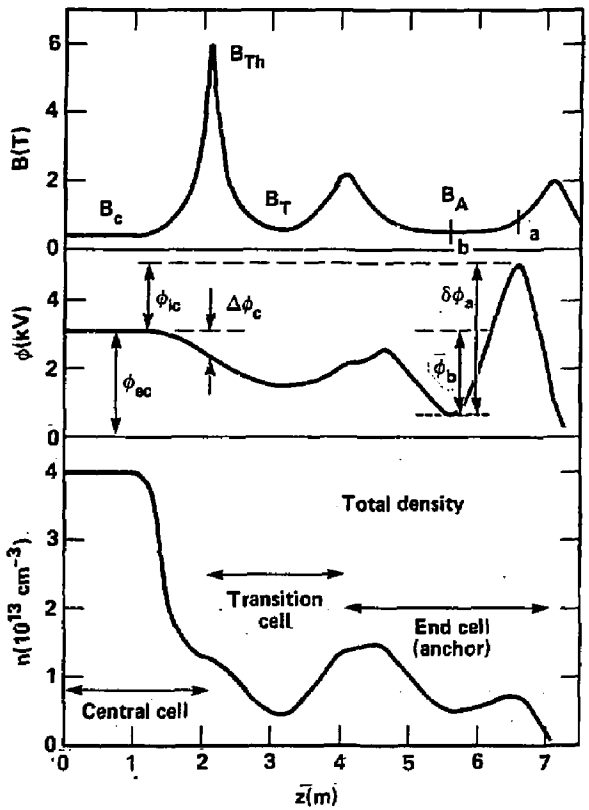

Fig. 1 -4. Axial profiles of B, ϕ, and n for case C of the TMX-U coil geometry.

ion-velocity distributions of the central cell that are expected for the MARS mode, if ICRF heating and neutral gas fueling are used in the central cell instead of neutral beams. The relative number of mirror trapped and electrostatically stoppered ions would differ from the previously discussed throttle coil Kelley-TDF modes and the passing population would become more dominant.

The throttle coil geometry could also be operated in the "standard TMX-U geometry" mode of MFTF-B where the central-cell density is constant through the transition by not pumping the transition region. Thus, all three modes of MFTF-B (see Fig. 1 -3) can be operated in the throttle geometry.

The remaining two sections of this document provide detailed analyses of the plasma parameters and operating modes (Section 2) and give theoretical background on the physics issues of a thermal-barrier tandem-mirror reactor that are addressable in the throttle coil geometry of TMX-U (Section 3).

REFERENCES

1.-1. G. A. Carlson, W. L. Barr, B. M. Boghosian, R. S. Devoto, J. N. Doggett, G. W. Hamilton, B. M. Johnston, W. N. Komai, J. E. Lee, B. G. Logan, R. W. Moir, W. S. Neff, and R. B. Campbell (TRW, Inc.), Comparative End-Plug Study for Tandem Mirror Reactors, LLNL Report, UCID-19271, (1981).

1.-2. J. Kesner, Nuclear Fusion 20 557 (1980).

1.-3. C. D. Henning et al., Mirror Advanced Reactor Study - Interim Design Report, LLNL Report, UCRL-53333 (March 1983).

1.-4. K. I. Thomassen and V. N. Karpenko, An Axicell Design for the End Plugs of MFTF-B, LLNL Report, UCID-19318, (1982).

1.-5. D. E. Baldwin and B. G. Logan, Physics Basis for an Axicell Design for the End Plugs of MFTF-B, LLNL Report, UCID-19359 (1982).

1.-6. F. H. Coensgen, T. C. Simonen, A. K. Chargin and B. G. Logan, TMX-U Major Project Proposal, LLNL Report, LLL-Prop-172 (April 1980).

2. PLASMA PARAMETERS AND OPERATING MODES

2.1. OPTIMIZATION OF MAGNETIC FIELD GEOMETRY

C. Damm and R. Wong

The geometry of the design for the throttle coil magnet is based on a set of constraints aimed primarily at controlling the cost and schedule for the modifications. The first constraint is that the overall machine length should remain the same. This eliminates costly pit extension and vacuum-chamber rework. The second constraint is that the end plugs, with associated neutral beams and ECRH equipment, should be used as they exist. This ensures that end-plug plasmas can be generated without additional ECRH or neutral beam capability and without costly relocation of injection ports. The third constraint is that the plasma radial size should remain about the same as in the present TMX-U, $r_p \approx 15$ cm, with a halo extending to $r_p \approx 25$ cm. This ensures the adequacy of the heating systems, brackets the vacuum requirements at the present level, and sets the size of the flux bundle that must clear any insert coils.

With these constraints, insertion of a full axicell at each end of the TMX-U central cell reduces the central-cell to an insignificant length. However, insertion of a single axisymmetric coil at each end leaves room for a reasonable central cell and this geometry was adopted. The bore of the high-field solenoid is chosen to clear the $r_p = 23$-cm flux bundle with $B_{Th} = 2.2$ T (see Fig. 2.1-1). At this field, $B_{Th} = B_A^{im}$ and, with the present value of the central field $B_c = 0.3$ T, the fraction of central-cell ions passing to the anchor will be the same as in TMX-U. This gives a tie-in of performance, including trapped particle effects, to the present operation. Improved performance by reduction of the passing-ion fraction requires increasing B_{Th}. A maximum field strength of 6 T was selected for the reference case. This makes TMX-U a half-field version of MFTF-B. At this field, the flux bundle with $r_p = 25$ cm easily clears the bore.

While a central field strength of $B_c = 0.3$ T provides a tie-in to present TMX-U operation, higher central fields help to meet trapped-particle-mode stability requirements (Sec. 3.3). Higher fields also allow confinement of higher plasma pressures, within the constraints of MHD ballooning limits (Sec. 3.1). Because the existing central-cell beams are

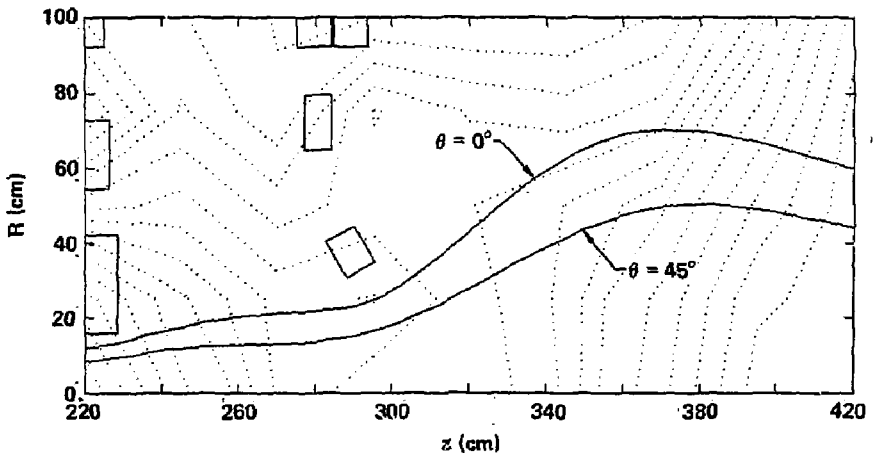

Fig. 2.1 -1. Projection of flux lines on the $\theta = 0^{o}$ plane for r_p = 23 cm and B_{Th} = 2.2 T. Clearance to the throttle coil conductor bundle located at z = 220 cm leaves room for coil casing and lead box. The section of the second transition quadrupole is at z = 290 cm.

adequate to sustain higher plasma pressure with the improved confinement predicted for the throttle coil geometry, a reference case value of B_c = 0.4 T was selected as best meeting the several stability and performance requirements. Variation of B_c between 0.3 and 0.5 T (the maximum attainable) will then aid testing of the stability criteria.

The field design now reduces to an optimization of the transition between anchor and throttle coils so as to maintain adequate MHD stability with minimum geodesic curvature. The physics basis for this optimization is identical to that described by Baldwin and Bulmer[2.1.-1].

The MHD-stability requirement is set as a minimum to match the present TMX-U reference case at β_c = 0.25, for β_p = 0.33. The goal for the geodesic curvature is to reduce the net value integrated over the transition region to zero. A quadrupole pair similar to the MFTF-B transition was tried for TMX-U but with that geometry, net-zero geodesic curvature could only be achieved by lengthening the transition and hence reducing the central-cell length to an unacceptable value. Instead, the existing transition coil is retained and the geodesic curvature minimized by the addition of a second smaller quadrupole adjacent to the throttle coil (Fig. 1.-1). Quadrupole currents in this magnet oppose those in the large transition coil, thus providing a local reversal in geodesic curvature and the desired reduction in net value. The coil shape and optimum transition-coil currents were determined by successive trials, using the EFFI code to calculate the fields and the TEBASCO code to evaluate normal and geodesic curvatures, parallel currents, and MHD stability. While the geodesic curvature could not be completely zeroed with the constraints imposed, the improvements in performance predicted by theory for the reference design are substantial as will be seen in subsequent sections. With this coil arrangement, the central-cell length is 4 m between throttle-field peaks, a length approximately equal to the axisymmetric part of the TMX-U central cell in the absence of a throttle coil. A plot of the r_p = 15 cm flux bundle is shown in Fig. 2.1-2.

Reference

2.1.-1. D. E. Baldwin and R. H. Bulmer, A Physics Conceptual Design for the MFTF-B Transition Coil, LLNL Report, UCID-19562 (August 1982).

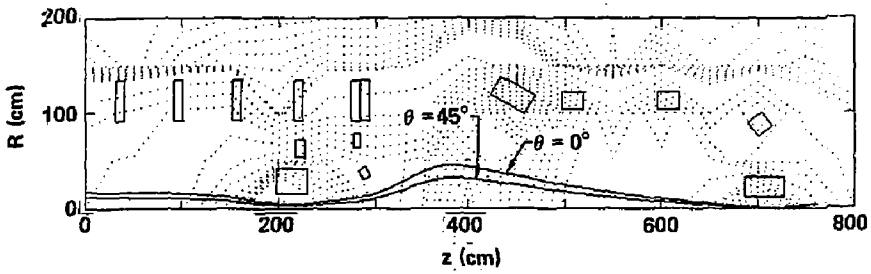

Fig. 2.1 -2. Projection of flux lines on the $\theta = 0^{o}$ plane for r_p = 15 cm and B_{Th} = 6 T (reference case). The center of the central cell is at z = 0.

2.2. OPTIMIZATION OF THE KELLEY TDF MODE

D. L. Correll and M. E. Rensink

Reference Case

Table 2.2-1 compares the TMX-U central-cell-plasma parameters for the throttle coil and for the standard geometry. Case A is the original thermal-barrier reference case of the TMX-U proposal (see Ref. 2.2-1, Table A2-1, p. A-21). The analytically derived parameters of Case A can be compared to the Fokker-Planck derived values given in Case B. The Case A plasma is hydrogen and the Case B plasma is deuterium because improved operation of TMX-U has been observed with deuterium. Case C is the throttle coil reference case, which requires ECRH, neutral beams, and vacuum performance at the level of the TMX-U proposal. Using the same ion-confining potential (ϕ_{ic}) and electron temperature (T_{ec}) as in Cases A and B, we ran the Fokker-Planck code[2.2-2] with a central-cell mirror ratio of 15 (B_c = 0.4 T and B_{Th} = 6 T), with radial losses, as well as pumping losses, being applied only to the passing population. For the total central-cell population, the confining parameter resulting from passing-particle losses is larger than $\tau_{passing}$ by the ratio $n_{ic}/n_{ic}^{passing}$ evaluated at the midplane. Also included in the loss boundary (see Fig. 2.2-1) in Case C was a potential drop, $\Delta\phi_c$ = 0.8 keV, from the central-cell midplane to the central-cell mirror throat. Case D, the other reference case for the throttle coil geometry, requires approximately half the ECRH end-cell performance and half the central-cell beam current as Case C. Because of the larger fraction of passing particles, the loss boundary for Case D's was defined with $\Delta\phi_c = 0$.

Compared to Case B the throttle coil geometry of Case C, as predicted by Fokker-Planck analysis, will show a 30% increase in density, a 200% increase in beta, a 275% increase in ion temperature, and a total central-cell confinement parameter four times larger $\left[(n\tau)_{ic}^{total} = 8.6 \times 10^{11}\ cm^{-3} \cdot s\right.$ compared to the standard geometry value of $\left.(\frac{1}{12} + \frac{1}{6.7} + \frac{1}{4})^{-1} \times 10^{11} = 2.1 \times 10^{11}\ cm^{-3} \cdot s\right]$.

Table 2.2-1. Central-cell parameters for TMX-U.

Parameter	Standard Geometry		Throttle coil geometry	
	Case A	Case B	Case C	Case D
Plasma Species	H_2	D_2	D_2	D_2
Density, n_{ic} ($10^{13}cm^{-3}$)	1.7(warm), 0.6(hot)	3.1	4.0	3.0
Ion Energy, E_{ic} (keV)	1.4(warm), 4.7(hot,$\perp$)	2.0	5.5	3.0
Ion Temp., $T_{ic}^{\perp}$, $T_{ic}^{\parallel}$ (keV)	0.9, 0.9(warm)	1.5, 1.0	4.3, 2.4	2.3,1.4
Electron Temp., T_{ec} (keV)	0.6	0.35[a]	0.7[a]	0.5[a]
Magnetic Field, B_c, B_c^{mirror} (T)	0.3, 2.0	0.3, 2.0	0.4, 6.0	0.4,6.0
Ion Beta, β_{ic} ($\perp$)	0.07(warm), 0.13(hot)	0.21	0.43	0.23
Total Beta, β_c ($\perp$)	0.26	0.26	0.50	0.27
Confining Potential ϕ_{ic} (kV)	2.2	2.2	2.2	2.2
Central Cell Potential ϕ_{ec} (kV)	2.6	1.6	3.1	2.3
Axial Confinement, $(n\tau)_{ic}^{axial}$ ($10^{11}cm^{-3}\cdot s$)	10	12	11	11
Radial Confinement, $(n\tau)_{ic}^{radial}$ ($10^{11}cm^{-3}\cdot s$)	5	6.7	200	60
Pumping Confinement, $(n\tau)_{ic}^{pumping}$ ($10^{11}cm^{-3}\cdot s$)	3	4	50	13
Total Confinement, $(n\tau)_{ic}^{total}$ ($10^{11}cm^{-3}\cdot s$)	(3.3)[b]	2.1(4.3)[b]	8.6[b]	5.4[b]
Beam Current, I_{beam}^{incid}, I_{beam}^{ioniz} (Atom A)	180, 27	180, 37	170, 22	90,10
Gas Feed, I_{gas}^{c-x}, I_{gas}^{ioniz} (Atom A)	84, 42	170, 57	6, 2	39,13
Plasma Radius & Length, r_c, L_c (cm)	26, 510	22, 510	17, 260	17,260
Plasma Density at B_c^{mirror}, $n_{passing}^{mirror}$ ($10^{13}cm^{-3}$)	not calculated	2.2	1.2	1.5
Passing Temp. at B_c^{mirror}, $T_{passing}^{mirror}$ (keV)	not calculated	0.6	1.3	1.0

[a]Does not include additional power input to the central-cell electrons through the end-cell electrons from ECRH.

[b]Values in parentheses are without pumping losses $(\tau_{ic})^{-1} = (\tau_{ic}^{axial})^{-1} + (\tau_{ic}^{radial})^{-1}$. Values with no parentheses include pumping losses, $(\tau_{ic})^{-1} = (\tau_{ic}^{axial})^{-1} + (\tau_{ic}^{radial})^{-1} + (\tau_{ic}^{pumping})^{-1}$.

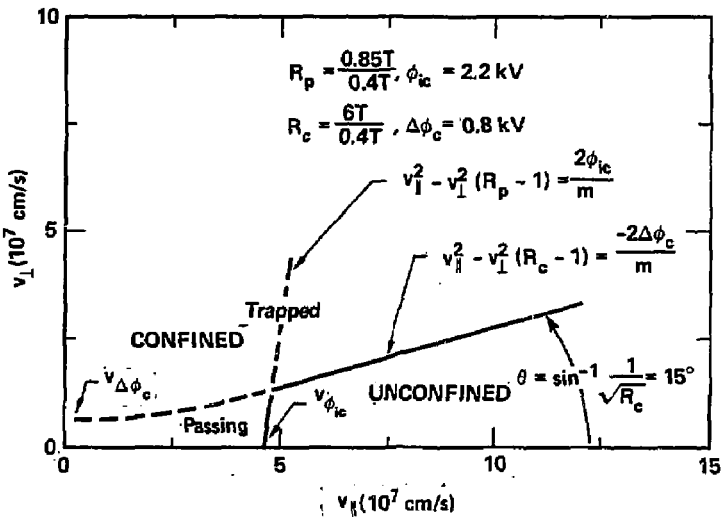

Fig. 2.2 -1 Central-cell phase space for the throttle geometry.

The parameters for Cases C and D are a self-consistent set in that they satisfy all the physics constraints discussed in Section 3.

In the remainder of this section, we give a step by step discussion of the parameters within Table 2.2-1. Appendix A supports these values by the use of analytical equations to model the particle and power balance.

Central-Cell Ion Fokker-Planck Results

In Table 2.2-1 we summarize the Fokker-Planck studies and associated analytical calculations used to compare the standard and throttle-coil-geometry operation of TMX-U. The power- and particle-balance equations for the central-cell ions (see Appendix A) were solved initially without the additional constraints set by the theoretical limits of Section 3. At a midplane magnetic-field value, B_c = 0.3 T, the available neutral-beam power was large enough and the ion confinement long enough so that the calculated parameters from the Fokker-Planck code could surpass the the theoretical central cell beta limits. In the reference case, the operating parameters for B_c = 0.4 T satisfy the constraints from Table 1-1.

The Kelley-TDF mode of the throttle coil geometry utilizes the same end-cell parameters and the same central-cell neutral beams as the standard geometry for TMX-U.[2.2-1] Using the same standard-geometry value for the ion-confining potential, ϕ_{ic} = 2.2 kV, and the values of 170 atom amps (Case C) and 70 atom amps (Case D) for the incident neutral-beam current with $V_{extraction}$ = 15 kV, the central-cell ion distribution is calculated using the Fokker-Planck computer code.[2.2-2] The central-cell electron temperature, T_{ec}, is an input parameter to the code. The T_{ec} input value of 0.6 keV is justified in Appendix A, which gives a detailed description of the electron power and particle balance for the central cell.

The velocity-space loss boundary at the central-cell midplane is shown schematically on Fig. 2.2-1. The two mirror ratios are the central-cell mirror ratio, $R_c = B_{Th}/B_c = \frac{6\ T}{0.4\ T} = 15$, and the mirror ratio associated with the potential peak ϕ_p within the anchor, $R_p = B_p/B_c = \frac{0.85\ T}{0.4\ T} = 2.1$. A potential drop $\Delta\phi_c$ from the central-cell midplane to the throttle coil exists because of the drop in density from the midplane, $n_{ic}^{trapped} + n_{ic}^{passing}$, to the throttle coil, $n_{ic}^{passing}$ at $B = B_{Th}$. Only recently could the potential peak and magnetic field peak be modeled in the code to occur at different axial (z) locations.[2.2-3]

When comparing the Fokker-Planck results between the standard and throttle coil geometry, the parameters associated with the Fokker-Planck analysis of the standard geometry (Case B) will be used instead of Case A, which summarizes the original TMX-U proposal numbers.[2.2-1] Beginning with the input parameters in Table 2.2-1, the incident beam and gas sources for Case B are the same as the TMX-U proposal. A derivation of the source terms associated with the neutral-beam and gas injection is given in Appendix A. Charge-exchange effects from the beam and gas sources were included along with the ionization sources. The ratio of charge-exchange to ionization events were 2 to 1 for the beam source and 3 to 1 for the gas-feed source. The equivalent current in amps for each source can be evaluated by using $I = n_c \nu e \frac{1}{3} \pi r_c^2 L_c$, where n_c is the central-cell density, ν is source strength (s^{-1}), for example, $\nu_{beam}^{ioniz} = n_{beam} \langle \sigma v \rangle^{ioniz}$, $\frac{1}{3}$ is from geometry averaging, assuming parabolic profiles in radius, r_c is the plasma radius, and $L_c = B_c \int dl / B_c$ is the flux equivalent length (510 cm for the standard geometry and 260 cm for the throttle coil geometry).

The value of r_c for Case A was arrived at by flux conservation between the end-cell anchor and central cell (B_A = 0.5 T, B_c = 0.3 T), r_A = 20 cm being the TMX-U proposal estimate. More recent estimates of r_A with thermal-barrier operation are closer to 15 instead of 20cm, with a halo plasma extending to 25 cm. Flux mapping 25 cm to the central cell midplane gives r_c^{halo} = 33 cm. The throttle coil at B_{Th} = 6 T will allow, if necessary, a plasma extending to 49 cm in radius to map from the central-cell midplane through the coil. On the other hand, recent TMX-U data (nonthermal-barrier operation) gives r_c = 22 cm for a parabolic fit and 18 cm for a Gaussian fit to the beam-attenuation line-density measurements.[2.2-4] Case B used r_c = 22. Rather than reduce the Case B value for r_c by the change in B_c from 0.3 T to 0.4 T for Cases C and D, the ECRH horn aiming at 15 cm in the end-cell anchor was mapped back to the central cell to give r_c = 17 cm. Similar mapping of the anchor halo radius (25 cm) gives r_c^{halo} for Case C equal to 28 cm. At B_c = 0.4 T, the throttle coil can be operated at or as low a value as 2.6 T and still allow a 28 cm radius plasma to map through. At B_c = 0.3 T, B_{Th} = 2 T still clears r_c = 28 cm.

The incident beam current, I_{beam}^{incid}, can be derived using

$$n_{ic} v_{beam}^{ioniz} e \frac{1}{3} \pi r_c^2 L_c \frac{\langle\sigma v\rangle^{total}}{\langle\sigma v\rangle^{ioniz}} = I_{beam}^{incid} \left[1 - \exp - \left(\frac{\langle\sigma v\rangle^{total} \int n dl}{v_{beam}} \right) \right] k_{geom} , \quad (2.2.1)$$

where $\langle\sigma v\rangle^{total} = \langle\sigma v\rangle^{ioniz} + \langle\sigma v\rangle^{c\text{-}x}$, and $k_{geom} \leq 1$ takes into account that beam trapping occurs in the core and halo plasma and that the beam footprint is not necessarily small compared to the core plasma diameter. The incident gas current is the sum of the ionized and charge-exchange gas currents.

The only major discrepancy between the standard-geometry Fokker-Planck run (Case B) and the analytically derived parameters (Case A) is in the ion energy and temperature. Case A assumed that the ion density had two energy components: a "bulk" isotropic component with an ion temperture T_{ic}^{warm} of 0.9 keV and n_{ic}^{warm} of 1.7 X 10^{12} cm^{-3}. The remaining density, 0.6 X 10^{13} cm^{-3} = n_{ic}^{hot}, is described by a tail distribution made up of the slowing down, neutral-beam trapped particles with a mean energy of 4.7 keV. The Fokker-Planck output (Case B) gives an anisotropic Maxwellian distribution with a perpendicular temperature $T_{ic}^{\perp}$ of 1.5 and a parallel value $T_{ic}^{\parallel}$ of 1.0 keV. Similar to the TMX-U proposal, the central-cell beta for Case A is the total beta (bulk ion, beam ion, and electron pressure).

Case C describes the throttle coil geometry of TMX-U. The central-cell volume, $V_c = \pi r_c^2 L_c$, is 240 rather than 780 liters for Case B because of the reduction in r_c and L_c. The central-cell mirror ratio R_c reflects the throttle coil field value of 6 T compared to the inner end-cell mirror field value of 2 T. Case C assumes the same ion confining potential, ϕ_{ic} = 2.2 keV, used for Case B, which was derived from the end-cell parameters given in the TMX-U proposal.[2.2-1] The electron temperature of 0.6 keV was also kept the same as in Case B. The electron power balance for Case C (discussed in Appendix A) shows more than enough ion-electron-drag power in the central cell to justify T_{ec} = 0.6 keV. From earlier studies of the throttle coil geometry, it was apparent that a smaller gas feed would be required and that a potential drop from the central-cell midplane to the throttle coil would develop because of the large number of mirror-confined

ions. The anisoptropic temperature, already present in Case B, will cause in Case C (with R_c = 15) the total density at B_{Th} to be less than at B_c because of the mirror effect. The value chosen for $\Delta\phi_c$ in the ion loss boundary in Fig. 2.2-1 was 0.8 keV. In Case C the final equilibrium value for $\Delta\phi_c$ turned out to be

$$\Delta\phi_c = T_{ec} \ln \frac{n_{ic}}{n_{ic}(B=B_{Tn})} = 0.85 \text{ keV} \quad . \tag{2.2.2}$$

This small discrepancy will not affect any other parameters.

The solid curve in Fig. 2.2-1 is the loss boundary for axial losses. Both the magnetically trapped and electrostatically stoppered (passing) populations are lost because of collisions that transport particles from the confined region to the unconfined region. An analytical fit to the axial losses that is within ±10% to the Fokker-Planck result for $R_c > 10$, $R_p > 2$, and ϕ_{ic}/T_{ic} of order one, is

$$(n\tau)_{ic}^{axial} = 3 \times 10^{10} \cdot T_{ic}^{3/2} \left[4 \log R_c + G(R_p) \frac{\phi_{ic}}{T_{ic}} \exp \frac{\phi_{ic}}{T_{ic}} \right] \quad , \tag{2.2.3}$$

where $T_{ic} = \frac{2}{3} E_{ic}$ and $G(R) = \frac{R+1}{R} \ln (2R + 2)$. The first term of Eq. (2.2.3) is similar in value to the axial confinement of a simple mirror, $k \times 10^{10} (E_{beam}^{inj})^{3/2} \log R$. The second term is similar to the $\frac{\phi}{T} >> 1$ limit of the Pastukhov confinement,

$$\frac{m^2 v^3}{4\pi e^4 \ln\Lambda} \frac{\sqrt{\pi}}{2} G(R) \frac{\phi}{T} \exp \frac{\phi}{T} \quad ,$$

which for $\ln \Lambda = 20$ and $v = (2T/m)^{1/2}$ becomes $2.4 \times 10^{10} T^{3/2} G(R) \frac{\phi}{T} \exp \frac{\phi}{T}$. The simple mirror term is evaluated with $R = R_c = B_{Th}/B_c$, the full central-cell mirror ratio, and the Pastukhov term with $R = R_p = B_p/B_c$, the mirror ratio to the potential peak within the end cell ($\log 6/0.4 = 1.2$ and $G(\frac{0.85}{0.4}) = 2.7$). For injection angles θ_{inj} other than 90°, one should use the effective mirror ratio, $R_{eff} = R\sin^2\theta_{inj}$. For ϕ_{ic}/T_{ic} of order one, the Pastukhov term is only 50% larger than the simple mirror term.

The dashed curve in Fig. 2.2-1 separates the confined region in phase space into the trapped and passing particle subregions. The passing-particle subregion has an additional loss rate, $\nu_{passing}$, because of radial transport associated with the nonsymmetric magnetic fields beyond the throttle coil ($\nu_{passing}^{radial}$) and because of pumping losses from the neutral beams used to charge-exchange pump the trapped populations within the transition and end cell ($\nu_{passing}^{pumping}$). The pumping loss rate also includes the particle losses associated with the collisional trapping of the passing population within the end cell and the transition cell. Whatever loss processes (radial or pumping) are experienced by the passing particles, they are reduced for the total central-cell population according to

$$\tau_{ic}^{passing} = \nu_{passing}^{-1} \frac{n_{ic}}{n_{ic}^{passing}} , \qquad (2.2.4)$$

or equivalently,

$$\tau_{ic}^{passing} = \nu_{passing}^{-1} \left(\frac{n_{ic}}{n_{ic}^{mirror}}\right)\left(\frac{B_c^{mirror}}{B_c}\right) , \qquad (2.2.5)$$

where $n_{ic}^{mirror} = n_{Th}$ and $B_c^{mirror} = B_{Th}$. From Fig. 3.5.3, $\tau_{ic}^{radial} \geq 0.5$ s for radial electric fields less than 100 V/cm. Equations 3.6.3 through 3.6.7 give $\tau_{ic}^{pumping} \simeq 0.13\ s^{-1}$. For $R_{Th} = B_{Th}/B_c = 15$ and $n_{ic}/n_{ic}^{mirror} \simeq 3$, then $\nu_{passing} = \nu_{passing}^{radial} + \nu_{passing}^{pumping} = 90 + 360 = 450\ s^{-1}$, giving $\tau_{passing} = 2.2$ ms.

Figure 2.2 -2 compares the perpendicular ion-distribution function, $f_{ic}(v_\perp)$, for Case C with a gas feed giving 2 gas atom amps ionized to that of a similar Fokker-Planck run (Case C') at half the gas feed. The fact that $f_{ic}(v_\perp)$ for Case C' is not monotonic, as it is for Case C, represents a destabilizing drive for instabilities within the central cell, such as the drift-cyclotron loss cone (DCLC) mode (see Section 3.4). At n_{ic} of $4 \times 10^{13}\ cm^{-3}$, ν_{gas}^{ioniz} of $4\ s^{-1}$ generates two ionized atom amps and also a monotonic $f_{ic}(v_\perp)$.

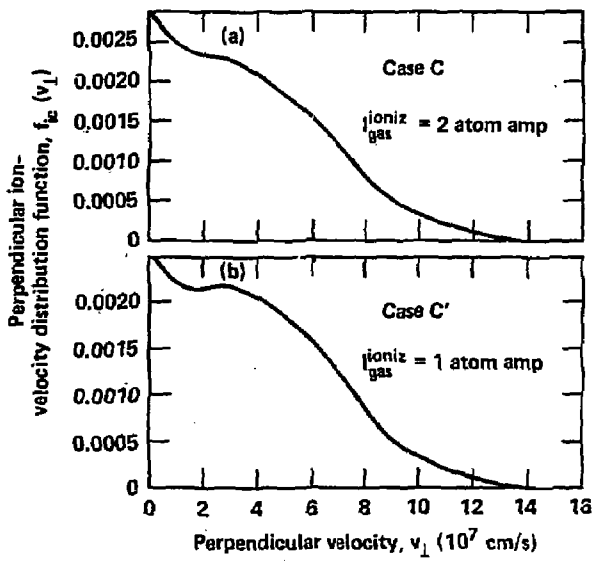

Fig. 2.2 -2 Central-cell velocity distribution for ions, $f_{ic}(v_\perp)$. A minimum amount of ionized gas current (approximately 2 atom amp.) is required to generate a monotonically decreasing $f_{ic}(v_\perp)$.

To estimate what neutral beam source term, ν_{beam}^{ioniz}, will generate a required incident neutral beam current near the 180 atom amps available, Eq. (2.2.1) is used. Particle balance demands,

$$\frac{n_{ic}^2}{(n\tau)_{ic}} = n_{ic}\left(\nu_{gas}^{ioniz} + \nu_{beam}^{ioniz}\right) . \qquad (2.2.6)$$

Eqs. (2.2.3) and (2.2.5) predict $(n\tau)_{ic} = \{[(n\tau)_{ic}^{axial}]^{-1} + [(n\tau)_{ic}^{passing}]^{-1}\}^{-1} \approx 10^{12}$ cm^{-3}· s. The solution to Eq. (2.2.1) for $\nu_{gas}^{ioniz} << \nu_{beam}^{ioniz}$ and, therefore, from Eq. 2.2.6 $n_{ic} = \nu_{beam}^{ioniz}\, 10^{12}$ is that $\nu_{beam}^{ioniz} \approx 40$ s^{-1} for $I_{beam}^{incid} \approx 180$ atom amps.
Equation (2.2.6) would predict n_{ic} approximately equal to 4×10^{13} cm^{-3}.
The following plasma-parameter values were used to solve Eq. (2.2.1):

$\pi r_c^2 L_c = 2.4 \times 10^5$ cm^3,

$\langle\sigma v\rangle^{ioniz} = 3.6 \times 10^{-8}$ cm^3·s^{-1},

$\langle\sigma v\rangle^{total}/\langle\sigma v\rangle^{ioniz} = 3$,

$v_{beam} = 10^8$ cm/s, $k_{geom} = 0.45$,

$\int n dl = \frac{4}{3} n_{ic} r_c^{halo} \sin\theta_{inj}^{-1}$,

$\theta_{inj} = 65^0$, and $r_c^{halo} = 28$ cm.

Once the particle source term is picked and the particle loss rates defined, the Fokker-Planck equation is iterated by the code until a velocity distribution is generated that satisfies both ion particle and power balance. The velocity distribution for case C is shown in Fig. 2.2-3. The distribution is anisoptropic with $T_{ic}^{\perp} > T_{ic}^{\parallel}$ and fills the entire confined region of velocity space. Moments of f(v) give $n_{ic} = 4.0 \times 10^{13}$ cm^{-3}, $E_{ic} = 5.5$ keV, $T_{ic}^{\perp} = 4.3$ keV, and $T_{ic}^{\parallel} = 2.4$ keV. The central-cell confinement parameter, $(n\tau)_{ic}^{total} = n_{ic}/\nu_{beam}^{ioniz} = 8.6 \times 10^{11}$ cm^{-3}·s, is the reciprocal of the

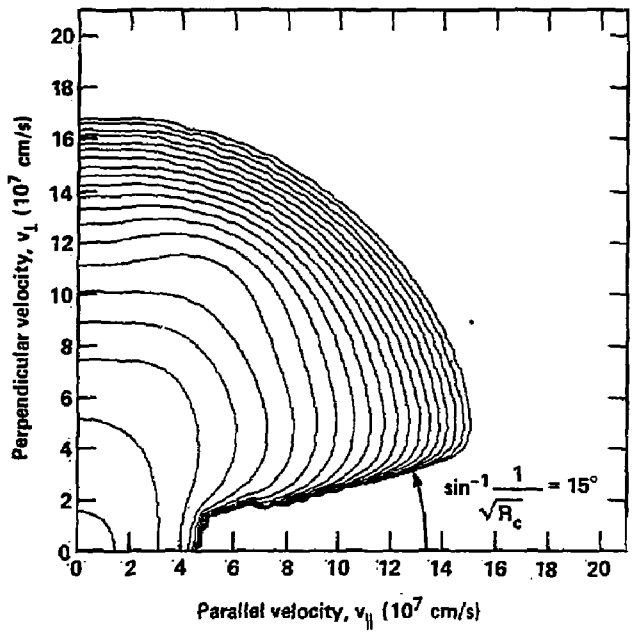

Fig. 2.2 -3 Central cell ion velocity distribution for Case C, R_c = 6 T/0.4 T = 15.

inverse sum of the axial, radial, and pumping confinement parameters: 11 X 10^{11}, 200 X 10^{11}, and 50 X 10^{11} cm^{-3}•s, respectively. The density and pressure versus B profiles imply that $n_{passing}^{Throttle}$ = 1.2 X 10^{13} cm^{-3} and $T_{passing}^{Throttle}$ = 1.3 keV.

The MHD stability of Case C requires maximum available end-cell beta, and, therefore, optimum performance of the ECRH hardware. Case D of the throttle coil geometry describes an operating point with reduced demands on the end-cell beta and hence ECRH power. To reduce the central-cell beta but still keep the density near that of Case B, we reduce the incident neutral-beam current from 170 to 90 atom amps, and a total of 39 atom amps of incident gas fueling is included to lower the ion temperature.

When gas fueling is used to augment the neutral beam fueling, a larger fraction of the midplane density will appear at the central-cell mirror, i.e, the passing population will increase. This can be seen by comparing the ratio of $n_{passing}^{mirror}$ to n_{ic} in Cases B and C, taking into account that B_c^{mirror} = 2 T for Case B and 6 T for Case C. The values for $(n\tau)_{ic}^{radial}$ and $(n\tau)_{ic}^{pumping}$ will be decreased by the increase in n_{ic}^{mirror} according to Eq (2.2.5). The pumping-confinement parameter will be lowered also because of the increase in $n_{passing}$ and the reduction in $T_{passing}^{mirror}$, both of which lead to higher ion-scattering rates and, therefore, to larger trapping and pumping losses (see Eqs. 3.6.3 thru 3.6.7). The axial-confinement parameter, $(n\tau)_{ic}^{axial}$, remains nearly the same because the decrease in the ion-scattering lifetime (proportional to $T_{ic}^{3/2}$) is offset by the larger potential confinement (proportional to ϕ_{ic}/T_{ic}) for ϕ_{ic} being fixed at 2.2 kV (see Eq. 2.2.3).

Using the particle inputs, power inputs, and confinement times associated with Case D results in an operating point with the same central-cell beta, but higher confinement time, as Case B, but with lower demands on the central-cell beam current and end-cell ECRH power in Case C.

Case C is still of interest because it has two and one-half times more plasma pressure than Case D which allows regimes of MHD stability nearer those of MFTF-B and reactor designs yet to be investigated.

REFERENCES

2.2.-1. F. H. Coensgen, T. C. Simonen, A. K. Chargin, and B. G. Logan, TMX-U Major Project Proposal, LLNL Report, LLL-Prop-172, (April 1980).

2.2.-2. T. A. Cutler, L. D. Pearlstein, and M. E. Rensink, Computation of the Bounce-Average Code, LLNL Report, UCRL-52233 (1977).

2.2.-3. M. E. Rensink, Appendix E, in LLNL Report, UCID-19359 (1982). Physics Basis for an Axicell Design for the End Plugs of MFTF-B D. E. Baldwin and B. G. Logan, Eds.

2.2.-4. J. H. Foote, R. S. Hornady, and F. E. Coffield, "Plasma-Density Measurements in TMX Upgrade," Bull. Am. Phys. Soc., 27 (8), 999 (October 1982).

2.3. END-CELL REQUIREMENTS

D. P. Grubb, T. D. Rognlien, and E. B. Hooper, Jr.

2.3.1. Introduction

In this section we compare the ECRH and neutral-beam power requirements of the plugs in the TMX-U standard geometry device with those in TMX-U with an added throttle coil. We find the throttle coil (Case C) needs less neutral beam current than the present TMX but requires more ECRH power to anchor the desired high central-cell betas. The reduced plug neutral beam requirements with the throttle coil reflect the reduction of the required pumping rate in the plugs (Sec. 3.6). The additional ECRH power is necessary to heat the plug electrons to an average perpendicular energy greater than 70 keV so they can effectively anchor the system against finite-β ballooning modes at the highest achievable central-cell beta-Case C (Sec. 3.1). The specific causes of the changes in the plug requirements are summarized in Table 2.3.1 along with a qualitative assessment of the resulting impact on the neutral-beam and ECRH power systems.

Quantitatively, our analysis indicates that with the throttle coil in place the plugs for Case C will require between 50 and 105 A of sloshing-beam current and between 30 and 40 A of pump beam current per plug. These values are presently obtainable on TMX.

In terms of the ECRH power requirements, the available 200 kW per plug is sufficient to heat the electrons to an average total energy of 35 keV at a density of roughly 4×10^{12} cm^{-2}. This provides a peak plug $\hat{\beta}_A$ of 0.20, which is sufficient to anchor a peak central-cell of $\hat{\beta}_c$ of 0.26. This is less than the desired $\hat{\beta}_c$ of 0.50 for Case C. However, the modeling to date of the hot-electron power requirements has not included finite $k_{\parallel}$ effects and optimized microwave beam patterns, which could raise the maximum hot-electron energy. We also note, though, that our models do not include the absorption of ECRH power in the halo which surrounds the plug plasma or any source of cold electrons in the potential peak. These effects reduce the amount of ECRH available to heat the hot electrons in the plasma core and, therefore, tend to reduce the maximum achievable hot-electron energy. When all of these effects are included in our codes, we will be

Table 2.3-1. Effect of throttle coil on plug-power requirements.

With Throttle Coil	Primary Result	Secondary Result
(1) Thermal barrier filling rate reduced	Less pumping current required	Less sloshing-ion current required
(2) Some pumping is done in the transition where there are no sloshing ions	Less sloshing-ion current required	
(3) Because of (1) and (2) the throttle coil requires less beam current	Less gas introduced into plugs by neutral beams	Plugs require less halo plasma
(4) Passing-ion density in the barrier is lower	For g(b) ~ 2 the plug with a throttle coil allows more sloshing ions at the barrier[a] and, therefore, a higher density at the potential peak	Less ECRH power required to produce ϕ_{ic}
(5) Density of cold electrons "leaning in" on the hot-plug electrons is lower	Less ECRH power required	
(6) The ratio β_p/β_c required for MHD stability is higher	More ECRH power required to anchor the throttle-coil tandem	
(7) Higher electron energy required by (6) necessitates a larger fraction of cold electrons in the barrier to avoid ion-ion two-stream instability	More ECRH power required	

[a]This benefit can be realized if a 0.25 density ratio of warm-ion to sloshing-ion in the barrier is stable to loss-cone modes.

better able to predict the maximum plug betas achievable in TMX-U. At this time we feel that we will be able to heat the plug electrons to $E_{eH}^{\perp} > 70$ keV as required for MHD stability of throttle coil Case C (Table 2.3-1.)

In our analysis of the plug requirements for TMX-U with a throttle coil we have also examined the ECRH and beam requirements for Case D. Case D uses less central-cell beam heating than Case C so that the central-cell beta is reduced to 0.27. Based upon Fokker-Planck and Monte-Carlo code analysis of the ECRH power requirements for Case D, we conclude that the available 200 kW per plug of ECRH power is sufficient to heat the plugs to a beta of 0.20 which provides an adequate MHD anchor for the central-cell.

In terms of the plug beam requirements, we found that Case D requires two more pumping beams per plug than Case C because the passing ion density is higher and the passing ion temperature is lower in Case D than in Case C. TMX has a sufficient number of neutral beams to provide the two extra beams per plug. It is important, however, that we have a good vacuum for this case because our present estimates of the pumping requirements do not include charge exchange on background gas. This possible source of cold ions must, therefore, be small compared to pitch-angle scattering and energy diffusion which are included in our models.

We now proceed in Sec. 2.3.2 and 2.3.3 to describe the analysis for Case C which led to our conclusions about the plug requirements. In Sec. 2.3.4 we examine the question of ion microstability in the plugs.

2.3.2. Plug Neutral-Beam Requirements

In this section, we describe the analysis that led to the plug beam requirements. As indicated in Table 2.3-1, the throttle coil geometry requires less sloshing-beam current than does the standard TMX-U geometry, primarily because the throttle coil reduces the density of passing ions in the plugs which can fill in the barrier. This reduces the barrier filling rate and, therefore, reduces the required pumping-beam current. In addition, with the throttle coil, some of the pumping is done in the transition region away from the plugs and the sloshing ions. (These phenomena are described in Sec. 3.6.) Because the sloshing ions are lost predominantly by charge-exchange with the pump beams, reducing the pump-beam current in the plug also reduces the required sloshing-beam current.

We modeled the pumping in the plug region by using a multiregion Fokker-Planck code developed by Matsuda.[2.3-1] We found a sloshing-beam current of 90 A with a pump-beam current of 40 A was sufficient to pump the warm-ion density in the barrier down to $n_{iw}(b) = 8 \times 10^{11}$ cm^{-3}, for a passing ion density $n_{passing}^{mirror} \approx 1.3 \times 10^{13}$ cm^{-3} with $T_{passing}^{mirror} = 1$ keV. This corresponds roughly to $g(b) = 2$, where $g(b) = [(n_{pass} + n_{trap})/n_{pass}]$ evaluated at the midplane of the barrier (point b).

At this time the code does not calculate the trapping of the sloshing ions and, therefore, does not self-consistently calculate the sloshing ion density. We can estimate sloshing-ion density by assuming the sloshing-ion lifetime is determined entirely by charge-exchange with the pump beams. In this limit, we solve for the sloshing-ion density according to

$$I_b^s (\sin 47^o)^{-1} [1 + (\langle\sigma_{cx}\rangle/\langle\sigma_i\rangle)(n_{iw}(b)/n_b)] \approx$$

$$I_b^p (\sin 18^o)^{-1} (\langle\sigma_{cx}\rangle/\langle\sigma_i\rangle)(n_{ih}(b)/n_b) \quad ,$$

where we have set the input current that is due to ionization of the sloshing beams and sloshing beam charge exchange of warm ions equal to the loss current that is due to pumping. For a sloshing-beam current of $I_b^s = 90$ A, a pumping beam current of $I_b^p = 40$ A, the ratio of charge-exchange cross sections to ionization cross section $\langle\sigma_{cx}\rangle/\langle\sigma_i\rangle = 2.5$, and a ratio of warm ions to total ion density* at b equal to $n_{iw}(b)/n_b = 8 \times 10^{11}/4 \times 10^{12}$, we find a sloshing-ion density $n_{ih}(b) = 2.3 \times 10^{12}$ cm^{-3} which is close to the desired value of 3.2×10^{12}. To obtain $n_{ih}(b) = 3.2 \times 10^{12}$ while maintaining the desired pumping requires us to adjust the currents slightly to $I_b^s = 105$ A with $I_b^p = 33$ A.

It is possible that this case with $n_{iw}(b)/n_b = 0.2$ is not stable to loss-cone modes because of the low value of $n_{iw}(b)/n_{ih}$. We are presently analyzing the stability of this case using Pearlstein's marginal stability code.[2.3.2] Previous stability analysis for TMX-U indicated that a value of

*The total ion density at b is limited to 4×10^{12} cm^{-3} so that ECRH of $2\,\omega_{ce}$ can be used.

$n_{iw}(b)/n_b \approx 0.5$ was required for loss-cone stability.[2.3-3] We can raise the value of $n_{iw}(b)/n_b$ for the throttle coil case by reducing the beam currents to reduce the pumping rate so that g(b) rises from the g(b) = 2, in the case we just analyzed, to g(b) = 5.*

As shown in Fig. 2.3-1, the value of g changes rapidly as a function of the pumping rate when g is in the range of 2 to 6.[2.3-4] A reduction in the beam current of order 25% will allow us to go from g(b) = 2, which may be loss-cone unstable, to g(b) = 5, which corresponds to $n_{iw}(b)/n_b = 0.5$ and should be stable.

For $n_{iw}(b)/n_b \approx 0.5$, the required beam currents are $I_b^s = 49$ A and $I_b^p = 38$ A. These values as well as those calculated in the previous case are well within our present capabilities.

At this point we note that our initial assumption that the sloshing ion losses are dominated by charge exchange with the pump beams is valid. When we compare the pumping time,** $\tau_{pump} = 10$ ms, to either the scattering time, $\tau_{ii} \approx 160$ ms, or to an electron-drag time, $\tau_{drag} \approx 160$ ms, where $\tau_{ii} = 2.5 \times 10^{11} E_i^{3/2}(\text{keV})\, A_i^{1/2}(\text{amu})/(Z^4\, n \ln\Lambda_{ii})$ and $\tau_{drag} = 10^{13}\, A_i(\text{amu})\, T_e^{3/2}(\text{keV})/Z^2\, n \ln\Lambda_{ei}$ we find that the pumping time is fast compared to either scattering or drag.

In our analysis we have assumed a perfect vacuum so that there is no charge exchange on background gas. It is difficult to include charge exchange on background gas analytically in the sloshing-ion particle balance, because the rate at which the resultant cold ions are lost is a function of position on the axial potential profile where the charge exchange event took place, on the pumping rate, and on the heating rate of the cold ions by the electrons and sloshing ions. Qualitatively, we know that charge exchange on gas will require us to raise both the pumping and sloshing beam currents. We plan to use the Fokker-Planck code to determine the magnitude of the increase as a function of the background gas pressure.

---

*$n_{iw}(b) = g(b)\, n_{pass}(b)$.

**$\tau_{pump} = n_{ih}(b) V_p/(I_b^p\, f_{cx}^p\, n_{ih}(b)/n_b)$ where V_p is the volume of the sloshing ions and f_{cx}^p is the fraction of the pump beam which is stopped by charge exchange.

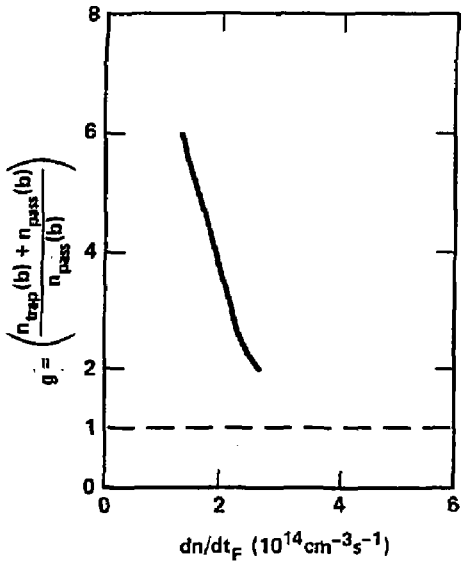

Fig. 2.3 -1. Change in value of g as a function of pumping rate for throttle coil with n_{pass}^{mirror} = 1.4 x 10^{13} cm^{-3}, T_{pass}^{mirror} = 1 keV, and ϕ_b = 2.2 kV.

2.3.3. ECRH Power Requirements

As shown in Table 2.3-1 several differences between TMX-U with and TMX-U without the throttle coil affect the ECRH-power requirements. Our analysis indicates that the two most important changes are, first the reduced cold-electron density "leaning in" on the hot electrons and second, the need for higher energy hot-electrons to provide an MHD anchor for the central cell.

The density of cold electrons leaning in on the hot electrons is less with the throttle coil, because pumping in the transition region reduces the density at the plug inner mirror to less than the central-cell density (Fig. 2.3-2). Because these cold electrons drag as well as scatter the hot electrons, reducing the cold-electron density reduces ECRH power requirements.

To determine the magnitude of this effect, we used Rognlien's Monte Carlo code to calculate the hot-electron energy and density that we can achieve with the available ECRH power (200 kW per plug, 100 kW of fundamental ECRH power, and 100 kW of second harmonic ECRH power). We found that the reduced cold-electron density allows us to obtain E_{eH} = 35 keV with the throttle coil as opposed to E_{eH} = 25 to 30 keV with the present TMX-U geometry.

The increased hot-electron energy is required if the plugs are to anchor a maximum central-cell beta. The increased confinement time of the central-cell ions and the reduced volume of the central-cell plasma allows the available central-cell beam current of 180 A to heat the central-cell to a higher beta than can be achieved in the present TMX-U geometry. With the throttle coil in place, we have sufficient neutral-beam power to raise the average central-cell beta to 33% for the B_c = 3 kG or 25% for B_c = 4 kG (see Table 2.2-1) as opposed to $\langle\beta_c\rangle$ = 13% for the present geometry.

The higher value of β_c and the fact that the throttle coil for a given central-cell beta requires a higher plug beta in order to maintain MHD stability (see Sec. 3.1), dictates that the average hot-electron energy must be significantly higher with the throttle coil.

For the throttle-coil base case in Table 2.2-1 Case C, we can calculate the hot-electron energy required for MHD stability (see Fig. 3.1-5,)

$$\beta_c/\beta_p = 0.50/0.40 = 0.50/\left\{\left[n_{eH}(b)\, E_{eH}^{\perp}(b) + n_{iH}^{\perp}(b)\, E_{iH}(b)\right] \Big/ \left(\frac{B^2(b)}{8\pi}\right)\right\} .$$

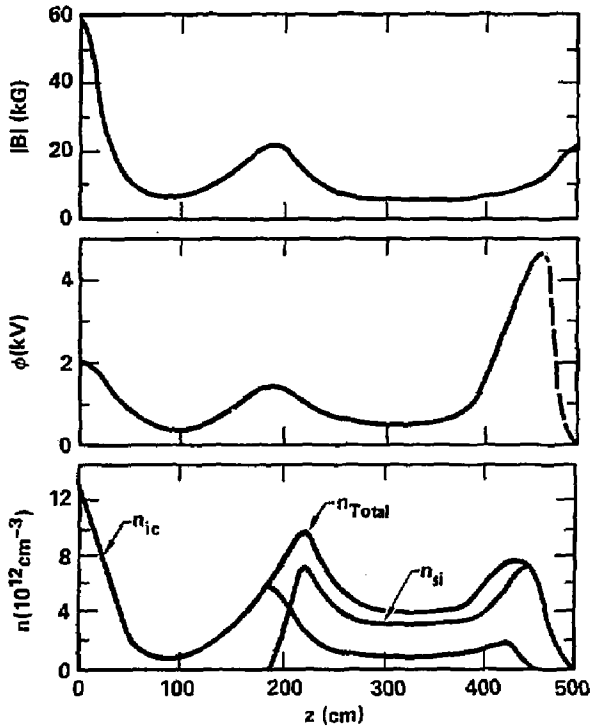

Fig. 2.3.-2. Axial profiles of $|B|$, ϕ, and n in the transition and end cell (Case C).

For $n_{iH}(b) = 3.2 \times 10^{12}$ cm^{-3}, $E_{iH}^{\perp}(b) = 4$ keV, $n_{eH}(b) = (0.86)\ (4 \times 10^{12})^{*}$ cm^{-3}, and B(b) = 0.5T, we find that $E_{eH}^{\perp}(b) = 74$ keV is necessary to obtain marginal stability to m = 1 finite-beta ballooning modes.

A similar calculation for the present TMX-U geometry (Case B in Table 2.2-1) shows that TMX-U in its present mode of operation requires an average hot-electron energy of 20 keV to anchor the system. Primarily this is due to the reduced value of central-cell beta ($\hat{\beta}_c = 0.26$) and a more favorable ratio of β_c/β_p allowed by MHD stability. The value of 20 keV at $n_{eH}(b) = 3.6 \times 10^{12}$ appears to be achievable with the available ECRH power.**

2.3.4. Microstability

The plasmas that can be obtained in the plugs are limited by power and particle balance and constrained by ion and electron microstability. The introduction of the throttle coil causes two changes that affect the ion microstability: the passing ion density at the plug midplane is reduced, and we increase the average hot-electron energy to maintain MHD stability at the highest achievable central-cell betas.

As described earlier in Sec. 2.3.2, the warm-ion density at the plug midplane is approximately 8×10^{11} cm^{-3} for the Case C parameters. The corresponding sloshing-ion density is 3.2×10^{12} cm^{-3} for a ratio of warm to hot ions at b of 0.25. Such a small value of $n_{iw}(b)/n_b$ is desirable to minimize the ECRH power requirements. The Monte Carlo code modeling of the ECRH heating shows that we require less fundamental ECRH-heating power to achieve the desired ion confining-potential (2.2 kV) as the density ratio at

*$n_{eh}(b) = 0.86\ n_b$ is necessary to satisfy ion-ion two-stream stability, which requires approximately 14% cold electrons at b.

**For the present TMX-U geometry, both the predicted hot-electron energy and that required for MHD stability are reported in this document to be less than specified in the TMX-U Major Project Proposal. The expected energy has been revised downwards from 50 keV to 25 to 30 keV based on Fokker-Planck and Monte-Carlo code modeling of the hot-electron power and particle balance.[2.3.-1,2.3.-5]

The required value of E_{eH} for MHD stability has been reduced from 50 keV to 20 keV on the basis of stability modeling using plasma pressure profiles derived from Fokker-Planck code calculations and experimental measurements.[2.3.-6] Previous stability calculations were based on an assumed isotropic-pressure profile that placed more pressure in the bad-curvature regions of the magnetic field than was experimentally measured.

the potential peak over that at the barrier midplane is increased. Since this density ratio is due primarily to the sloshing ions, it is desirable to maximize the $n_{iH}(b)/n_b$ ratio to minimize the ECRH-power requirements.

The minimum value of $n_{iw}(b)/n_b$, however, is constrained by loss-cone stability. If this ratio becomes too small, the plasma will be unstable. Case C with $n_{iw}(b)/n_b = 0.2$ may indeed be unstable. Analysis using Pearlstein's marginal stability code is presently under way. If the analysis indicates the plasma is unstable, we will change the ratio of pump to sloshing-beam current, as described in Sec. 2.3.2, thus increasing the $n_{iw}(b)/n_b$ ratio to obtain stability. This will decrease the total beam requirements but will raise the ECRH power requirements.

The second change in the ion microstability caused by the introduction of the throttle coil is an increased need for cold electrons at the barrier midplane. These electrons are needed to maintain stability against ion-ion two stream modes. As described in Ref. 2.3-7, the cold electrons Landau damp the waves to provide stability. The relative density of cold electrons that are necessary to obtain stability is given by

$$[(n_{ec}(b)/n_b)\ (T_{ic}/T_{ec}) + (n_{eH}(b)/n_b)\ (T_{ic}/T''_{eH})] = 0.27$$

where the value of 0.27 was taken from Ref. 2.3-7 (Fig. 2), which is reproduced here as Fig. 2.3-3. For $T_{ic} = 1$ keV, $T_{ec} = 0.6$ keV and $T''_{eH} = 20$ keV, we find $n_{ec}(b)/n_b = 0.14$. A similar calculation for the standard TMX-U geometry with a lower T''_{eH} value of 7 keV yields $n_{ec}(b)/n_b = 0.08$.

Since increasing the ratio $n_{ec}(b)/n_b$ decreases the thermal isolation between the central-cell and the plug electrons, the throttle coil requires somewhat more ECRH power than the present TMX-U geometry. We are presently modeling this effect with the Monte Carlo code but believe the increase in the required ECRH power will be small.

Finally, for the purpose of this report we have not reexamined the hot electron microstability. We assume that the plug plasma parameters are close enough to those in the original TMX-U proposal that the electron microstability is unchanged.

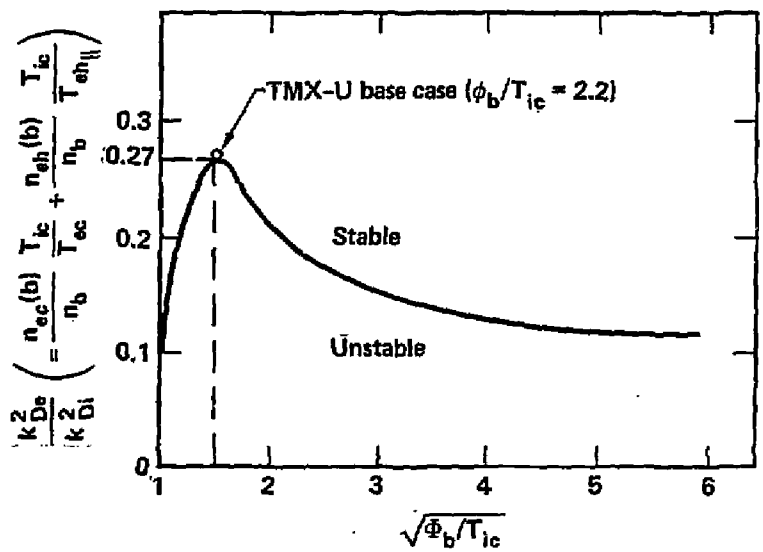

Fig. 2.3 -3. Stability boundary for ion two-stream mode.

REFERENCES

2.3.-1. Y. Matsuda and J. J. Stewart, "Fokker-Planck Calculations of Hot and Warm Electrons in a Tandem Mirror Plug," Bull. Am. Phys. Soc. 27, 1116 (1982).

2.3.-2. L. D. Pearstein, LLNL private communication.

2.3.-3. F. H. Coensgen, T. C. Simonen, A. K. Chargin, and B. G. Logan, TMX Upgrade Major Project Proposal, LLNL Report, LLL-Prop-172, (1980).

2.3.-4. A. H. Futch and L. L. LoDestro, Collisional Trapping Rates For Ions in a Magnetic and Potential Well, LLNL Report, UCRL-87249, (1982), submitted for publication; also A. H. Futch, "The Field Shape Factor for TMX-U," Internal Memorandum, LLNL (1982).

2.3.-5. T. D. Rognlien, "Tandem Mirror Thermal Barrier Formation with ECRH," Bull. Am. Phys. Soc. 27, 1116 (1982).

2.3.-6. W. E. Nexsen, "TMX-U Diamagnetic Measurements," Bull. Am. Phys. Soc. 27, 998 (1982).

2.3.-7. T. J. Orzechowski, "Cold Electrons in TMX-Upgrade Thermal Barrier," Internal Memorandum, LLNL (1980).

2.4. ION-CYCLOTRON RESONANT FREQUENCY (ICRF) HEATING OF THE CENTRAL CELL (MARS MODE)

A. Molvik

The addition of throttle coils to TMX-U necessitates a decrease in the ICRH power required for heating the central-cell ions. The power requirements are decreased by a factor of 5 during start-up before thermal barriers are formed. Power requirements are decreased by a factor of 2 at the new higher-design-level densities (Case C of Table 2.2-1) compared with densities observed without the throttle coil (Case A). Either directly or by equilibration with a energetic-ion tail, ICRH heats the bulk of the warm ions to maintain the central-cell temperature needed for MARS-mode operation. The transmitter power is about a factor-of-two higher than the absorbed power given in the figures.

We evaluate the power requirements for heating the TMX-U central cell equipped with throttle coils by following the treatment in Ref. 2.4.-1 (Appendices A and B). For start-up purposes, consider the power requirements before thermal-barrier formation (see Fig. 2.4-1). These can be compared with the power requirements in the absence of the throttle coil[2.4-1] (see Fig. 2.4-2). The power-balance model is summarized later.

Two aspects of the power requirements must be considered: first, the amount of power that must be absorbed to heat the ions and, second, the amount of power that can be absorbed. The first is displayed as the power in kilowatts. The second is shown by the ratio α, the power required in TMX-U to the measured power absorbed in Phaedrus[2.4.-1]. In Phaedrus, the power absorbed is approximately proportional to the plasma density and is expected to scale with the cross-sectional area of the plasma. One can then reasonably expect α as large as 4 to 10 in TMX-U[2.4.-1]. The power in kiloWatts indicates that the existing transmitter of 200 kW will sustain a plasma density exceeding 2×10^{12} cm^{-3} with the throttle coil compared to a density of about 1×10^{12}cm^{-3} without the throttle coil. This is compatible with $\alpha < 4$.

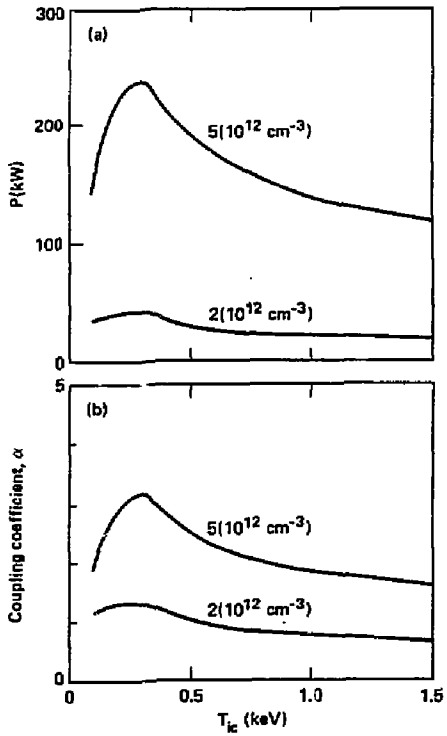

Fig. 2.4 -1. Power required to heat TMX-U (with throttle coil) during start-up. Central-cell ion temperature T_{ic} versus (a) power in kilowatts and (b) coupling coefficient α. Numerals on curves are for peak central-cell density n_c (powers calculated for a parabolic density profile).

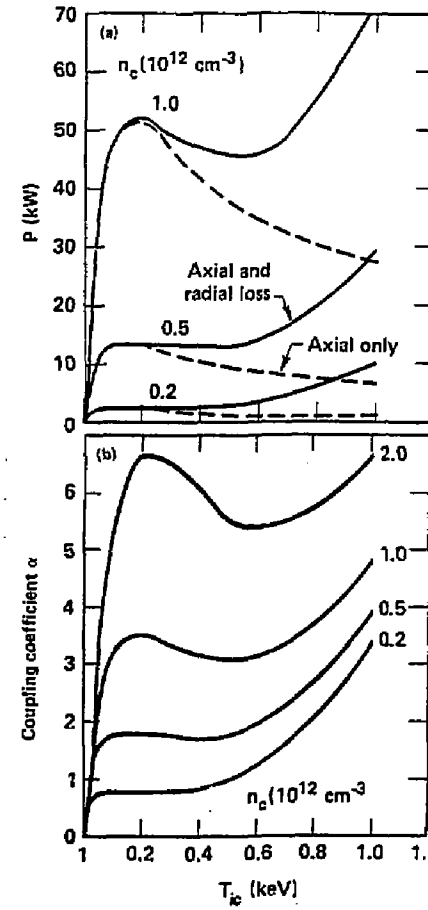

Fig. 2.4 -2. Critical ion-heating period before thermal-barrier formation (no throttle coil). Central-cell ion temperature T_{ic} versus (a) power in kilowatts and (b) coupling coefficient α.

The general power balance for ions is given approximately by

$$qk_2V\frac{dnE_{ic}}{dt} = 1.5 \times 10^{-8} n_c \alpha - \frac{qn_c^2\kappa_i V\, 1.5(T_{ic} - T_{ec})}{n\tau_{drag}}$$

$$- \frac{qn_c^2\kappa_2 V}{n\tau_{radial}} \left(1.5\, T_{ic} + \Gamma\frac{f_x}{f_1}\langle E_{cx}\rangle\right)$$

$$- \frac{qn_c^2\kappa_1 V}{n\tau_{axial}} \left\{\left[q\phi + T_{ic}\right] + \Gamma\frac{f_x}{f_1}\langle E_{cx}\rangle\right\} ,$$

where the coupling parameter α is defined as

$$\alpha \sim \left(\frac{r_c}{9\ cm}\right)^2 ,$$

to give the ICRH power (in watts) that we expect to couple into the central cell. The excess gas injected (over and above the end-loss current times the charge exchange to ionization ratio f_x/f_i) is given by Γ. The latter was taken to be two in these computations, which agrees well with gas-fueling efficiencies in TMX but needs to be reevaluated in the axisymmetric central-cell geometry of TMX-U. The volume is V. Axial losses dominate and are multiplied by charge exchange from gas fueling. At higher temperature, the axial confinement is given by

$$n\tau_1 = 5.47 \times 10^5 A^{0.5} (AMU)\, T_{ic}^{1.5}(eV) \frac{R_{eff} + 1}{R_{eff}} \ln(2R_{eff} + 2) \frac{1 + \frac{1}{4\chi^2}}{1 + \frac{1}{2\chi}} \chi \exp(\chi) ,$$

where $\chi = q\,\phi_c/T_{ic}$. The exact equations used are discussed in detail in Ref. 2.4.-1.

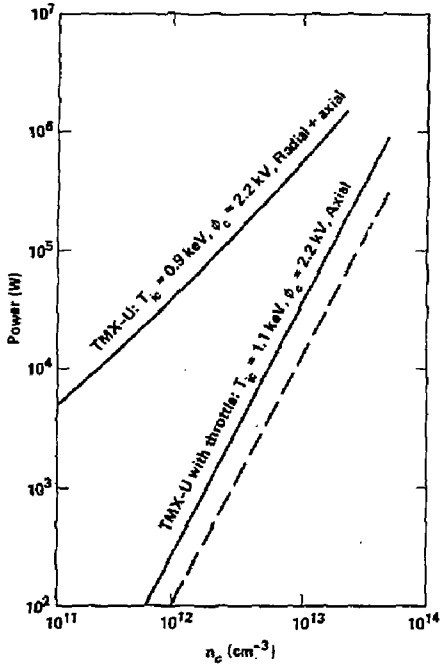

Fig. 2.4 -3. Power-density curve after thermal barrier formation (with throttle coil). Dashed line shows the power requirements to heat only the 17-cm-radius core. The solid lines include heating the halo out to a radius of 28 cm with the throttle coil and to 33 cm without the throttle coil.

The central-cell power requirements with the throttle coil are reduced for several reasons:

- Radial diffusion is substantially reduced.
- Plasma length is reduced by a factor of 260/508 cm.
- Total plasma radius is reduced from 33 to 28 cm; ICRH is expected to heat the boundary plasma in addition to heating the 17-cm-radius core. The power requirements are shown in Fig. 2.4-3 for heating the 17-cm-radius core plasma and for heating the entire 28-cm-radius total plasma column.
- The mirror ratio is increased from 6.7 to 15.
- Deuterium rather than hydrogen as assumed in Ref. 2.4.-1 decreases the power by a factor of $2^{0.5}$.
- The ratio of charge exchange to ionization is somewhat smaller for deuterium at the energies in TMX-U, so that less gas fueling is required and less power is expended in charge exchange.

The effect of radial diffusion is seen at high ion energies. With the throttle coil, axial losses dominate, so the power decreases with increasing T_{ic} (Fig. 2.4.-1). Whereas without the throttle coil, radial losses dominate so the power increases with T_{ic} (Fig. 2.4.-2). The power requirements on the ICRH system are substantially reduced by the throttle coil before thermal-barrier formation.

The higher central-cell density achievable before barrier formation may provide the option of start-up in the central-cell stand-alone mode.[2.4.-2] In this mode, start-up guns would provide preionization to be sustained by gas-box fueling and ICRH. The basis of the apparent MHD stability of this mode has not been established, but in recent experiments on the Phaedrus tandem mirror, stable operation is achieved in an axisymmetric geometry.[2.4.-3] This would provide for more efficient use of the ECRH gyrotrons (compared with using ECRH for preionization as well as heating) by forming a dense plasma in the central cell before beginning to heat the low-density flowing plasma in the end cells. This start-up mode would be similar to that proposed for the MFTF-B A-cell configuration.[2.4.-4]

Similar reductions are also found after barrier formation (Fig. 2.4-3). Axial power losses with a thermal barrier are expected to be reduced from

those of TMX-U without the throttle coil by a factor of about 3. This is due primarily to the reduction in length and the change from hydrogen to deuterium. The largest reduction is expected to be in radial diffusion, which is taken to be zero in the throttle-coil power balance computations shown in Fig. 2.4-3. While some radial diffusion can be expected to increase the power requirements beyond those shown, two other effects should reduce the power requirements. First, the model used[2.4.-1] assumes that, with a thermal barrier, the effective mirror ratio is for the field at the potential peak compared to that at the central-cell midplane; thus ignoring any improvement in confinement because of the throttle coil. The second effect is that the gas-box efficiency has been higher in TMX-U than the $\Gamma = 2$ found in TMX[2.4.-1]. Thus decreased charge-exchange losses are expected.

A second frequency range might enable all the central-cell heating to be done with ICRH. Fundamental heating (ω_{ci}) is required for start-up and is expected to heat to densities approaching 1×10^{13} cm^{-3} where the fast wave begins to propagate. Above a density of 3×10^{12} cm^{-3}, the second harmonic ($2\omega_{ci}$) will propagate and will heat an energetic-ion tail. This will equilibrate with the bulk in a way similar to energetic ions from neutral-beam heating.

REFERENCES

2.4.-1. A. W. Molvik and S. Falabella, Use of ICRH for Startup and Initial Heating of the TMX-U Central Cell, LLNL Report, UCID-19342 (May 1982).

2.4.-2. J. R. Ferron et al., Bull. Am. Phys. Soc. 27, 958 (1982).

2.4.-3. N. Hershkowitz, University of Wisconsin, private communication (December 1982).

2.4.-4. D. L. Correll "Startup Scenario for a Positive-Potential MFTF-B," in Mirror Fusion Quarterly Report, LLNL Report, UCRL-50051-81-3, (1981), p. 43.

3. PHYSICS ISSUES

3.1. MHD STABILITY

W. E. Nexsen and R. L. Wong

Recent developments in tandem mirror MHD theory and the understanding of the role that hot electrons play in modifying the MHD response were applied to the magnetic field design of TMX-U with throttle coils. In addition, plasma-pressure profiles, which better approximate the output of the Fokker-Planck runs, have been incorporated in the stability calculations. The stability boundaries for the 0.4-tesla central-field reference case are given in Fig. 3.1-5.

3.1.1. Introduction

Basic tandem-mirror MHD stability (i.e., the demonstration that proper pressure weighting of regions of good curvature can stabilize bad-curvature regions against flute interchange modes) was demonstrated in TMX and in the initial TMX-U operation.[3.1.-1,-2] In TMX-U the role that hot electrons play in the MHD equilibrium and stability aspects of tandem mirrors will be explored. With the addition of throttle coils to TMX-U, new regions of bad curvature and the possibility of trapping plasma in the transition regions will modify the MHD stability boundaries from their standard TMX-U values; however, no new MHD stability issues are expected to be encountered.

3.1.2. Recent Developments in MHD Stability Theory

Some recent developments in tandem-mirror MHD theory yielded more favorable ballooning-stability boundaries than those previously obtained. These new developments follow from attempts to incorporate finite-Larmor-radius (FLR) corrections. Calculations that include the FLR effects in the large, but finite, mode number limit[3.1.-3] show that typical tandem configurations would be stable down to mode numbers so small as to violate this eikonal approximation. In addition, only the lowest order modes have been observed experimentally in TMX[3.1.-4] and Phaedrus.[3.1.-5]

These results suggest that the only important perturbation to consider is a rigid displacement of the plasma cross section[3.1.-6] i.e., a perturbation in

which the MHD displacement varies only as a function of distance along the magnetic axis. With such a perturbation there are no FLR effects because both ions and electrons experience the same average force. One can apply an energy principle to this perturbation to obtain Euler-Lagrange equations identical to the "infinite-m", zero Larmor radius, ballooning-mode equations of marginal stability except for the presence of an extra field-line bending term and the substitution of radial averages of $Q = B^2 + P_\perp - P_\parallel$ and $p = 1/2\ (p_\perp + p_\parallel)$ for peak values. The extra term that arises from the perturbation of the magnetic field in the vacuum beyond the lateral boundary of the plasma is strongly stabilizing, leading to stability predictions closer to interchange than to ideal MHD ballooning. The vacuum bending energy is furthur increased if there is a conducting wall near the plasma; the maximum stabilizing effect of the wall occurs when it coincides with the plasma boundary. In that case the mode becomes flute-like, with a critical beta equal to the interchange limit.

A furthur development has been the inclusion of the effects of finite-beta distortions in the equilibrium flux-line geometry.[3.1.-7] This, at the present, is limited to an assumed flat radial-pressure profile.

3.1.3. Pressure Distribution Modeling.

The MHD-stability calculations require the proper modeling of the plasma-pressure variation with magnetic field in the various regions of the tandem mirror. In the TMX-U anchors, the majority of the pressure will be due to the hot-mirror-contained electrons in the thermal barriers. We first examine whether these hot electrons have a fluid MHD response or whether they are "rigid", in which case the effective pressure is less than the calculated value.

For a tandem mirror, the condition that the electrons give a fluid response is given by[3.1.-8]

$$|\omega_{kh}| \ll |\omega^*_{icc}| \quad , \tag{3.1.1}$$

where ω_{kh} is the hot-curvature-driven-drift frequency of the hot electrons in the anchor and ω^*_{icc} is the diamagnetic-drift frequency of the central-cell ions. This condition reduces to

$$E^\perp_{he}/E^\perp_{ic} \ll R_c/r_A \quad , \tag{3.1.2}$$

where $E_{he}^{\perp}$ is the hot-electron perpendicular energy, $E_{ic}^{\perp}$ is that of the central-cell ions, R_c is the field line radius of curvature in the anchor, and r_A is the plasma radius. For the TMX-U anchors, $R_c \simeq 850$ cm at $r_A = 15$ cm, yielding $E_{he}^{\perp}/E_{ic}^{\perp} << 57$ for the hot electrons that are to be treated as a fluid. For Reference Case C the point design value of $E_{ic}^{\perp} \simeq 4.5$ keV, requires $E_{he}^{\perp} << 250$ keV. Since $E_{he}^{\perp}$ is estimated to be of the order of 60 keV for this case, this condition is met and all of the hot-electron pressure contributes to stabilization.

The pressure variation in the anchors is modeled for the stability calculations by the expressions,

$$P_{\parallel} = P_A \, (1 - B/B_m)^2 \quad , \tag{3.1.3}$$

$$P_{\perp} = P_A \, [1 - (B/B_m)^2] \quad , \tag{3.1.4}$$

where B_m is the lower of the two mirror-field values. Since the pressure is the sum of the contributions of the hot electrons and sloshing ions (which have a different variation with B), the above expressions are compromises that approximately conform to the sum of the outputs of the Fokker-Planck ions for hot electrons and sloshing ions. For TMX-U, we estimate that the above pressure models result in a stability integral value

$$I = \int_{plug} \frac{P_{\perp} + P_{\parallel}}{B} \, \mathcal{R} \, dz \quad ,$$

which is approximately 10% higher than the value obtained if the Fokker-Planck values are used.

In the pumped transition region we model the pressure of the passing ions plus the barely trapped ions by the relations

$$P_{\perp} = P_c \, (B/B_T)^2 \quad , \tag{3.1.5}$$

$$P_{\parallel} = P_c \, [2 \, (B/B_T) - (B/B_T)^2] \quad , \tag{3.1.6}$$

where B_T is the throttle coil-peak value and P_c is the pressure of the thermal component of the central-cell ions. A mirror distribution, similar to that used in the anchor, models the pressure of the deeply trapped ions.

For the reference-case neutral-beam-heated central cell much of the plasma pressure is due to an energetic mirror-confined ion component. A thermal-pressure component, whose value in the central-cell midplane is ~15% of the mirror-confined value, is also predicted by the Fokker-Planck runs to be present. We model the central-cell plasma pressure by

$$P = P_0 (1 - B/B_T)^{10} (10(B/B_T) + 1) + P_c \quad , \tag{3.1.7}$$

$$P_{\parallel} = P_0 (1 - B/B_T)^{11} + P_c \quad . \tag{3.1.8}$$

When expressions are plotted (Fig. 3.1-1) and compared with reference case Fokker-Planck values, the fit is quite good.

3.1.4. Sensitivity Analysis

The MHD equilibrium and stability code is TEBASCO, which uses magnetic fields generated by the magnetic-design code EFFI and analytic expressions for the plasma pressure of the type described in Sec. 3.1.3. Here we examine the sensitivity of the MHD stability boundary to changes resulting either from the addition of the throttle coil or from the new developments in theory.

In Fig. 3.1-2, the finite-β, rigid, ballooning-mode-stability boundaries for several values of throttle coil field are compared with those of TMX-U in its present configuation. For these cases B_c is 0.3 tesla, and we assume a thermal central-cell plasma whose pressure is constant to the peak of the plug inner mirror, i.e., we assume that throttle coil transition regions are unpumped. The differences in the boundaries reflect the effect of the additional curvature introduced by the throttle coil and the new transition coil. For these ballooning calculations and those that follow, we assume for the wall location a value of $(r_w - r_p)/r_p = 1.62$, which best approximates the TMX-U conditions. Here, r_w is the radius of the wall at the central-cell field minimum and r_p is the plasma radius in the same plane.

In Fig. 3.1-3, we see the effect on the stability boundary of pumping the transition regions. The parameter $\langle\beta_T\rangle$ is the value of the radially averaged beta of the deep mirror-trapped ions at the field minimum in the transition region. Repeated for comparison is the 6-tesla unpumped case

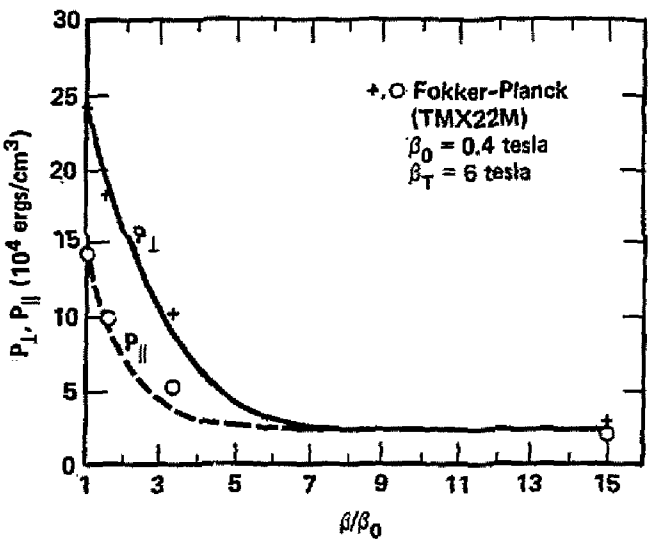

Fig. 3.1-1. Analytic fit to the reference-case Fokker-Planck central-cell pressure distribution. For discussion see Sec. 3.1.3.

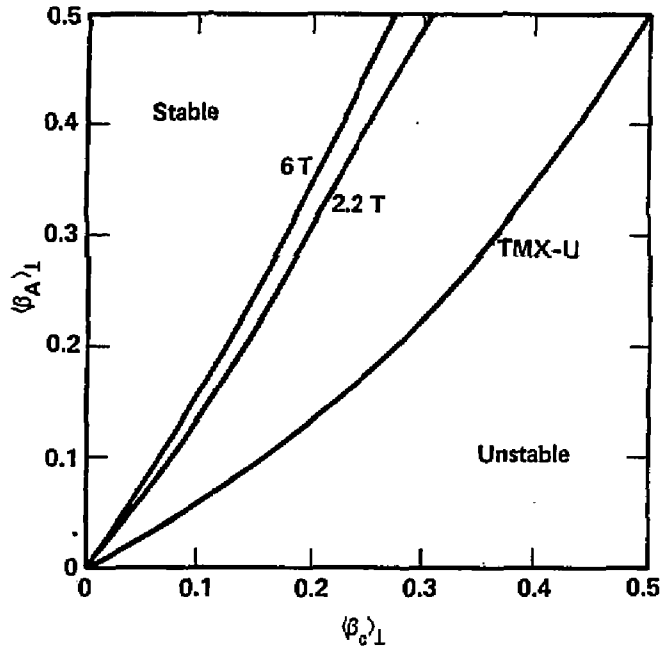

Fig. 3.1-2. Marginal stability boundaries for finite β, rigid, ballooning modes in TMX-U in its original configuration and for two values of the throttle coil peak field. The value of perpendicular beta in the MHD anchor, $\langle\beta_a\rangle_\perp$, required to stabilize a given beta in the central cell, $\langle\beta_c\rangle_\perp$, is shown as a function of $\langle\beta_c\rangle_\perp$. The transition regions are unpumped and a constant pressure extends to the peak of the inner mirror of the anchor. The equilibrium is stable to the left of the curves.

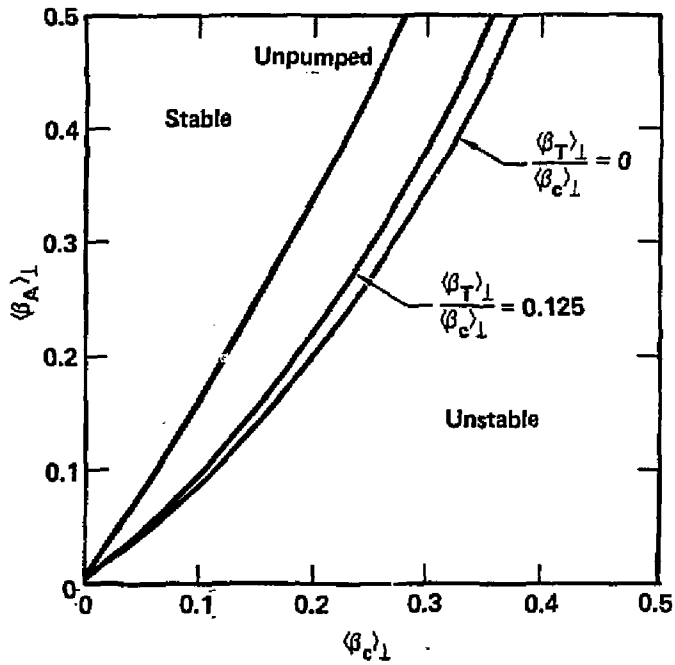

Fig. 3.1-3. Effect of pumping transition region on finite β, rigid, ballooning-mode-stability boundary for TMX-U with a 6-tesla throttle coil field and thermal central-cell pressure distribution; $\langle\beta_T\rangle_\perp$ is the perpendicular beta of the deep mirror-trapped ions in the transition region.

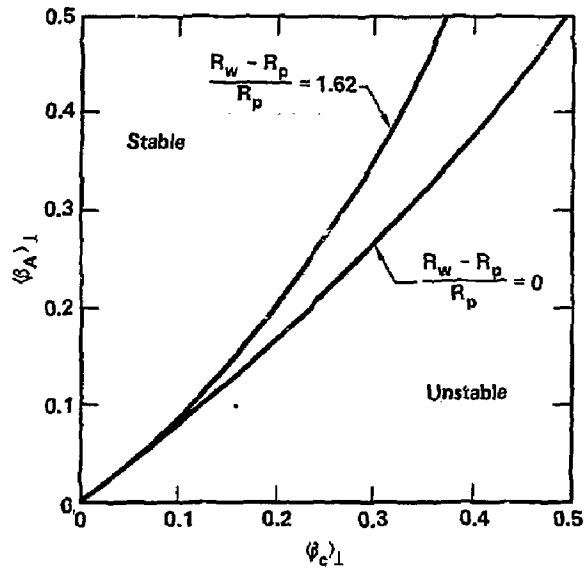

Fig. 3.1-4. Effect of wall position on finite β, rigid, ballooning-mode-stability boundary for TMX-U with a 6-tesla throttle coil field, a fully pumped transition, and a thermal central-cell pressure distribution.

from Fig. 3.1-2. In addition we plot the boundary for a fully pumped transition, $\langle\beta_T\rangle / \langle\beta_{cc}\rangle = 0$, as well as for an intermediate value, $\langle\beta_T\rangle / \langle\beta_{cc}\rangle = 0.125$. The improvement in the stability boundary for the pumped case is due to the reduction of the plasma pressure in the regions of bad curvature in the transition. For proper throttle coil operation, we expect pumping to reduce the pressure of the deeply trapped ions in the transition region to a very small value. Consequently, for the remaining plots we will show only the fully pumped case.

The effect of conducting walls on the stability boundaries is shown in Fig. 3.1-4, where we compare the ballooning limit with the flute limit obtained if the wall radius equals the plasma radius. As expected, the ballooning limits and flute limit are the same at low values of beta but diverge as beta increases.

3.1.5. Reference Case Stability Boundary

Using the analytic expressions of Sec. 3.1.3 for the pressure weighting of the Reference Case C (6-tesla throttle, 0.4-tesla central field, neutral-beam heated central-cell plasma, and fully pumped transitions) in TEBASCO, we compute the stability boundary. We then raise the stability boundary by 10% to compensate for the overestimate of the anchor stability caused by the use of the analytic pressure distribution rather than the Fokker-Planck distribution (see discussion in Sec. 3.1.3), and we obtain Fig. 3.1-5 as our best estimate of the Reference Case C stability boundary. For this case, the peak central-cell density is predicted to be 4.0×10^{13} with average ion-perpendicular energy of 4.5- and 0.7-keV electron temperature, yielding a peak perpendicular beta of 50% or, for a parabolic radial-pressure profile, an average perpendicular beta of 25%. For stability, we require an average plug-perpendicular beta greater than 22% and peak greater than 44%. In the anchor central plane the ions contribute less than 2% to the peak-perpendicular beta so we require for a peak hot-electron density of 4×10^{12} an average perpendicular energy of the order of 60-keV for MHD stability. For Reference Case D, if we assume that the same stability boundary applies, we find that a peak hot-electron density of 4×10^{12} will require an average perpendicular energy of the order of 30-keV for stability.

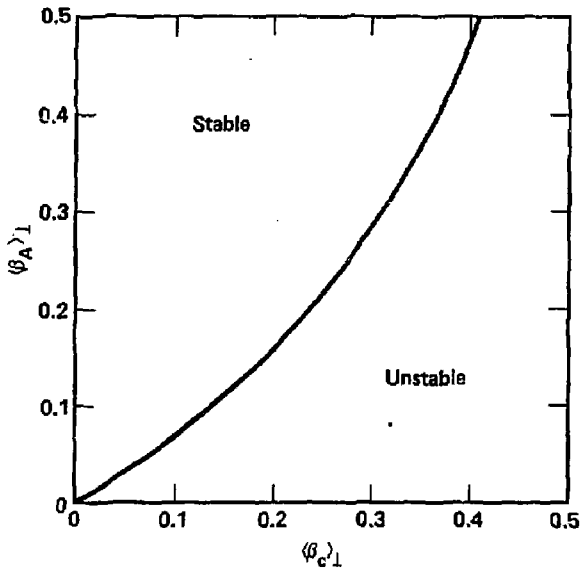

Fig. 3.1-5. Finite β, rigid, ballooning-mode-stability boundary for a beam-heated TMX-U central-cell plasma with a 6-tesla throttle coil, a 0.4-tesla central-cell field, and fully pumped transitions. Central-cell thermal beta is 15% of the beam-injected beta.

REFERENCES

3.1.-1. W. E. Nexsen in Summary of Results from the Tandem Mirror Experiment (TMX) T. C. Simonen, Ed., LLNL Report, UCRL-53120 (1981), Section 8.

3.1.-2. T. C. Simonen et al., TMX-Upgrade (TMX-U) Operation in the Sloshing-Ion Mode, LLNL Report, UCID-19568 (1982).

3.1.-3. W. M. Nevins and L. D. Pearlstein, in Physics Basis for an Axicell Design for the End Plugs of MFTF-B, D. E. Baldwin and B. G. Logan, Eds., LLNL Report, UCID-19359 (1982), Appendix B.

3.1.-4. T. A. Casper and E. B. Hooper, in Summary of Results from the Tandem Mirror Experiment (TMX), T. C. Simonen, Ed., LLNL Report, UCRL-53120 (1981), Section 11. E. B. Hooper, Jr., J. Foote, and G. Hallock, to be published in Phys. Fluids.

3.1.-5. R. Bruen, S. N. Golovato, L. Yuijiri, B. McVey, A. Molvik, D. Smatlak, R. S. Post, D. K. Smith, and N. Hershkowitz, "Experiments in a Tandem Mirror Sustained and Heated Solely by rf," Phys. Rev. Lett., 26 1833 (1981).

3.1.-6. T. B. Kaiser, W. M. Nevins, and L. D. Pearlstein, LLNL Report, UCRL-88268; also L. D. Pearlstein, T. B. Kaiser, and W. A. Newcomb, "Analytic Equilibria with Quadrupole Symmetry in the Paraxial Limit," Phys. Fluids 24 (7), 1326 (1981).

3.1.-7. L. D. Pearlstein, LLNL, personal communication.

3.1.-8. D. E. Baldwin, "Some Effects of Hot Electron Stability in Tandem Mirror Geometry," in Mirror Theory Monthly, LLNL (February 15, 1982).

3.2. PARALLEL CURRENTS

W. C. Turner and R. L. Wong

Because the divergence of the diamagnetic current is not everywhere equal to zero in a nonaxisymmetric linear device, currents exist that are flowing parallel to the magnetic flux lines in a tandem mirror stabilized with quadrupole end plugs.[3.2.-1] In the central cell of a tandem mirror, parallel currents have the deleterious effect of giving rise to transverse magnetic-field components that distort magnetic-flux surfaces. In a long machine the distortions can become appreciable and even cause flux surfaces to intercept material walls unless the parallel-current drive is minimized during design. Fortunately, it is possible to control the magnitude of the parallel currents by judicious magnet design without unduly increasing the bad-curvature drive for MHD instability.

In the paraxial limit (radial scale length << axial scale lengths) and to first order in plasma pressure, the derivative of the parallel current density per unit magnetic flux ($j_{\parallel}/B$) is given by[3.2.-1]

$$\frac{d}{ds}\frac{j_{\parallel}}{B} = \frac{1}{B}\left[\frac{\partial}{\partial\psi}\left(P_{\perp} + P_{\parallel}\right)\right] \cdot \text{HO} \,, \tag{3.2.1}$$

where ψ is the flux coordinate and HO is the geodesic curvature (geodesic curvature lies in a magnetic flux surface while normal curvature is perpendicular to a flux surface). For quadrupole symmetry the geodesic curvature can be written as

$$\text{HO} = \psi\, g(z) \sin 2\theta \,, \tag{3.2.2}$$

where g(z) is related to the strength of the quadrupole field component. For a tandem mirror with opposite end plugs rotated 90° the function g(z) is odd about the midplane z = 0 of the central cell. Because of this, integrating Eq. (3.2.1) between the outboard mirrors gives no net current flowing out of the device. For an isolated single-cell quadrupole, g(z) is also odd about the center of the quadrupole so no net axial currents flow out the ends. Joining a quadrupole to a central-cell solenoid, however, breaks the symmetry of the quadrupole so that axial currents may flow into the central cell.

As can be seen from Eq. (3.2.1), the key to controlling the axial extent of parallel-current flow is arranging nearby regions to have opposite signs of geodesic curvature that will tend to cancel one another when integrating along a magnetic-field line. This was recognized by Baldwin and Pearlstein in the design of the transition section for the MFTF-B axicell design.[3.2.-2] Recircularizing a flux tube as it leaves the inboard mirror of an end plug and enters the axially symmetric central cell necessarily introduces relatively large geodesic curvature. To balance this out, in the MFTF-B axicell designs, it was necessary to introduce two transition quadrupoles to fan the flux tube in opposite directions. A similar solution was adopted for the TMX-U throttle coil design in which a transition quadrupole, in addition to the existing one, was added. However, because of space limitations the cancellation of regions of opposite geodesic curvature will not be as good as achieved in the MFTF-B axicell design.

Figures 3.2.-1 to 3.2.-3 show some computational results related to parallel currents in the TMX-U throttle coil design. These results were obtained for 6.0-T in the throttle coil, 0.4-T in the central cell, for central-cell beta peak $\beta_c = 0.40$, and for end-plug beta peak $\beta_p = 0.33$. The magnitude of the results were determined to be insensitive to 50% variations in these beta values.

The normal and geodesic curvature along the flux line $\psi = \psi_B$ (the flux where the plasma pressure vanishes, corresponding to $r_B = 20$ cm in the central-cell midplane), with $\theta = 45^0$, are shown as functions of axial position in Fig. 3.2-1. As was discussed, the geodesic curvature is odd about $z = 0$, has its largest values ($\kappa_0 \sim 0.2$) in the transition region, and nearly vanishes in the central cell. Geodesic curvature in the end plugs is much smaller than in the transition and odd about the end-plug midplanes. The largest peak in the geodesic curvature occurs just inside the inboard mirror of the end plugs, where the existing transition quadrupoles begin to recircularize the flux tube fan. Opposite sign peaks occur in the new transitions added near the outboard sides of the throttle coil but do not entirely compensate the larger peaks at the existing transitions. Shown in Fig. 3.2-2 is the parallel-current density per unit magnetic flux flowing along the same flux line as in Fig. 3.2-1. One can clearly see the imperfect current cancellation in the quadrupole end plugs and transition regions as finite parallel current flows from the plug to the transition and from the

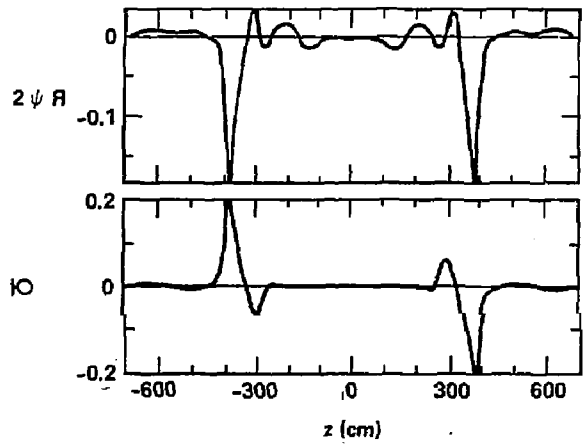

Fig. 3.2-1. Curvature versus axial position: normal curvature (top) and geodesic curvature (bottom). Positive normal curvature provides MHD stability.

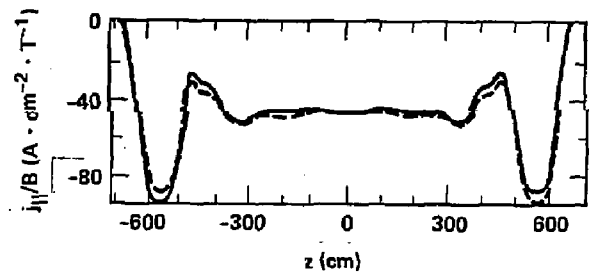

Fig. 3.2-2. Parallel current versus axial position.

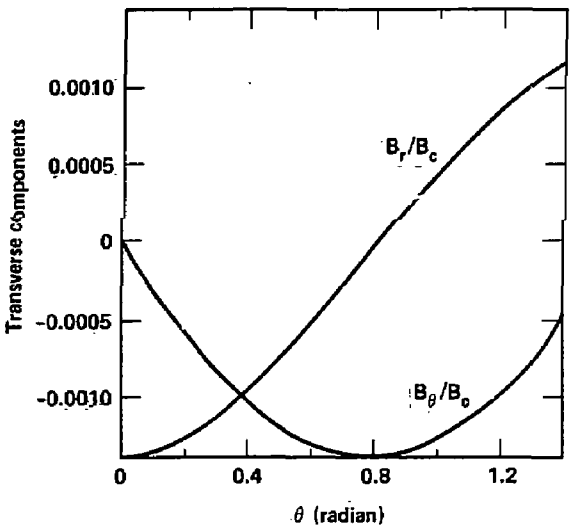

Fig. 3.2-3. Transverse components of magnetic field as functions of azimuth.

transition to the central cell. In the central cell, $j \sim 20$ amps/cm^2 for this case. In Fig. 3.2-3, we show the magnitude of the transverse components of B^+, normalized to the central-cell axial field B_c at $\psi = \psi_B$, $z = 0$, as functions of azimuthal coordinate θ from $\theta = 0$ to $\pi/2$. We find B_r and B_θ have the symmetry expected for axial quadrupole currents. For a central-cell field $B_c = 0.4$ T, the parallel-current-induced transverse components have magnitudes $B \sim 5 \times 10^{-4}$ T. For the TMX-U throttle coil design, transverse components of this magnitude perturb flux surfaces in the central cell by less than 1 cm and by themselves are benign. However, field components of this magnitude appear to be measurable and would constitute an important test of the existence of parallel currents. The magnitude of parallel currents is relatively insensitive to beta variations but quite sensitive to variations of transition-coil currents.

Aside from driving parallel currents geodesic curvature also enhances radial transport. This is discussed in Sec. 3.5.

REFERENCES

3.2.-1. L. D. Pearlstein, T. B. Kaiser, and W. A. Newcomb, Phys. Fluids 24, 1326 (1981).

3.2.-2. D. E. Baldwin and R. H. Bulmer, A Physics Conceptual Design for MFTF-B Transition Coil, LLNL Report, UCID-19562 (Aug. 1982).

3.3. STABILITY TO ELECTROSTATIC BALLOONING (TRAPPED-PARTICLE) MODES.

E. B. Hooper, Jr.

Control of trapped particle modes [3.3.-1,-2] is a significant constraint on tandem mirror design.[3.3.-3] Theory, described here, predicts that TMX-U with a throttle coil can be operated both in stable and unstable regimes. These experiments will thus provide a definitive test for electrostatic ballooning modes which are predicted to grow in the central cell at rates approaching MHD.

The TMX-U geometry with a throttle coil responds to the trapped particle modes in the same manner as the MFTF-B axicell configuration in that stability is provided by a coupling to drift waves because of the differences in turning points of the passing electrons and ions. For trapped-particle modes, the primary significant difference between MFTF-B and TMX-U experiments is the absence (in TMX) of the potential maximum in the axicell that reduces the number of passing particles below those that are due to the magnetic mirror. The reduction in passing particles by the throttle coil will provide a much more stringant test of trapped particle theory than is possible without the coil.

The trapped-particle analysis[3.3.-1,-2] follows that for MFTF-B.[3.3.-3] The m = 1 mode is expected to be the most unstable. Stability to the mode requires that

$$\frac{\omega_{*i}^2}{\gamma_c^2} > \frac{4(1 + A_r)}{A_r^2} \quad , \tag{3.3.1}$$

where ω_{*i} is the diamagnetic-drift frequency, γ_c the MHD growth rate of the central cell, and

$$A_r = \frac{1}{k^2 \rho_i^2} \frac{2 \int_{T+A} \frac{d\ell}{B} n_i^{pass}}{\int_c \frac{d\ell}{B} n_c}$$

$$\simeq \frac{r_c^2}{\rho_i^2} \frac{2(L_A + L_T)}{L_c} \frac{B_c}{B_A} \frac{n_i^{pass}}{n_c} \quad , \tag{3.3.2}$$

with $\rho_i^2 \approx T_i/(M_i\omega_{ci}^2)$. Also, in Eq. 3.3.2 L_A, L_T, and L_c are the lengths of the anchor, transition, and central cell; n_i^{pass} and n_c are the passing and central-cell densities.

In TMX-U we have L_c = 4.2 m, L_A = 3 m, and L_T = 1.9 m, B_c = 0.3 T, and B_a = 0.5 T to yield

$$A_r = 3.9\left(\frac{r_c^2}{\rho_i^2}\right)\left(\frac{n_i^{pass}}{nc}\right). \tag{3.3.3}$$

Using typical parameters (r_c = 20 cm, ρ_i = 1.5 cm, 1.5 keV; and n_i^{pass}/nc = 1/2 R = 1/40), we estimate A_r = 17.3, so stability is predicted for $\omega_{*i}^2/\gamma_c^2 > 0.24$.

In the limit $A_r \gg 1$, condition 3.3.1 becomes

$$\frac{\omega_{*i}^2}{\gamma_c^2} > \frac{4}{A_r}\ . \tag{3.3.4}$$

We have A_r given by Eq. 3.3.3,

$$\omega_{*i} = \left(\frac{1}{M\omega_{ci}}\right)\left(\frac{1}{nr_c}\right)\left(\frac{dp}{dr_c}\right) \simeq \left(\frac{\rho_i^2\,\omega_{ci}}{r_c^2}\right)$$

and

$$\gamma_c^2 = \frac{2\rho_i^2\,\omega_{ci}^2}{L_{cTr}}\ .$$

The value of L_{cTr}, which is the length of bad curvature in the central cell, actually depends on the pressure weighting of the curvature. The TEBASCO code was run in two limits to evaluate the MHD growth rate: For a thermal plasma L_{cTr} = 32 cm, and for a purely sloshing-ion plasma L_{cTr} = 70 cm.

Equations 3.3.4 and 3.3.2 yield the stability condition:

$$\frac{n_i^{pass}}{n_{ic}} > \frac{r_c^2}{L_{cTr}\,(L_A + L_T)}\,\frac{B_A}{B_c}\ . \tag{3.3.5}$$

Thus, for a thermal central cell-plasma, $n_i^{pass}/n_c > 0.04$ for stability, where as for a central cell with beta dominated by sloshing ions, $n_i^{pass}/n_{ic} > 0.02$. The passing to central-cell density at the mirror peak is $n_i^{pass}/n_{TH} = B_c/2B_{TH}$; for $B_c = 0.4$ T and $B_{TH} = 6$ T, $n_i^{pass}/n_{TH} = 0.03$. Thus the purely thermal case is predicted to be unstable by a small amount. The beam-injected case is predicted to be stable if the thermal density at the throttle coil is greater than 30/51 or 0.6 of the central-cell sloshing density. The experiment, however, has considerable flexibility for varying the operating conditions; e.g., using $n_i^{pass}/n_{ic} = 1/2$ R, condition (Eq. 3.3.5) can be written as

$$\frac{n_{TH}}{n_{ic}} \cdot \frac{B_c^2}{B_A B_{TH}} > \frac{2r_c^2}{L_{cTr}(L_A + L_T)} \sim \begin{cases} \frac{1}{20} \text{ (thermal)} \\ \frac{1}{43} \text{ (sloshing)} \end{cases} ,$$

which can be achieved by varying either B_c or B_{TH}. For example, for a thermal central cell at $B_{TH} = 6$ T, stability is achieved for $B_c = 0.39$ T, slightly below base operating conditions of 0.4 T.

The experiment will permit a wide range of magnetic fields and thus stability conditions, as shown in Table 3.3.1. We see that $B_c^2/B_A B_{TH}$ ranges from $(62.5)^{-1}$ to $(4.4)^{-1}$ and thus includes the values predicted for marginal stability. In the throttle coil geometry TMX-U will, therefore, permit stable operation to test thermal-barrier concepts in the tandem mirror, including a axisymmetric central cell, and also permit tests of trapped-particle theory by varying operating parameters.

Table 3.3-1 Values of $B_c^2/B_A B_{TH}$ that can be achieved in the throttle coil experiment with B_A = 0.5 T. These values can be used in Eq. (3.3.6) to determine the density ratio, n_{TH}/n_{ic}, required for stability.

	B_{TH}			
B_C	2.2	3	4	6
0.2	0.036	0.027	0.020	0.013
0.3	0.082	0.060	0.045	0.030
0.4	0.145	0.107	0.080	0.053
0.5	0.227	0.167	0.125	0.083

REFERENCES

3.3.-1. H. L. Berk, M. N. Rosenbluth, H. V. Wong, T. Antonsen, and D. E. Baldwin, Fast-Growing Trapped-Particle Modes in Tandem Mirrors, Institute for Fusion Studies, University of Texas, Austin, TX, Report IFSR-59 (1982).

3.3.-2. L. D. Pearlstein, D. B. Baldwin, R. H. Cohen, T. K. Fowler, and B. G. Logan, "Stabilization of Tandem-Mirror Trapped-Particle Modes by Incomplete Cancellation of Trapped-Particle Drifts," presented at 1982 Sherwood Meeting, Annual Controlled Fusion Theory Conference, Santa Fe, NM, April 25-28, 1982.

3.3.-3. D. E. Baldwin, "Electrostatic Ballooning Modes', Appendix D in D. E. Baldwin and B. G. Logan, Eds., in Physics Basis for an Axicell Design for the End Plugs of MFTF-B, LLNL Report, UCID-19359 (1982), Appendix D.

3.4. CENTRAL-CELL MICROSTABILITY

T. A. Casper and G. R. Smith

The longer ion lifetime achieved by using the throttle coil impacts the microstability of the central-cell plasma. The preliminary analysis given here is based on our best knowledge (from Fokker-Planck calculations) of the ion distribution function $f(\underline{v})$. Improved knowledge of $f(\underline{v})$ will motivate an updated analysis of microstability. Such a future update is particularly important for the drift-cyclotron (DCI) and Alfvén ion-cyclotron (AIC) instabilities, which are quite sensitive to $f(\underline{v})$ and may occur in TMX-U, both without and with the throttle coil. The convectively unstable AIC mode is not expected to grossly affect confinement because of its limited spatial amplification. Additional physics is presently being incorporated into the DCI stability analysis. This mode, predicted to be unstable in past experiments, has not been observed experimentally.

Using the latest TMX-U Fokker-Planck calculations[3.4.-1] for the central cell (properly includes the confining potential and the R = 15 throttle coil effects), we observe nearly monotonically decreasing distributions $f_{\parallel}(v_{\parallel})$ and $f_{\perp}(v_{\perp})$ as shown in Fig. 3.4-1. Since a strongly double-humped perpendicular ion distribution does not result, we rule out the occurrence of the two-component[3.4.-2] (bump-on-tail) instability in the central cell.

The possibility also exists for three modes driven unstable by the radial density gradient. These three related modes are the drift-cyclotron loss-cone (DCLC) mode, the DCI instability, and the lower-hybrid-drift (LHD) instability. Since the expected perpendicular ion distribution is nearly monotonically decreasing (see Fig. 3.4-1a), we do not anticipate the presence of loss-cone-driven modes; specifically, neither the DCLC nor the axial loss cone (ALC, independent of the density gradient) modes should be present.

In the limit of a Maxwellian ion-velocity distribution, however, the DCLC mode becomes the DCI. It is driven solely by the radial density gradient and results from a coupling between ion-cyclotron waves (stable in a Maxwellian plasma) and drift waves propagating in the ion diamagnetic direction.

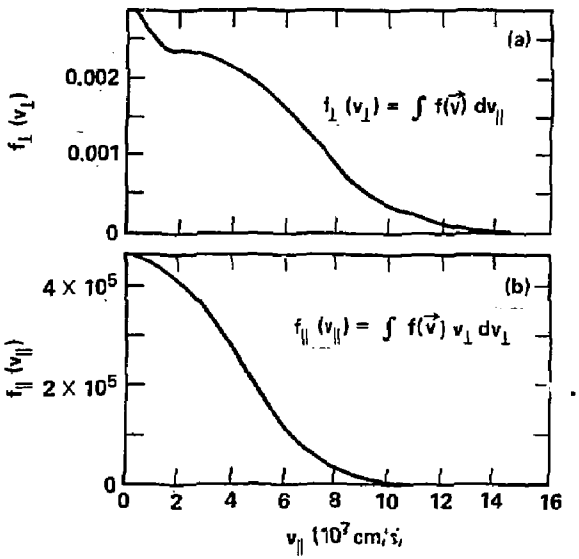

Fig. 3.4-1. Velocity distributions from TMX-U throttle coil Fokker-Planck calculations: (a) perpendicular and (b) parallel ion-velocity distributions.

According to a simple theory,[3.4.-3] stability is expected if

$$\frac{r_n}{\rho_c} > \frac{1}{2^{3/2}} \left(\frac{m_e}{m_i} + \frac{\Omega_i^2}{\omega_{pi}^2} \right)^{-1/2} ,$$

where r_n is the radial density-gradient scale length, ρ_c is the ion gyroradius, Ω_i is the ion-cyclotron frequency, and ω_{pi} is the ion-plasma frequency. For the proposed TMX-U throttle coil operating conditions, this reduces to $r_n/\rho_c > 21$ for stability. This is satisfied if the average ion energy of the central cell, $\bar{E}_{ic}$, is less than 251 eV. Since the expected energy $\bar{E}_{ic}$ is 5.5 keV it would appear that this mode is unstable. Note, however, that a similar calculation for the TMX central cell indicates it also was unstable but no evidence for this mode was ever observed in that experiment. We believe the simple theory uses an inadequate model for the central cell. We hope to obtain more realistic stability limits for the drift-cyclotron mode by including the additional physics of electron Landau damping, electromagnetic couplings, and radial gradients of temperature and magnetic-field strength.

A small level of collisions can destroy the cyclotron resonance leading to the DCI mode. In the limit where collisions become important, the DCI evolves to the LHD-instability.[3.4-4] Near maximum growth rate, this mode is unstable if

$$\nu_{ii}/\Omega_i > m_e/m_i \quad .$$

The TMX-U throttle coil parameters indicate that $\nu_{ii} \sim 129\ s^{-1} << (m_e/m_i)\Omega_i$. Thus, due to the low central-cell ion collisionality, the LHD-instability is not expected to occur.

The moderately high beta, $\beta_{cc} = 50\%$, leads to the possibility of an AIC instability.[3.4.-5] The longer ion lifetime and larger mirror ratio with the throttle coil allows pitch-angle scattering to build a broader pitch-angle distribution with the result that the throttle coil may improve stability to the AIC mode as compared to TMX-U.

Figure 3.4-2 shows theoretical convective-absolute stability boundaries for two different models of the pitch-angle dependence $G(\phi)$ of the ion distribution. For Fig. 3.4-2a we use a Gaussian model, $G(\phi) = \exp[-(\phi-\phi_0)^2/2\Delta^2] + \exp[-(\phi-180^0+\phi_0)^2/2\Delta^2]$, where $\phi \equiv \sin^{-1}(v_\perp/v)$ and, for TMX-U, $\phi_0 = 65^0$. At $\beta_\perp$ of 43% the instability is merely convective if $\Delta > 22^0$. An ion distribution with $\Delta = 22^0$ is similar to the distribution found in Fokker-Planck calculations (Fig. 3.4-3) except that the Fokker-Planck distribution extends further towards the loss-cone angle of 15^0 than does the $\Delta = 22^0$ distribution. The ion distribution found in the Fokker-Planck calculations is, therefore, merely convectively unstable.

The model distribution with $\Delta = 22^0$, $\beta_\perp = 43\%$, and $\bar{E}_{ic} = 5.5$ keV causes AIC convective growth with an e-folding length for the wave amplitude of 0.3 m. Since this length is a sufficiently large fraction of the 4-m distance between throttle coils, convectively growing waves will not degrade performance unless the axially propagating waves are somehow reflected back towards the center of TMX-U.

Figure 3.4-2b shows the convective-absolute stability boundary for another pitch-angle distribution $G(\phi)$, which is constant for $\phi_{edge} \leq \phi \leq 180^0 - \phi_{edge}$ and zero for other ϕ. If we take ϕ_{edge} equal to the loss-cone angle of 15^0 in TMX-U with throttle coils and thus obtain a distribution more stable than the Fokker-Planck distribution, the figure shows the plasma to be well into the convective region at any conceivable β. At $\beta_\perp = 43\%$ the convective-absolute boundary is at $\phi_{edge} = 25^0$, which is consistent with the results obtained with the first model for $G(\phi)$. Our conclusion is therefore confirmed that the Fokker-Planck distribution should be only convectively unstable.

Based on current theory and available Fokker-Planck runs, the central cell of TMX-U with throttle coils is predicted to be unstable to both the DCI and the AIC modes. However, since the DCI was predicted in the past to be unstable but was not observed, it is possible that improved stability analysis will provide a boundary sufficiently relaxed to actually indicate stability. Because of the possibility of a broadened ion distribution during throttle-coil operation, the AIC mode may be more stable than in TMX-U. Even though the AIC mode is convectively unstable, its presence may not be

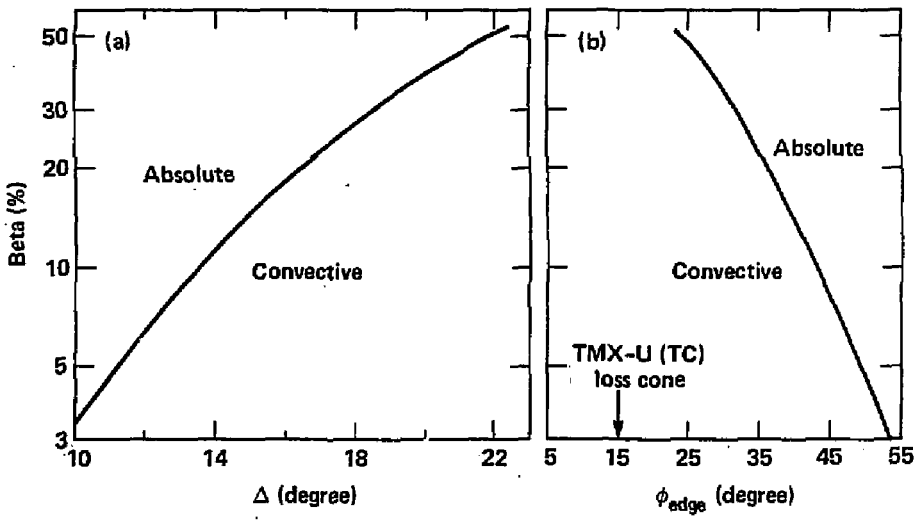

Fig. 3.4-2. The AIC convective-absolute stability boundaries for model distributions: (a) Gaussian angular distribution and (b) rectangular angular distribution. A comparison with the Fokker-Planck distribution indicates TMX-U at β_c = 50% operates well into the convective region for both model distributions.

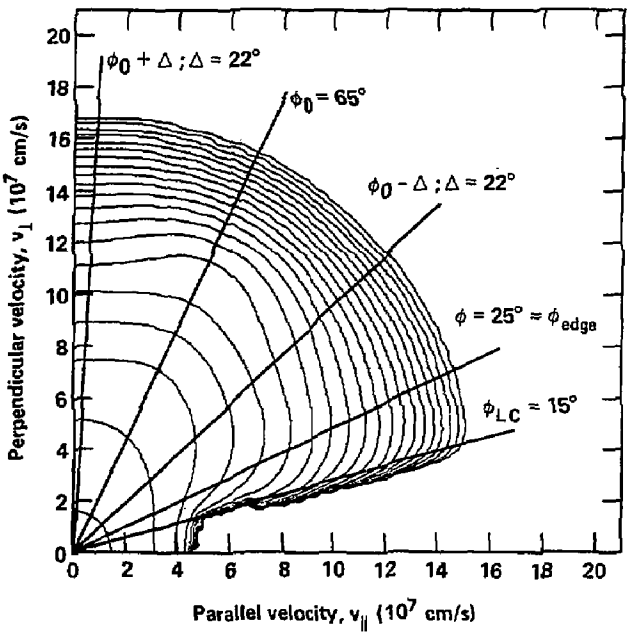

Fig. 3.4-3. Contours of $f(\underline{v})$ from Fokker-Planck calculations. This distribution has a greater spread than the model distributions and is therefore more stable.

detrimental to confinement. The mode observed in the TMX-U central cell during beam heating[3.4-6], which may be the AIC mode, does not appear to severely alter confinement. A detailed analysis using improved stability codes and Fokker-Planck runs specific to the operating conditions should be performed to refine the estimates.

For the lower-beta reference case, the conclusions reached for the DCI mode and the stability of the loss-cone modes remain virtually unchanged. For the AIC mode, we note from Fig. 3.4-2a that the lower-beta reference case ($\beta \approx 25\%$) requires a smaller Δ ($\approx 17^{o}$) to prevent absolute instability, and the AIC mode is less likely to occur than in the higher-beta case.[3.4.-5] We conclude, therefore, that microinstability is less of a problem in the lower central-cell beta case.

REFERENCES

3.4.-1. M. E. Rensink, LLNL, private communication.

3.4.-2. D. E. Baldwin, B. G. Logan, and T. C. Simonen, Eds., Physics Basis for MFTF-B, LLNL Report, UCID-18496 (1980), Part 2, p. IV-219.

3.4.-3. A. B. Mikhailovskii and A. V. Timofeev, Sov. Phys. JETP 17, 626 (1963).

3.4.-4. J. D. Huba and S. L. Ossakow, Phys. Fluids 22, 1349 (1979).

3.4.-5. T. A. Casper and G. R. Smith, Phys. Rev. Lett. 48, 1015 (1982).

3.4.-5. T. A. Casper, L. D. Pearlstein, and G. R. Smith, Bull. Am. Phys. Soc. 27, 1117 (1982); and G. R. Smith, W. M. Nevins, and W. M. Sharp, Bull. Am. Phys. Soc. 27, 1116 (1982).

3.5. RADIAL TRANSPORT

R. H. Cohen, J. A. Byers, and E. B. Hooper, Jr.

3.5.1. Introduction

The axisymmetric throttle coil limits the fraction of central-cell ions that sample the region of nonsymmetric magnetic field to $\sim 1/2\ R^{-1} = 0.03$. This reduces radial (resonant) transport of thermal central-cell ions by a factor > 5 relative to TMX-U without the throttle coil;[3.5.-1] the exact reduction depends on the radial electric fields in the two machines and lies between 5 and 30.

By isolating the bulk of the central-cell ions from the quadrupole regions that contain nonzero geodesic curvature, the throttle coil TMX-U models an essential part of the MFTF-B design. The experiment will provide a first test of transport theory in a regime in which radial transport is dominated by particles (the passing fraction) in a small part of phase space. Furthermore, because the predicted radial flux is small, searches may be made for anomalous transport mechanisms, if any.

The use of the throttle coil reduces the predicted radial transport to a sufficiently low level that axial processes will be the dominant losses in TMX-U. This occurs even though the high degree of geodesic-curvature balance in the MFTF-B plug has not been achieved in TMX-U. Because the particle motion is not stochastic for TMX-U parameters, even with the imperfect balance, much larger gains in confinement are achieved than would be possible in MFTF-B with a corresponding inbalance.

3.5.2. Application of Resonant Transport Theory to TMX-U.

The theory of resonant transport for a system with an axisymmetric throttle is described in a MFTF-B physics study.[3.5.-2] The first step was to determine whether the particle trajectories were stochastic. This was done in two ways: (1) Analytic approximations to the particle drifts were calculated, using various integrals of the field-line curvatures generated by the EFFI program and the electrostatic potential. The Cherikov stochasticity parameter K was calculated as in Ref. 3.5-2 ($K = 2\Delta\alpha_m\ \partial\Delta\beta/\partial\alpha$, where α,β denote the usual flux coordinates and $\Delta\alpha_m$ denotes the

azimuth-maximized value of $\Delta\alpha_*$.) A value K > 1 corresponds to intrinsic (collisionless) stochasticity. For these calculations, a model electrostatic potential

$$\phi\ (r,z) = \Phi(z)\ \frac{e^2 - e^{2r^2/r_H^2}}{e^2 - 1} \tag{3.5.1}$$

is used. For TMX-U parameters (with the radius r_H taken to be 25 cm), K reaches a broad, shallow maximum of about 0.95 at r ≈ 21 cm at B_c = 0.3 T. (2) Particle-guiding centers were followed numerically with the EFFI-generated magnetic fields. Particle trajectories were well-balanced (small, bounded oscillations in radius versus time) out to about 18 cm (Fig. 3.5-1a) but showed stochastic behavior (random, apparently unbounded radial motion) at larger radii (Fig. 3.5-1b). Given the degree of approximation made in evaluating K analytically, a 5 to 10% error is certainly within reason; thus we consider the analytic and numerical results to be in agreement.

Particle and energy transport can be expressed in the form[3.5.-1]

$$\Gamma_r = D_0 \left(\frac{\partial n}{\partial r} + \frac{nq}{T_i} \frac{\partial \phi}{\partial r} \right) + \frac{n}{T_i} \left(D_1 - \frac{3}{2} D_0 \right) \frac{\partial T_i}{\partial r} \tag{3.5.2}$$

and

$$Q_r = T_i \left[D_1 \left(\frac{\partial n}{\partial r} + \frac{nq}{T_c} \frac{\partial \phi}{\partial r} \right) + \frac{n}{T_i} \left(D_2 - \frac{3}{2} D_1 \right) \frac{\partial T_i}{\partial r} \right] . \tag{3.5.3}$$

The diffusion is found to be in the banana regime. The three diffusion coefficients are shown as a function of radial electric field in Fig. 3.5-2. Multiple resonances may be seen, for example in D_0, and yield a non monotonic dependence of D on E_r. The values given here are for $n_c = 1.7 \times 10^{13}$ cm^{-3}, T_i = 0.9 keV, and B_c = 0.3 T. The diffusion coefficients will scale approximately as ν_{ii} in the banana regime. The confinement time associated with resonant transport is a very weak function of central-cell magnetic field so that these estimates can be used for fields other than the assumed 0.3 T.

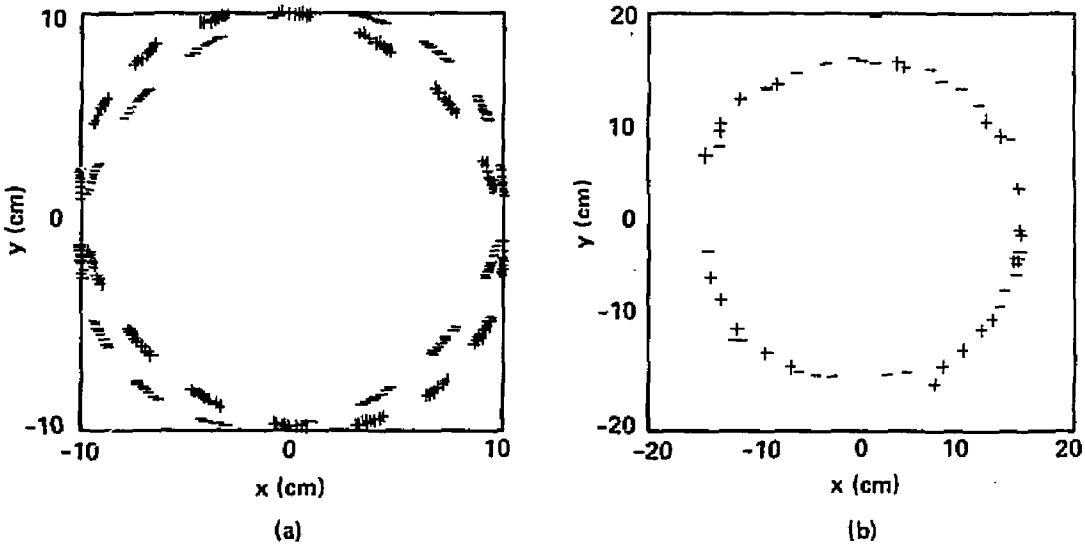

Fig. 3.5-1. Passing-particle orbit crossing x-y positions as the orbit crosses the midplane of the central cell. Positive-z and negative-z traveling orbits are shown with a plus or minus sign, respectively. (a) Nonstochastic initial radius at r = 10 cm. (b) Stochastic initial radius r = 17 cm. This particle is almost on the boundary between stochastic and nonstochastic behavior. After about 25 bounce periods it is lost radially. (Note the negative crossing at y ≈ 20 cm near x = 0.)

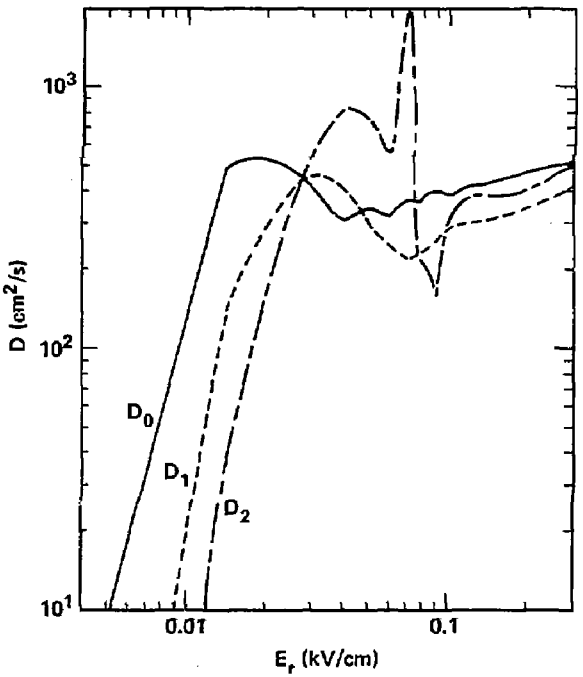

Fig. 3.5-2. Diffusion coefficients for resonant diffusion in TMX-U throttle (n_c = 1.7 x 10^{13} cm^{-3}, T_i = 0.9 keV, B_c = 3 kg).

To obtain an estimate of the particle-confinement time we replace gradients by an effective scale length, r_{eff}, [e.g., $n/(\partial n/\partial r)$] and define

$$\tau_2 = r_{eff}^2/\{D_o[(\phi_o/T_i r_{eff}) - 1/2] + D_1\} \quad . \tag{3.5.4}$$

The value of τ_2 is plotted in Fig. 3.5-3. The rapid increase in τ_2 below 0.03 kV/cm is due to a cancellation in the denominator of τ_2 associated with the temperature-gradient term in Eq. (3.5.2); one anticipates that the temperature-gradient will flatten out in that limit.

Operation of TMX-U will be at $E_r < 0.1$ kV/cm with corresponding radial confinement times because of resonant transport greater than 0.5 s. At a central-cell density of $\gtrsim 2 \times 10^{13}$ cm^{-3}, this corresponds to $n\tau > 10^{13}$ s cm^{-3}. Precise values will depend on density, temperature, and electric-field profiles.

3.5.3. Diffusion Caused by Particle Transitions.

When a particle scatters between trapped and passing orbits its radial excursion changes by some maximum amount, δr, because of the geodesic curvature in the quadrupole regions. This change causes a radial diffusion.[3.5.-3,-4]

Although a detailed theory has not been worked out, we estimate[3.5.-4] the diffusion coefficient as

$$D_o \sim \frac{(\delta r)^2}{4}\left(\frac{\nu_{ii}\nu_{\parallel}}{R\,L}\right)^{1/2} \quad . \tag{3.5.5}$$

From analytic analysis of the drift equations (confirmed by orbit calculations), we find $\delta r/r \approx 0.18$.

Choosing $n = 2 \times 10^{13}$ cm^{-3}, $T_i = 1$ keV, and $L = 1100$ cm (the plug-to-plug length); and with the mirror ratio $R = 20$, we estimate $D_o \sim 1.4 \times 10^3$ cm^2/s. This mechanism may, therefore, be the dominant mechanism here and in MFTF-B; if we take $r_{eff}^2 = 25$ cm, we estimate a confinement time $\tau \sim (25)^2/1.4 \times 10^3 = 0.45$ s, but with a significant uncertainty. This loss mechanism thus is slow on the time scale of the 75-ms experiment. The diffusion coefficient will scale as B_c^{-2}, so that the process will become even less important at higher fields. Further analysis is required to evaluate this effect with more accuracy.

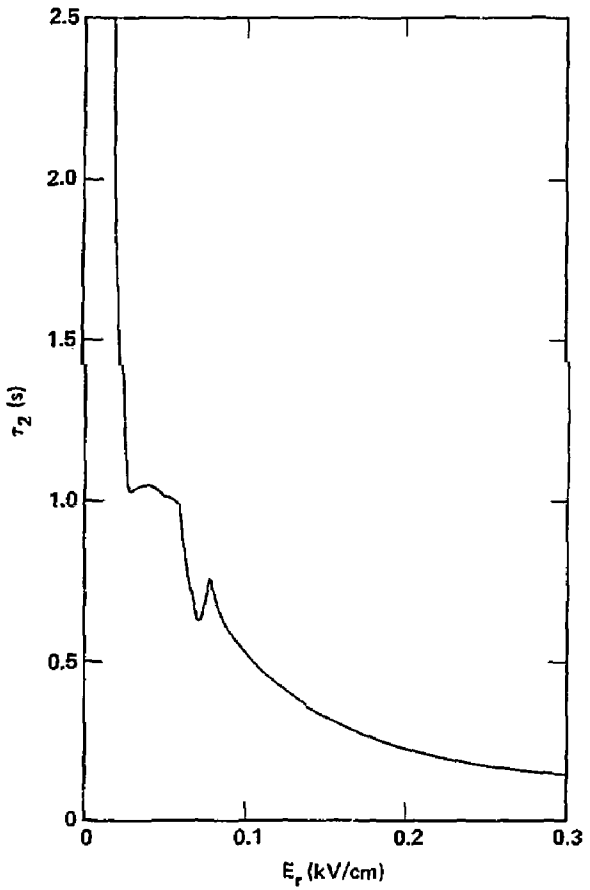

Fig. 3.5-3. Radial confinement time because of resonant diffusion in TMX-U throttle (n_c = 1.7 x 10^{13} cm^{-3}, T_i = 0.9 keV, B_c = 3 kg).

3.5.4. Other Transport Mechanisms

The ambipolar diffusion coefficient resulting from electron-ion collisions is given approximately by $\nu_e^2\nu_{ei}/\omega_{ce}^2 \approx 50$ cm^2/s at $n = 2 \times 10^{13}$ cm^{-3} and $T = 10^3$ eV and is, thus, about an order of magnitude less than resonant diffusion. It can thus generally be neglected in the TMX-U with the throttle coil.

Transport arising from ion-neutral collision is dominated by mobility resulting from charge-exchange. The transport is given by $(e\nu_{cx}/M_i\omega_{ci}^2)E_r$, with $\nu_{cx} = N_o \langle\sigma v\rangle_{cx} \approx 10^{-7}N_o$; N_o is the neutral density. For comparison with previous results, define an equivalent diffusion coefficient $D_{eq} = v^2\nu_{cx}/\omega_{ci}^2 \approx 5 \times 10^{-7}\ N_o$. This will be small compared to resonant transport if $N_o \ll 10^9$ cm^{-3}; at a halo attenuation of 3×10^2, this corresponds to a neutral density of 3×10^{11} cm^{-3} (10^{-5} Torr) outside the plasma. Reduction of the central-cell neutral density below this value will make the effect unimportant.

REFERENCES

3.5-1. J. H. Foote, A. K. Chargin, R. H. Cohen, T. B. Kaiser, C. V. Karmendy, T. C. Simonen, and R. L. Wong, "TMX-Upgrade Magnet System--Design Characteristics and Physics Considerations," J. Fusion Energy 2(6), 385 (1982).

3.5-2. R. H. Cohen and J. A. Byers, in A Physics Conceptual Design for the MFTF-B Transition Coil, D. E. Baldwin and R. H. Bulmer, Eds., LLNL Report, UCID-19562 (1982), Appendix A.

3.5-3. P. B. Lysyanskii and M. A. Tinnov, Institute of Nuclear Physics, Siberian Division, Acad. Sci. USSR, Preprint 80-94, Novosibrisk.

3.5-4. J. A. Byers and R. H. Cohen, Am. Phys. Soc. 27, 1115 (1982).

3.6. TRANSITION AND BARRIER TRAPPED-PARTICLE PUMPING

E.B. Hooper, Jr., J. A. Byers, W.F. Cummins,
B.G. Logan, and Y. Matsuda

3.6.1. Introduction

Both the plug and transition sections in TMX-U have axial minima in the magnetic field. It is important to maintain the density of warm ions considerably below the thermal equilibrium value in both regions. Warm ions trapped in the plug will fill in the thermal barrier, eliminating the isolation between central-cell and plug electrons that is required for the generation of a large confining potential. In the transition, trapped ions sample a large (bad) curvature region and thus reduce the maximum central-cell beta that can be achieved. In addition, if the transition fills up, pumping requirements in the plug will not be reduced by the large mirror ratio caused by the axisymmetric coil but rather will be determined by the mirror between the transition and the plug.

The primary source of trapped ions is the passing-ion population. Coulomb collisions among passing ions and between passing and trapped ions may cause passing particles to scatter into the trapped part of phase space. In addition, charge-exchange of passing ions will generate low energy ions which may be trapped. For this process to be unimportant, it is necessary that

$$n_0 \langle \sigma v \rangle_{cx} \ll \nu_{ii} \quad .$$

With $\langle \sigma v \rangle_{cx} \sim 10^{-7}$ cm^3 s^{-1} and $\nu_{ii} = 5.0 \times 10^{-8}\, n^{pass}\, \ell n\, \Lambda / T_i^{3/2}$, this yields

$$n_0 \ll 10\, n_{pass}\, T_i^{-3/2} \quad .$$

Estimating $T_i \sim 10^3$ eV and $n_n^{pass} = 5 \times 10^{11}$ cm^{-3}, we require $n_0 \ll 1.6 \times 10^8$ cm^{-3}. At a halo attenuation of 300, the gas pressure outside the plasma thus must be $p(D_2) \ll 1.4 \times 10^{-6}$ Torr for trapping by charge-exchange to be negligible. If this pressure is not

achieved, trapped-ion pumping beyond that calculated from Coulomb collisions will be required . In the following, we assume that adequate pressure is achieved in the experiment.

Three methods of trapped-particle pumping were considered for TMX-U. Neutral beams are used in the base case and are discussed in detail later.

- Neutral-beam pumping. Charge-exchange between trapped ions and energetic neutrals will produce an ion that leaves the field minimum if the energy parallel to the field is large enough. This mechanism was suggested in the original thermal-barrier proposal[3.6.-1] and is used in TMX-U operation in the absence of a throttle coil. It is concluded that adequate pumping can be achieved with two pumping beams (18^{0} beams) arranged as on the non throttle coil experiment and two beams (9^{0} beams) aimed to pump the transition section.

- Drift pumping. Baldwin[3.6.-2] originally proposed removing trapped particles by radial transport induced by alternating magnetic fields. The concept has been significantly improved[3.6.-3] by recognizing that resonances with bounce motion cause an amplification of the radial motion. An rf drive at a frequency near the bounce motion causes the radial excursion to accumulate over many bounces. The radial motion can be further increased by driving the oscillating $\underline{E} \times \underline{B}$ motion across the narrow fan in the magnetic-flux surfaces. Radial diffusion can be obtained by driving the motion with a range of frequencies. The result, described further in Appendix C.1, is an efficient pumping of trapped particles that can discriminate against passing particles with their significantly different bounce frequencies. Although the analysis of this technique is still incomplete, it potentially has three significant advantages: (1) little or no gas may be generated (beams generate gas at their dumps), (2) it works in the minimum of the magnetic field (unlike ICRH pumping), and (3) it may be able to pump impurity ions radially. This technique is now used in the MARS (reactor) reference case.

- ICRH pumping. This technique uses the large magnetic field of the throttle coil. Ions that are Yushmanov-trapped between the throttle coil and the plug potential are heated at high magnetic fields by ICRH. Although this heating technique heats ions primarily in the perpendicular direction, the large mirror ratio (5/1) between the ion-cyclotron resonance and the maximum

of the plug potential converts the energy to parallel motion, propels them over the potential, and expels them from the system. However, ICRH pumping does not work near the field minimum, and must be supplemented by pumping in this region.

Before evaluating these pumping techniques, we will discuss two general constraints on pumping. Drift and ICRH pumping are discussed in detail in Appendix C: Alternate Pumping Techniques.

(1) Threshold in pumping rate. The efficiency of pumping increases dramatically above a threshold level (a detailed example is given in Appendix B). The threshold occurs when the electrostatic-potential minimum becomes deep enough that energy scattering time to the bottom of the minimum is longer than the inverse-pump frequency. At pumping frequencies below the threshold, the potential well fills in with a near Maxwell-Boltzmann distribution. Because of the filling in, the potential is small and ion-ion collision frequencies large. Above the threshold, however, the filling in does not occur; the relatively large potentials lead to sloshing distributions for the trapped ions. As shown in the Appendix, the transition between the two regimes is abrupt. The TMX-U design provides pumping rates above this threshold.

(2) Pumping requirements at magnetic-field minima. Because passing particles are trapped by small-angle scattering, trapped particles initially slosh, with turning points high on the throttle magnetic mirror and the plug potential. Pumping at high magnetic field can thus remove trapped ions before they scatter enough to reach the field minima. Some particles, however, will leak through the pump and accumulate at the bottom of the well. If the only pumping is at the high-field point, the deeply trapped ions will reach the pumping volume only by scattering in angle and energy. As a result, the well will fill up until the potential difference between the minimum and the pump is $< T_i$. (Numerous runs with the Fokker-Planck code lead to this conclusion.) Pumping part way up the magnetic mirror can reduce the trapped particle fraction significantly at a beam energy below that required at the minimum.[3.6.-4] In the present scheme, however, we ensure that the wells will be pumped by requiring some pumping at the field minimum.

3.6.2 Neutral-Beam Pumping

Access for pumping neutral beam modules is available at three locations:

- 18^0 Pump Beams. The four ports used in the original TMX-U experiments are available for experiments with the throttle coil. The pumping frequency, $\sigma_{cx} j_b/e = 5 \times 10^3 j_b$, along the machine axis is shown in Fig. 3.6-1 for a single (18^0) pump beam located at one of these ports. The peak of the inner-plug mirror is at z = 407 cm; only a small part of the beam extends into the transition and essentially none to the transition midplane. These beams must consequently be supplemented by additional pumping in the transition region.

- 9^0 Pump Beams. These beams replace the 18^0 beams (using the same ports) but are smaller (10 A) and mounted at an angle, which permits penetration into the transition region. The 9^0 beams can be obtained by relocating a pump-beam module and a sloshing-beam module with internal masks; existing power supplies can also be used. The pumping frequency (on axis) is plotted in Fig. 3.6-2 for a single 9^0 beam.

- Axial Pump Beams. A second option for pumping the transition regions is to inject a beam up the axis of the device. The resulting pumping frequency is shown in Fig. 3.6-2. Note that the pumping frequency throughout most of the transition region is less than that for a single 9^0 pump beam; we will see that a single axial pump beam is not a viable option because of its low pumping efficiency.

Two computational tools are available to evaluate the pumping issues; the single region, bounce-average, Fokker-Planck Code,[3.6-5] and Matsuda's multi-region, bounce-average, Fokker-Planck Code.[3.6-6] The first code includes the physics of neutral-beam injection, charge-exchange, etc., and has been used to evaluate conditions in tandem mirror anchors,[3.6-7] especially those in the anchor of TMX-U.[3.6-8] The code cannot, however, be used to evaluate the effects of multiple regions. Matsuda's code, on the other hand, can handle multiple regions but cannot (at this time) handle the trapping of neutral beams. It is being upgraded to permit analysis of the full problem.

The pumping physics of anchor and transition regions is quite different. In the barrier, potentials are affected by the presence of hot electrons and by the difference in T_e between the central side and plug side. In addition, the sloshing neutral beams contribute significantly to the pumping

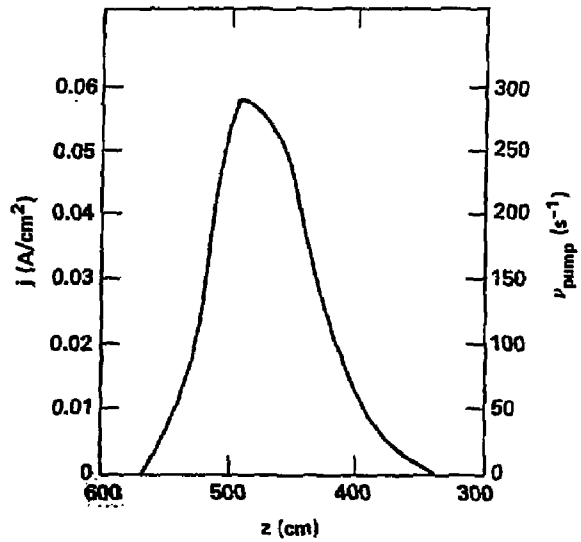

Fig. 3.6-1. Current density and pumping frequency of a single 18^{o} pump beam. Values on axis are plotted.

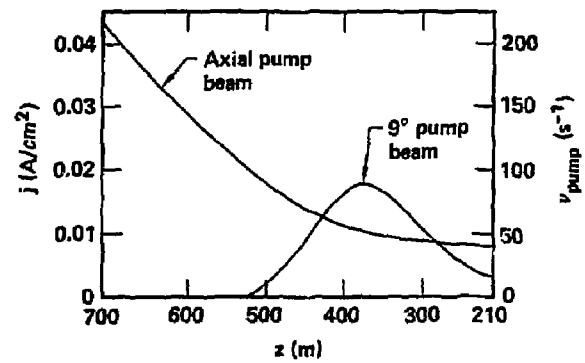

Fig. 3.6-2. Current density and pumping frequency of a single 9^{o} and an axial pump beam. Values on axis are plotted.

rate. Because the 9° beams and axial beams have only a small effect on the pumping in this cell, the analysis is based partly on a single cell model (bounce-averaged code), including trapping using the 18° beams, and partly upon a double-cell model without neutral beam trapping.

The pumping in the transition section, on the other hand, is affected by the strong pumping in the anchor section. Because of the magnetic geometry the trapping of passing particles first occurs between the high-field throttle coil and the plug-potential peak. The 18° pumping beams remove significant numbers of particles before they are trapped in the transition region. Consequently, a two-cell analysis is required using Matsuda's code. Future work will include more complete physics in both regions using an upgraded multi-region code.

Anchor Pumping. The high-field throttle coil will reduce the passing density in the barrier region from that in TMX-U without throttle coil. At the design potentials, we have

$$\frac{n_{ic}^{passing}}{n_{ic}^{th}} \approx \frac{1}{R}\left(\frac{T_{ic}}{\pi\,\phi_b + T_{ic}}\right)^{1/2} ,$$

with ϕ_b the potential drop from the throttle coil to the barrier. Thus, for a given T_{ic} and ϕ_b, the density ratio drops by about three by inserting the throttle coil.

Futch and LoDestro[3.6.-5] obtained an emperical formula for pumping requirements. Setting their filling rate $dn/dt_F = \nu n_{ia}^{trapped}$ and rearranging terms, one finds the required pumping frequency

$$\nu = \frac{n_{ic}^{pass}}{n\tau_p}\left[C(1 + 0.044\,1\ R)\,\frac{g}{g-1}\right]^{1/0.3} H ,$$

with $n\tau_p = 6.27 \times 10^{11}\ T_{ic}^{3/2}/\ell n\ A$, $g = n_{ia}/n_{ic}^{pass}$, $C = 0.935$ and H is a shape factor. Comparing the two cases R = 4, g = 2 and R = 12, g = 6, we have $\nu(R = 4)/\nu(R = 12) = 2.3\ H(R = 4)/H(R = 12)$. In the absense of shape-factor changes, we thus expect a large decrease in the pumping requirements.

This decrease is offset, in part, by the transition section. If the transition is weakly pumped, it will fill; and the density at the inner anchor mirror becomes close to that at the throttle. The distribution at that point is nearly Maxwellian despite strong pumping in the anchor. (This is an example of the threshold effect discussed in Appendix B.) In this limit, therefore, the throttle coil will offer little advantage for barrier pumping.

Anchor pumping requirements are thus largely determined not by the central-cell passing density but rather by ions that are Yushmanov-trapped between the throttle and the plug potential. Consequently, to significantly reduce the barrier pumping requirements, we must have sufficient pumping in the transition region to reduce the density at the inner anchor mirror well below that at the throttle. The conditions to do this are discussed in the next subsection, Transition Pumping.

For present purposes we make a conservative evaluation of anchor pumping and sloshing-beam requirements by neglecting any enhancement resulting from the throttle coil. The single-region Bounce-Averaged Code is used to determine the density and distribution of particles in the anchor.

The example for $n = 1 \times 10^{13}$ cm^{-3} and $T_i = 1$ keV is shown in Fig. 3.6-3a and b. This example includes 90-A equivalents of sloshing neutral beams and three pump beams ($N_{18} = 3$).

Charge-exchange on background gas was neglected. The required sloshing current, however, is a factor of 2 below that available and even below that required for sloshing-ion experiments on TMX-U.[3.6-9]

The conclusion of these calculations, therefore, is that the available sloshing-ion curent is more (by a factor of 2) than required for operation of TMX-U (throttle coil) at the design parameters. Good anchor pumping can be achieved by three 18° pump beams if the transition is unpumped. When results from the next subsection are included, it is found that two 18° pump beams are sufficient to pump the anchor if the transition is well pumped, e.g., by two 9° pump beams.

Transition Pumping. In the transition region the potential is determined by a Maxwell-Boltzmann factor because there are no hot, magnetically-confined

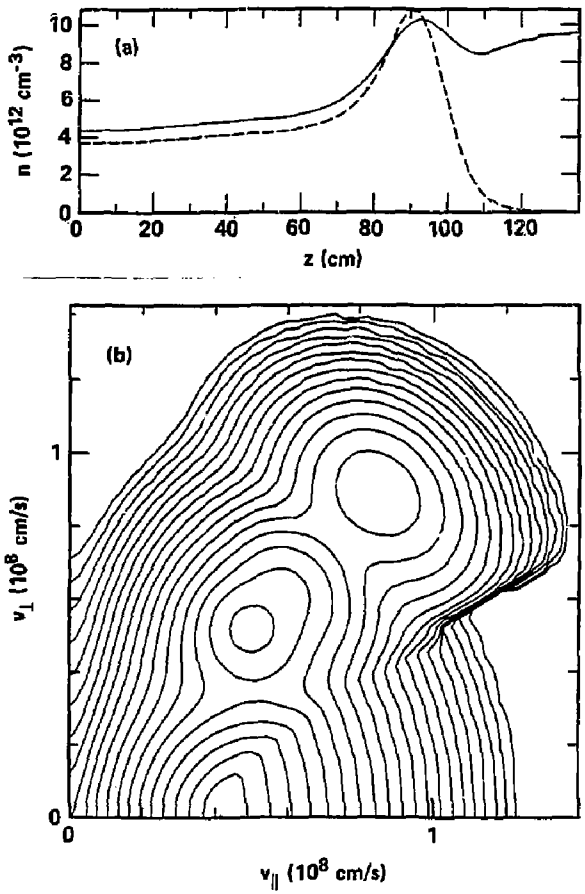

Fig. 3.6-3. Density and distribution of particles for case of TMX-U plug without a throttle coil. (a) Axial density profile. Sloshing neutral-beam current of 90 A and two 18^0 pump beams are used. (b) Phase space at the plug minimum for case in (a).

electrons. For fixed magnetic field and pumping geometry, the density at any point is μ therefore given by

$$n_i/n_{TH} = f[\nu_{ii}, N_{18}, N_g, N_{ax}, T_e/T_i] \quad . \tag{3.6.1}$$

Here the sub/superscript "TH" refers to values at the throttle peak; all other plasma parameters scale from that value. Thus,

$$\nu_{ii}^{TH} = n_{TH} \ln \Lambda/(6.27 \times 10^{11}) \; T_{keV}^{3/2} \quad . \tag{3.6.2}$$

The number of pump beams are given by N_{18}, N_g, and N_{ax}; these determine the axial profile of the pumping rate. Finally, the electrostatic potential is proportional to T_e and thus its net effect depends on the ratio T_e/T_i.

To estimate the effects of the throttle coil, the multi-region code (including a 6-T throttle coil) was run with no sloshing ions from neutral-beam trapping. The results, shown in Fig. 3.6.4, show that the transition and plug are indeed well pumped; this calculation yields $g = n_{ip}/n_i^{pass} = 1.7$, which is considerably less than required.

To evaluate the pumping requirements, Matsuda's multi-region Fokker-Planck code[3.6.-6] was run for several values of N. The magnetic field in the code closely matches that on axis in the transition and anchor sections of TMX-U; the multiple-section phase space is properly handled by the program. The physics of the sloshing ions, magnetically confined electrons, etc., is absent from the code; results, therefore, apply primarily to the transition region. The behavior in the anchor is mocked-up by an axial potential variation that is held constant. In the transition, the potential is given by $T_e \ln (n/n_i^{TH})$; the value and axial shape are obtained by iteration of the converged output.

As noted in the previous section, in the absence of pumping in the transition section, the density at the inner anchor peak is close to that at the throttle and the distribution is close to Maxwellian. An example is shown in Fig. 3.6-5. If the passing distribution is filled in, the anchor pumping requirements in the absence of transition pumping are not significantly improved by the presence of the throttle coil.

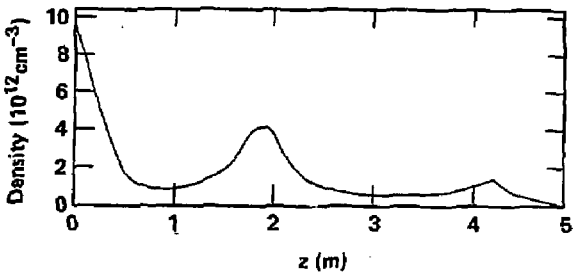

Fig. 3.6-4. Axial density profile for TMX-U with a throttle coil. Pumping by sloshing beams is included but no sloshing ions are trapped.

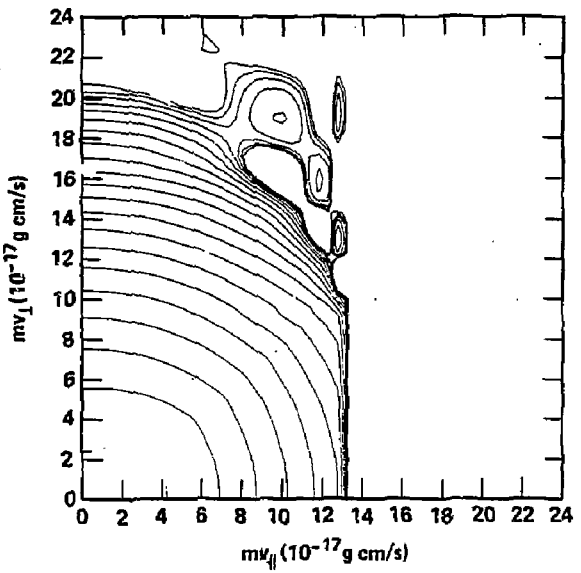

Fig. 3.6-5. Phase space at the plug inner mirror (B = 22 kg) in the absence of transition pumping. Here $n_i^{TH} = 2 \times 10^{13}$ cm^{-3}, T_i (keV, $N_{18} = 3$ and the density at the inner mirror is 1.65×10^{13} cm^{-3}.

An example of moderate pumping in the transition region is shown in Fig. 3.6-6,-7. Note that at the inner mirror the distribution is clearly sloshing. The density at the transition minimum is about 0.32 n_i^{TH}, enough to reduce the instability drive from the transition to a low level. (See Sec. 3.1. on MHD.)

The result of neutral-beam pumping is shown for three different beam configurations in Figs. 3.6-8 through 3.6-10. Each graph shows the total density at the bottom of the transition, n_T, and at the inner mirror, n_i^{in}, normalized to that at the throttle coil; n_i^{TH}, and plotted as a function of the ion-ion collision frequency at the throttle peak.

For the proposed case of $N_{18} = 2$, the density in the anchor is found to "fill-in" at $\nu_{ii}^{TH} > 10^3\ s^{-1}$. This is a ratio of $\nu_{ii}/\nu_{pump} \gtrsim 0.1$ (when weighted with the ratio of pump to anchor lengths), in fairly good agreement with the transition value of 0.2 (see Appendix B) found for a simple square-well model. As this model does not include pumping that is due to the sloshing beams, we conclude that two, 18^0 pump beams provide good barrier pumping at the design parameters.

The result of pumping with $N_{18} = 3$ and $N_{axial} = 1$ is shown in Fig. 3.6-9. The pumping effectiveness in the transition is approximately the same as for $N_9 = 1$. At the highest collision frequencies the pumping is marginal, and we conclude that the configuration is not as effective as $N_{18} = 2$, $N_9 = 1$. The latter case is thus the preferred pumping beam assignment for the throttle coil arrangement of TMX-U.

Central Cell Confinement Time. The pumping of trapped particles causes a corresponding passing-ion loss and thus a reduction in the central-cell confinement time. The effective central-cell confinement time that is due to pumping is

$$(\tau_{ic}^{pump})^{-1} = 2\, j_{trap}\left(\frac{g}{g-1}\right)\frac{1}{en_c L_c}\ , \qquad (3.6.3)$$

where j_{trap} is the trapped current per end and where $g = (n_{pass} + n_{trap})/n_{pass}$ corrects for pumping of both trapped and passing particles. That is, τ_{ic}^{pump}

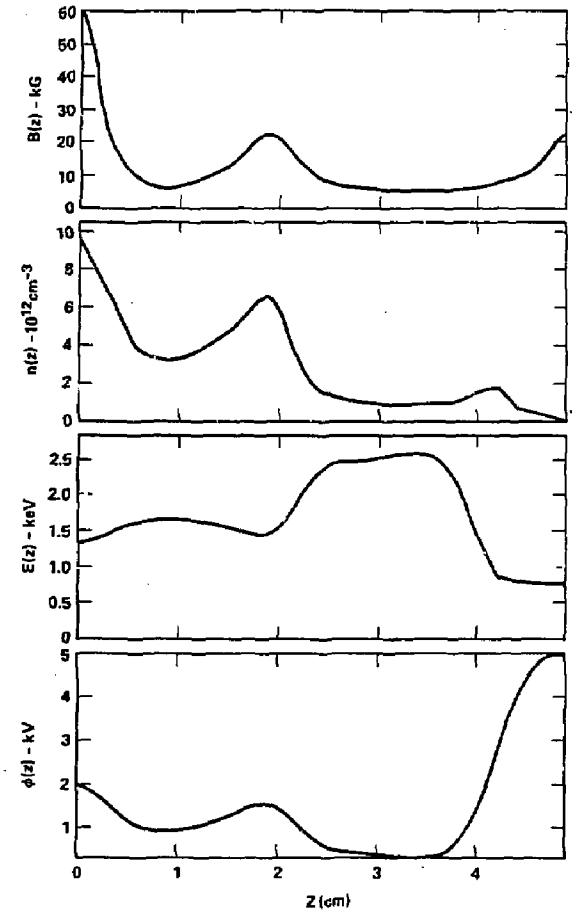

Fig. 3.6-6. Axial profiles for a moderately pumped transition. Here $n_i^{TH} = 1 \times 10^{13}$ cm^{-3}, $T_i = 1$ keV, $N_{18} = 3$, and $N_9 = 1$.

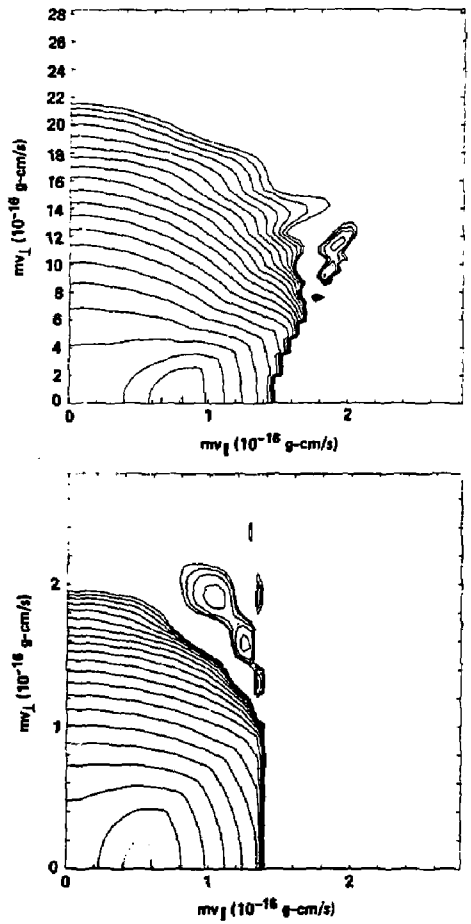

Fig. 3.6-7. Phase space for the case of Fig. 3.6-6. (a) Transition minimum. (b) Plug inner mirror.

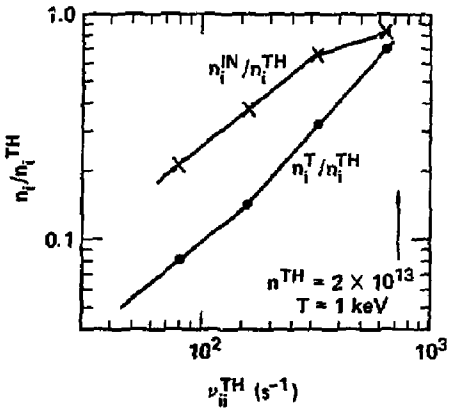

Fig. 3.6-8. Transition pumping for $N_{18} = 3$, $N_9 = 1$, $N_{ax} = 0$ and $T_e = T_i$. Shown are the density at the inner mirror, N_i^{in}, and at the transition minimum, N_iT, normalized to the density at the throttle coil. The densities are plotted against the ion-ion collision frequency at the throttle coil peak. The potential at the barrier is fixed at -1.7 kV below that at the throttle coil. The mass of a deuteron is 3.35×10^{-24} gram.

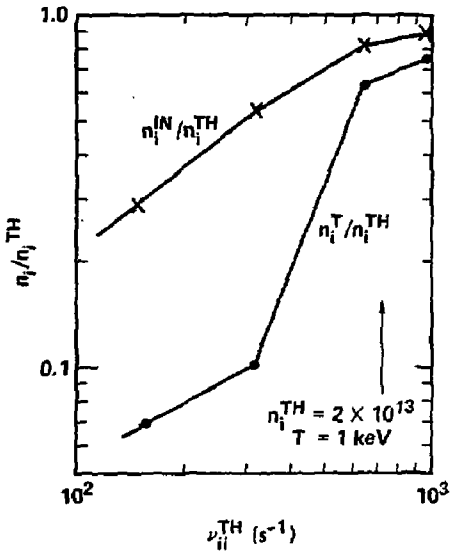

Fig. 3.6-9. Transition pumping for $N_{18} = 2$, $N_9 = 2$, $N_{ax} = 0$, and $T_e = T_i$.

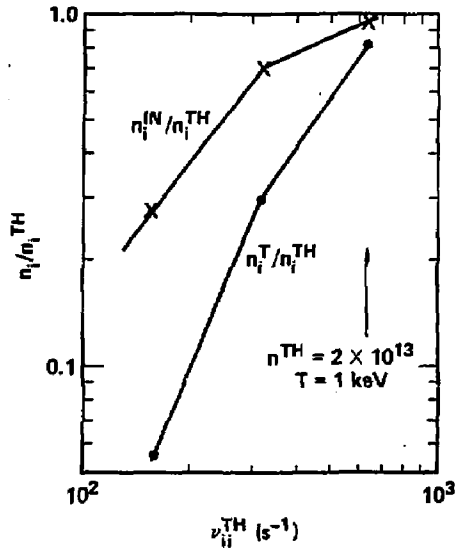

Fig. 3.5-10. Transition pumping for $N_{18} = 1$, $N_9 = 0$, $N_{ax} = 1$, and $T_e = T_i$.

includes not only the pumping losses but the trapping losses of the passing population. Thus, for a two-region end cell (transition plus anchor),

$$j_{trap}\frac{g}{g-1} = \sum_{\substack{i=trans \\ + \\ anchor}} \left[g\ n_{pass} L\bar{\nu}_{pump} \right]_i \ , \qquad (3.6.4)$$

where $g\ n_{pass} = \frac{g}{g-1} n_{trap} = n_{pass} + n_{trap}$.

In Eq. (3.6.4) $L\bar{\nu}_{pump}$ is the charge-exchange pumping rate defined as

$$L\bar{\nu} = B_o \int \frac{d\ell \nu}{B} \ .$$

Integration of the rates shown in Figs. 3.6-1 and -2 yields

$$B_o \int \frac{d\ell}{B}\ \nu_{pump} = \left[6.4 \times 10^3\ N_9 + 1.8 \times 10^4\ N_{18} \right] \text{cm s}^{-1} \ . \qquad (3.6.5)$$

Integration of the sloshing-ion-current density yields

$$B_o \int \frac{d\ell}{B}\ \nu_{pump}^{slosh} = 6.4 \times 10^4 \text{ cm s}^{-1} \qquad (3.6.6)$$

for $I_{slosh} = 90$ A. Estimating $n_{pass} = n_{Th}/(R\sqrt{1+\pi\phi/T})$, $g = 2.5$, $(2<g<3)$, $N_{Th} = 1.2\times10^{13}$, and taking $N_{18} = N_9 = 2$, one finds for Case C that

$$\tau_{ic}^{pump} = 0.13 \text{ s} \ . \qquad (3.6.7)$$

This confinement time is combined in Sec. 2.2 with those for axial and radial losses to yield the total central-cell confinement time.

REFERENCES

3.6.-1. D.E. Baldwin and B.G. Logan, Phys. Rev. Lett. 43, 1318 (1979).

3.6.-2. D.E. Baldwin, "Drift Pumping of Thermal Barriers," Invited paper presented at meeting of Am. Phys. Soc., Div. Plasma Physics, New York (1981).

3.6.-3. B.G. Logan and J. A. Byers, LLNL, unpublished.

3.6.-4. R.S. Devoto, Computational Methods for Mirror Reactors, LLNL Report, UCRL-87149 (1982); submitted to Nuclear Technology/Fusion.

3.6.-5. A. H. Futch and L. L. LoDestro, A Simple Analytical Model for the Collisional Filling Rate in a Potential and Magnet Well, LLNL Report, UCRL-97249 (1982)

3.6.-6. T.A. Cutler, L.D. Pearlstein, and M.E. Rensink, Computation of the Bounce Average Code, LLNL Report, UCRL-52233 (May 23, 1977).

3.6.-7. Y. Matsuda and J.J. Stewart, Bull. Am. Phys. Soc. 27, 1116 (1982).

3.6.-8. M.E. Rensink, Bull. Am. Phys. Soc. 27, 1116 (1982).

3.6.-9. T.C. Simonen et al., submitted to Phys. Rev. Lett.

3.7. DRIFT SURFACES AND ADIABATICITY

J. H. Foote

We have calculated drift surfaces and checked adiabaticity for ions trapped in the three distinctive magnetic-field regions of the throttle-coil configuration: end cell, central cell, and transition region. For the computer calculations summarized here, the particles moved under the constraint of the vacuum magnetic field. We have not included either alterations of the magnetic field arising from plasma diamagnetism (beta effect) or influences of electric fields and particle collisions.

The analysis methods used are summarized in Ref. 3.7-1, where drift-surface and adiabaticity results for the standard TMX-U magnetic-field configuration are given. A more detailed discussion is also presented there. Here we compare the present results for the end and central cells of the throttle-coil configuration with results in Ref. 3.7.-1.

The reflection points for the various orbits calculated are depicted in Fig. 3.7-1. There, R_{eff} is the ratio of the maximum-to-minimum magnetic-field magnitudes experienced by a particle.

End Cell

The end-cell magnet-coil configuration has not been changed from the standard design, so little change in particle trajectories was expected here. Nevertheless, some of the earlier calculations were repeated to check that the changes made in the transition region did not significantly affect the end-cell particle trajectories. This indeed is the case.

Figure 3.7-2 shows the cross section of one of the four calculated drift surfaces for the throttle-coil configuration. This cross section is located at z = 563 cm, the minimum-B position along the magnetic axis. The drift surface is closed and well behaved and is similar to those of the standard configuration (Fig. 8 of Ref. 3.7-1). The drift surface was started on the x-axis at 20 cm and at z = 563 cm, it encircles the magnetic axis, and it has an R_{eff} of 2.00. The other three calculated drift surfaces correspond to R_{eff} values of 1.12, 3.00, and 3.75, and differ only slightly from the one shown. The farthest out radially that any of the four drift surfaces extends

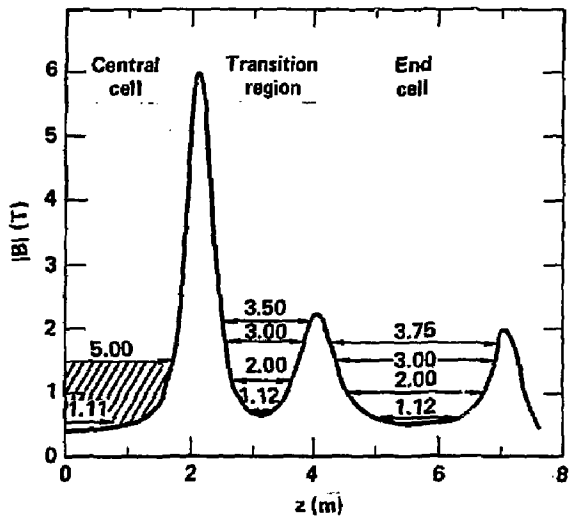

Fig. 3.7-1. Plot of magnetic-field strength on-axis from the midplane of the central cell to beyond the end-cell outer-mirror. The reflection points for the various calculated ion trajectories are depicted. The numbers shown are values of R_{eff}, where R_{eff} is the ratio of the maximum-to-minimum magnetic-field magnitudes experienced by a particle.

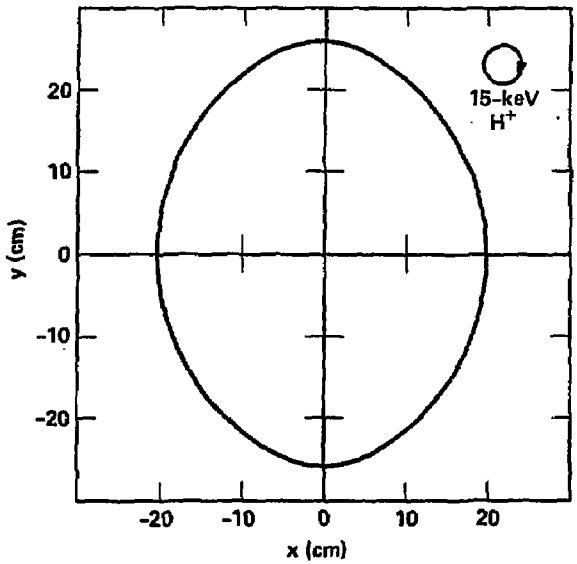

Fig. 3.7-2. Intersection of the calculated drift surface for R_{eff} = 2.00 with the end-cell plane at z = 563 cm (minimum-B position). Also shown is the gyrodiameter for a 15-keV proton at the minimum-B position, with 45° pitch angle there (R_{eff} = 2.00).

Transition Region

Unlike the end-cell and central-cell regions, the shapes of the plasma cross sections on the two sides of the transition-region midplane (away from and toward the central cell) are not similar, even with a 90° rotation about the magnetic axis. The cross section is highly elliptical toward the end cell and less elliptical near the throttle coil, which tends to circularize it there. One would thus expect results for drift surfaces and adiabaticity to differ from those obtained in the other magnetic-field regions and that is what we find.

We calculated drift surfaces for the four different values of R_{eff} shown in Fig. 3.7-1, starting ions at z = 315 cm (position of minimum-B on-axis) and at radii of 10 cm along the x-axis and at 22 cm along the y-axis. These starting positions correspond to the mapping of magnetic-field lines from points in the end cell at z = 563 cm and r = 15 cm. The particles starting with R_{eff} = 1.12 rapidly moved to the wall. But, according to J.A. Byers,[3.7.-2] the presence of electric fields in the transition region will create $\underset{\sim}{E} \times \underline{B}$ rotation that closes the drift surfaces for these deeply trapped particles. The calculated drift surfaces for the other three values of R_{eff} are closed and without excessive ellipticity (maximum ratio of major axis to minor axis lengths at the z = 315 plane is 1.4). For comparable particle energy, the Δr jumps at reflection for these drift surfaces are greater by only a factor of up to 1.6 than those in the central cell of the standard configuration.

We calculated detailed trajectories to estimate loss lifetimes from nonadiabatic behavior for ions that become trapped in the vacuum magnetic field of the transition region with various midplane pitch angles there. To enhance the nonadiabatic jumps in the calculations, energetic 15-keV D^{+} were followed. The ion starting at z = 315 cm, x = 0, and y = 22 cm, with 71° pitch angle (R_{eff} = 1.12), escaped the transition region in 21 μs. The R_{eff} = 3.00 particle (35° pitch angle, i.e., toward the loss cone) had magnetic-moment jumps of a magnitude that led to a calculated lifetime of about 1.0 ms. The trajectories with intermediate R_{eff} values gave much longer τ_{ad} times.

These drift-surface and adiabaticity calculations suggest that we cannot depend on particle drifts to pump out the transition region. The drift

(at z = 563 cm) is 26 cm along the y axis (as compared with 31 cm for the standard configuration). Drift surfaces with the same four values of R_{eff} but starting at 25 cm instead of 20 cm are also closed for the throttle-coil design, while for the standard configuration the two starting at 25 cm with lowest values of R_{eff} open up into banana shapes. Thus, the end-cell drift surfaces appear even better behaved than before.

Figure 3.7-3 shows calculated end-cell adiabaticity results. Lifetimes for loss from nonadiabatic behavior are plotted there for protons with various energies and with $R_{eff} = 2.0$ (corresponding to injected sloshing ions). The plot is taken from Ref. 3.7.-1 for the standard design, with two newly calculated values (at 30 and 120 keV) added for the throttle-coil configuration. As expected, little change is found. If anything, the new configuration is slightly more adiabatic.

Central Cell

The main purpose for installing the throttle coils is to produce an axisymmetric magnetic field in the central cell with reduced radial transport. We have calculated a series of drift surfaces for ions trapped in the central cell, with pitch angles at the midplane ranging from near 90^0 to near the loss cone. As anticipated, the radial jumps of the particles at reflection are much reduced in magnitude compared with the standard design: the peak Δr for the throttle-coil configuration is about 2% of that for the standard design, other conditions remaining the same. This large reduction is in addition to that already obtained with the magnetic ramp of the standard design (those results shown in Fig. 14 of Ref. 3.7-1).

Because adding the throttle coils shortens the central-cell length, one might expect particles trapped in the central cell to be less adiabatic with the shorter length available for |B| to change. But our trajectory calculations show particles with midplane pitch angles in the range of the injection angles of the energetic neutral heating beams to be more adiabatic for the throttle-coil configuration than for the standard. Evidently dB/dz versus z is smoother in the throttle-coil design even though dB/dz is larger in magnitude. Figure 3.7-4, taken from Ref. 3.7-1, shows the standard-configuration results (circles) as well as two values of adiabatic lifetime calculated for the throttle-coil configuration (triangles). In either design, the particles are highly adiabatic.

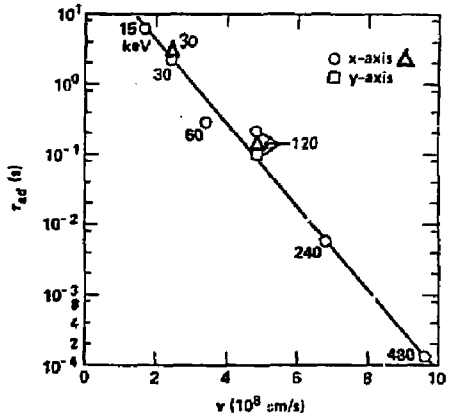

Fig. 3.7-3. Adiabatic lifetime τ_{ad} versus velocity v for protons confined in the TMX-U end cell [for standard design (circles and square) and throttle-coil design (triangles)]. Proton energies in kiloelectron volts are shown. Starting points are at 15 cm along the x- or y-axis, at z = 566 cm for the standard design and 563 cm for the throttle-coil design. To approximately apply these results to D^+, divide the velocity scale and the energy values by a factor of two.

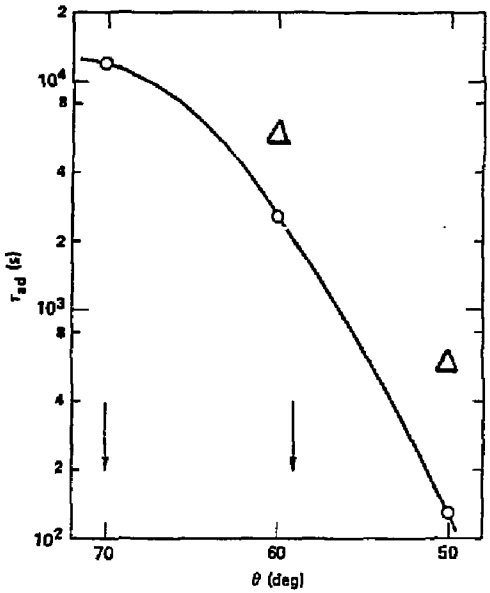

Fig. 3.7-4. Adiabatic lifetime τ_{ad} versus pitch angle θ at the central-cell midplane for 15-keV protons confined in the TMX-U central cell (at a 20-cm midplane radius). The circles are for the standard design and the triangles for the throttle-coil design. The two arrows show the angles (59^{o} and 70^{o}) at which the central-cell heating beams are injected.

surfaces do not appear that distorted, especially when one includes the $\underset{\sim}{E} \times \underset{\sim}{B}$ rotation in addition to the vacuum-magnetic-field effects. Also, the lifetimes against nonadiabatic loss will probably be longer than those calculated above because the ion energy expected is near 1 keV instead of the 15 keV used (leading to smaller magnetic-moment jumps and a longer time between jumps) and because of the tempering effect of the $\underset{\sim}{E} \times \underset{\sim}{B}$ drifts.

REFERENCES

3.7.-1. J.H. Foote, A.K. Chargin, R.H. Cohen, T.B. Kaiser, C.V. Karmendy, T.C. Simonen, and R.L. Wong, TMX Upgrade Magnet System -- Design Characteristics and Physics Considerations, LLNL Report, UCRL-86677 (Nov. 1981), and J. Fusion Energy 2 (6), 385 (1982).

3.7-2. J.A. Byers, LLNL, private communication, based on his previous calculations.

APPENDIX A

PARTICLE- AND POWER-BALANCE FORMULARY FOR THE CENTRAL CELL

D. L. Correll

A.1. Introduction

A series of formulas for the central cell, which describe the ion particle and power accountability within the Fokker-Planck code, are discussed. The electron power balance is analyzed explicitly. These formulas allow central-cell scenarios to be described analytically. The Fokker-Planck code input requires an electron temperature T_{ec}, which was fixed at 0.6 keV (see Sec. A.8), and an ion confining potential ϕ_{ic}, which was set at 2.2 kV. Both T_{ec} and ϕ_{ic} are consistent with the TMX-U proposal values.[A-1] The peak of the confining potential is within the end cell at B = 8.5 kG. The axial variation, used in the code, of the magnetic field and plasma potential for Case C is given in Fig. A-1. The potential is referenced to the central-cell electron potential, ϕ_{ec} = 2.6 kV; the central-cell mirror ratio, $R_c = \frac{60}{4} = 15$; and the mirror ratio at the potential peak, $R_p = \frac{8.5}{3} = 2.1$. All equations are general in nature but when examples are given the numbers refer to Case C of the throttle coil geometry. Figure A-2 summarizes the particle and power balance for Case C.

A.2. Ion-Particle Sources

The neutral beams within the central cell were modeled to have an extraction voltage V_{beam}^{ext} of 15 kV and to be injected at 65° with respect to the magnetic axis. The three beam species associated with D^+, D_2^+, and D_3^+ particles had extracted currents in a 55, 30, 15% ratio with 1.6 atom-amps per power amp. The mean incident-beam energy E_{beam}^{incid} is 9.4 keV with $v_{beam} \approx 10^8$ cm/s for deuterium. If we include the variation in neutralization, energy, velocity, and ionization rate for each species, then the relative neutral-beam source strength, $\nu_{beam}^{ioniz} = n_{beam}\langle\sigma v\rangle^{ioniz}$, for particles at 15, 7.5, and 5 keV is 30, 35, and 35%, respectively. The charge-exchange events to ionization events for beam particles was assumed to be $f_{beam}^{c-x}/f_{beam}^{ioniz} = 2$.

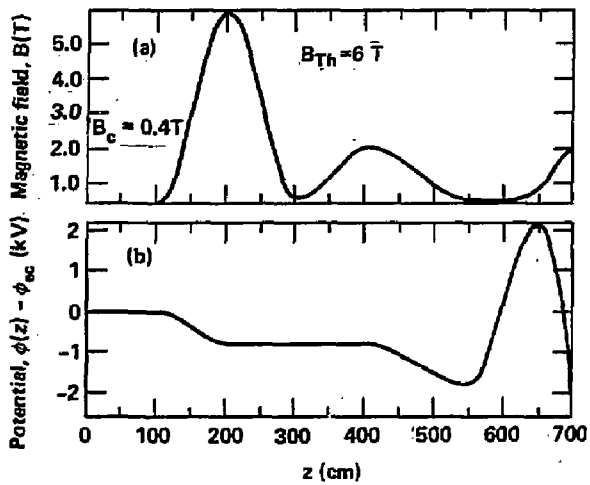

Fig. A-1. Fokker-Planck axial profiles of B and ϕ (Case C).

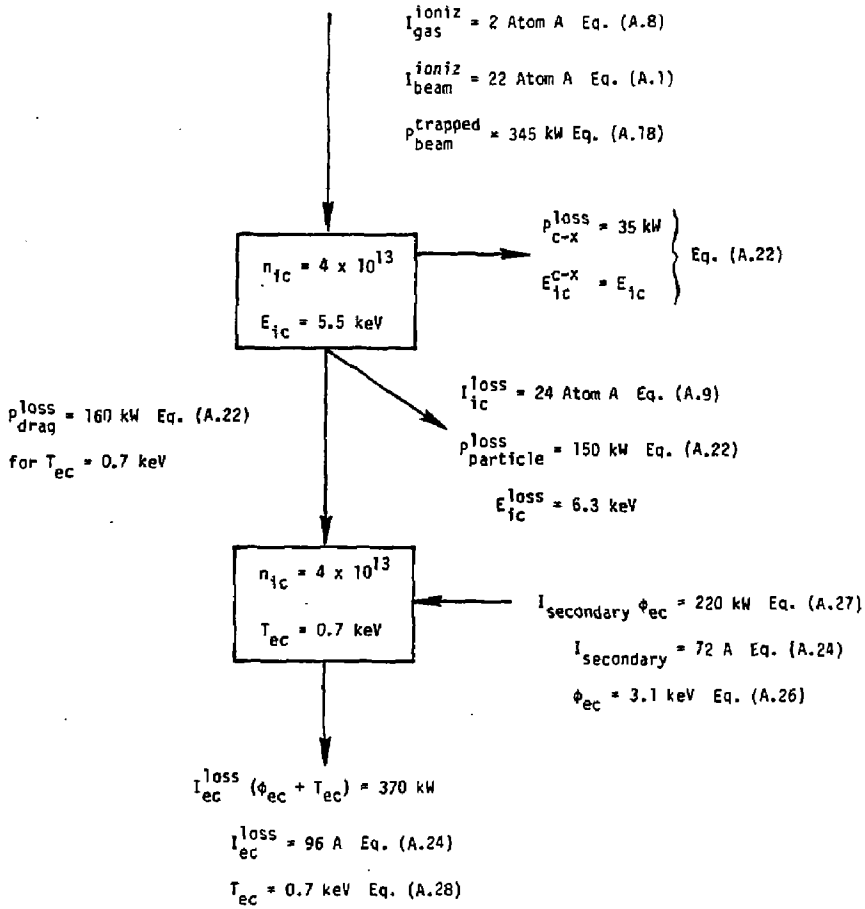

Fig. A-2. Throttle geometry: particle and power balance (Case C).

In terms of the source strength, the ionized beam current,

$$I_{beam}^{ioniz} = \sum_{species} n_c \nu_{beam}^{ioniz} e \frac{1}{3} \pi r_c^2 L_c \, . \tag{A.1}$$

The target density, n_c, is the central cell density ($n_c = n_{ic} = n_{ec}$). For parabolic profiles,

$$n_c(r) = n_c \left(1 - \frac{r^2}{r_c^2}\right) \, . \tag{A.2}$$

The following relationships hold:

$$\int n_c(r) dr = \frac{4}{3} n_c r_c, \tag{A.3}$$

$$\int n_c(r) 2\pi r dr = \frac{1}{2} n_c \pi r_c^2, \tag{A.4}$$

and

$$\int n_c^2(r) 2\pi r dr = \frac{1}{3} n_c^2 \pi r_c^2. \tag{A.5}$$

For the throttle coil, r_c = 17 cm, $L_c = B_c \int \frac{dl}{B_{ioniz}}$ = 260 cm, and $V_c = \pi r_c^2 L_c$ = 2.4 X 10^5 cm^3. For example, given a total ν_{beam}^{ioniz} = 43 s^{-1}, the species mix for 15, 7.5, and 5 keV neutral-beam particles would be 15, 17.6, and 17.6 s^{-1}, respectively. This source strength at n_c = 4 X 10^{13} would imply I_{beam}^{ioniz} = 22 amps. For $f_{beam}^{c-x}/f_{beam}^{ioniz}$ = 2, an accompanying 44 amps of charge-exchange current from the beam would be present, if the plasma was "thin".

For "thick" plasma targets,

$$\frac{\langle \sigma v \rangle^{total} \frac{4}{3} n_c r_c}{v_{beam} \sin\theta_{inj}} >> 1 \, , \tag{A.6}$$

with $\langle \sigma v \rangle^{total} = \langle \sigma v \rangle^{ioniz} + \langle \sigma v \rangle^{c-x}$, the charge-exchange products are modeled to be re-ionized before leaving the plasma. Therefore,

ν_{beam}^{c-x} is set equal to zero. Given $\langle\sigma v\rangle^{ioniz} = 3.6 \times 10^{-8}$ cm$^3 \cdot$ s^{-1}, $f^{c-x}/f^{ioniz} = 2$, $r_c = 28$ cm (core + halo), $\theta_{inj} = 65^0$, and $v_{beam} = 10^8$ cm/s, a thick density according to Eq. (A.6) is

$$n_c^{thick} >> 2.2 \times 10^{13} \text{ cm}^{-3} \quad . \tag{A.7}$$

When neutral-gas sources are used, $\nu_{gas}^{ioniz} = n_{gas} \langle\sigma v\rangle_{gas}^{ioniz}$, which provides a particle source of "zero" energy given by

$$I_{gas}^{ioniz} = n_c \nu_{gas}^{ioniz} e \frac{1}{3} \pi r_c^2 L_c \quad . \tag{A.8}$$

Because the gas source has no directed energy, $\langle\sigma v\rangle_{gas}^{ioniz} = 3 \times 10^{-8}$ cm$^3 \cdot$ s^{-1}. The value of $\langle\sigma v\rangle^{ioniz}$ for the beam source had an additional input from ion-ion ionization collisions, 0.6×10^{-8}, bringing the total for beam ionization up to 3.6×10^{-8} cm$^3 \cdot$ s^{-1}. Again due to the difference in the energy of the two particle sources (gas and beam), the ratio of gas charge-exchange events to ionization for the gas source, $f_{gas}^{c-x}/f_{gas}^{ioniz}$, is 3 rather than the value of 2 for the beam source. Therefore, the total incident neutral-gas current, $I_{gas}^{incid} = 4\, I_{gas}^{ioniz}$. For $\nu_{gas}^{ioniz} = 4$, $I_{gas}^{ioniz} = 2$, and $I_{gas}^{c-x} = 6$ atom amps.

A.3. Ion-Particle Losses

The central-cell ion-particle losses can be calculated from

$$I_{ic}^{loss} = \frac{n_{ic}^2}{(n\tau)_{ic}} \frac{1}{3} eV_c \quad , \tag{A.9}$$

where $V_c = \pi r_c^2 L_c = 2.4 \times 10^5$ cm^{-3} for the throttle geometry and the 1/3 geometry factor comes from Eq. A.5. The central-cell confinement parameter

$$(n\tau)_{ic}^{total} = \left\{ [(n\tau)_{ic}^{axial}]^{-1} + [(n\tau)_{ic}^{radial}]^{-1} + [(n\tau)_{ic}^{pumping}]^{-1} \right\}^{-1} \tag{A.10}$$

or

$$(n\tau)_{ic}^{total} = \left\{ [(n\tau)_{ic}^{axial}]^{-1} + [(n\tau)_{ic}^{passing}]^{-1} \right\}^{-1} \quad . \tag{A.11}$$

Equivalently,

$$\frac{n_{ic}^2}{(n\tau)_{ic}^{total}} = n_{ic}\,\nu_{ic}^{loss} = n_{ic}\nu_{ic}^{axial} + n_{ic}^{passing}\left(\nu_{passing}^{radial} + \nu_{passing}^{pumping}\right) \tag{A.12}$$

For Case C of the throttle coil (see Sec. 2.2), $\nu_{ic}^{axial} = 36$, $\nu_{passing}^{radial} = 90$, and $\nu_{passing}^{pumping} = 360\ s^{-1}$. As discussed in Sec. 2.2, only the passing population for the throttle geometry experiences radial and pumping losses, whereas in the standard geometry the total confined density, n_{ic}, undergoes radial transport from nonsymmetric mirror fields. If the sum of the two terms within the parentheses of Eq. A.12 is defined as $\nu_{passing}$, then Eq. (A.12) can be rewritten as

$$n_{ic}\nu_{ic}^{loss} = n_{ic}\nu_{ic}^{axial} + n_{ic}\nu_{ic}^{passing} \quad , \tag{A.13}$$

where

$$\nu_{ic}^{passing} = \frac{n_{ic}^{passing}}{n_{ic}}\,\nu_{passing} \tag{A.14}$$

and

$$\frac{n_{ic}^{passing}}{n_{ic}} = \left(\frac{n_{ic}^{mirror}}{n_{ic}}\right)\left(\frac{B_c}{B_{mirror}}\right), \tag{A.15}$$

In Case C of Table 2.2-1, $\nu_{passing} = 450\ s^{-1}$. The values for n_{ic} and $n_{ic}(B=B_{Th})$ are 4×10^{13} and $1.2 \times 10^{13}\ cm^{-3}$, respectively. This implies $\nu_{ic}^{passing} = 9$. Knowing that $\nu_{ic}^{loss} = \nu_{beam}^{ioniz} + \nu_{gas}^{ioniz} = 43 + 4 = 47$,

Eq. A.13 substantiates $\nu_{ic}^{axial} = 36$. Using $n\nu = n^2/n\tau$ gives $(n\tau)_{ic}^{total} = 8.6 \times 10^{11}$, $(n\tau)_{ic}^{axial} = 11 \times 10^{11}$, and $(n\tau)_{ic}^{passing} = 40 \times 10^{11}$ $cm^{-3}\cdot s$ for the Case C value of $n_{ic} = 4.0 \times 10^{13} cm^{-3}$. Equation A.9 gives $I_{ic}^{loss} = 24$ atom amps.

A.4. Ion-Particle Balance

Equations A.1 and A.8. for I_{beam}^{ioniz} and I_{gas}^{ioniz} give 22 + 2 = 24 atom amps for Case C, which does indeed equal the result from Eq. A.9 where $I_{ic}^{loss} = 24$ atom amps. The general result for particle balance is

$$I_{ic}^{loss} = I_{beam}^{ioniz} + I_{gas}^{ioniz} \quad , \tag{A.16}$$

with $n\nu = n^2/n\tau$, giving

$$n_{ic} = (\nu_{beam}^{ioniz} + \nu_{gas}^{ioniz})\,(n\tau)_{ic} \quad . \tag{A.17}$$

A.5. Ion-Power Input

The trapped neutral-beam power is calculated from

$$P_{beam}^{trapped} = n_{ic}\,\frac{1}{3}\,V_c \sum_{species} \left[\nu_{beam}^{ioniz} E_{beam} + \nu_{beam}^{c-x}(E_{beam} - E_{ic})\right] \quad . \tag{A.18}$$

For $E_b = 15$, 7.5, and 5 keV, the values for Case C of ν_{beam}^{ioniz} were 13, 15, and 15 s^{-1}, respectively. The values for ν_{beam}^{c-x} are twice the ν_{beam}^{ioniz} values. Equation A.18 gives $P_{beam}^{trapped} = 345$ kW for $E_{ic} = 5.5$ keV. Solving

$$E_{beam}^{trapped} = P_{beam}^{trapped}\left[(I_{beam}^{ioniz})^{-1} + (I_{beam}^{c-x})^{-1}\right] \tag{A.19}$$

gives $E_{beam}^{trapped} = 4.8$ keV. The value of $(n\tau)_{ic}^{Energy}$ is calculated from

$$P_{beam}^{trapped} = \frac{n_{ic}^2 E_{ic}}{(n\tau)_{ic}^{Energy}}\,\frac{1}{3}\,V_c \quad , \tag{A.20}$$

which gives $(n\tau)_{ic}^{energy} \approx 3.3 \times 10^{11}$ cm^{-3} • s and $\tau_{ic}^{energy} = 8$ ms. Knowing $I_{ic}^{loss} = I_{ic}^{trapped}$, Eqs. A.9, A.19, and A.20 imply

$$(n\tau)_{ic}^{energy} = \frac{E_{ic}}{E_{beam}^{trapped}} (n\tau)_{ic}^{total} \left[1 + \frac{f_{beam}^{c-x}}{f_{beam}^{ioniz}} \right]^{-1} . \qquad (A.21)$$

A.6. Ion-Power Losses

The ion population loses power through three channels: ion-electron drag, particle losses, and charge-exchange losses with neutral gas. Charge-exchange events with beam neutrals have already been accounted for in Eq. A.18. Mathematically,

$$P_{ic}^{loss} = \frac{I}{3V_c} \left[\frac{n_{ic}^2 (E_{ic} - \frac{3}{2}T_{ec})}{(n\tau)_{drag}} + \frac{n_{ic}^2 E_{ic}^{loss}}{(n\tau)_{ic}} + n_{ic} \nu_{gas}^{c-x} E_{ic}^{c-x} \right] , \qquad (A.22)$$

where (depending on where the gas is fed and the relative values of τ_{ic} and τ_{gas}^{c-x}) $E_{ic} \leq E_{ic}^{c-x} \leq E_{beam}^{trapped}$ and where $(n\tau)_{drag} = 10^{12} T_e^{3/2}(keV)$ for deuterium.

Recall (see Sec. 2.2.2) for the throttle coil design (Case C) that $\nu_{gas}^{c-x} = 4$ s^{-1}. Gas from neutral-beam sources and/or halo fueling can generate its own power losses through charge-exchange collisions. For now, both additional gas sources are ignored. For Case C parameters of $T_{ec} = 0.6$ keV and $E_{ic} = 5.5$ keV, Eq. A.22 reduces to

$$P_{ic}^{loss}(kW) = 230 + 130 \frac{E_{ic}^{loss}}{E_{ic}} + 35 \frac{E_{ic}^{c-x}}{E_{ic}} .$$

A.7. Ion-Power Balance

The Fokker-Planck code does not output E_{ic}^{loss}, the mean energy carried out by ion particles. By equating Eq. A.22 for P_{ic}^{loss} to either Eq. A.18 or Eq. A.20 for $P_{beam}^{trapped}$, the value of E_{ic}^{loss} that satisfies ion-power balance can be evaluated. Equations A.20 and A.22 give

$$\frac{1}{(n\tau)_{ic}^{Energy}} = \frac{\left(1 - \frac{3}{2}\frac{T_{ec}}{E_{ic}}\right)}{10^{12} T_{ec}^{3/2}} + \frac{E_{ic}^{loss}/E_{ic}}{(n\tau)_{ic}} + \frac{\nu_{gas}^{c-x} E_{ic}^{c-x}}{n_{ic} E_{ic}} . \qquad (A.23)$$

For Case C and for $E_{ic}^{c-x} = E_{ic}$, ion power balance requires

$$\frac{E_{ic}^{loss}}{E_{ic}} = 0.6 \quad ,$$

which gives $E_{ic}^{loss} = 3.3$ keV. This means for $T_{ec} = 0.6$ keV that the 345 kW of trapped neutral-beam power is split between ion-electron drag consisting of 230 kW, direct particle losses consisting of 80 kW, and charge-exchange power losses of 35 kW.

A.8. Electron-Particle and Power Balance.

The electron-particle balance can be described by

$$I_{ic}^{loss} = I_{ec}^{loss} - I_{secondary} \quad , \tag{A.24}$$

where $I_{secondary} = \frac{\lambda}{1-\lambda} I_{ic}^{loss}$, and λ is the secondary emission coefficient.[A-2]

Rewriting Eq. A.24 as

$$I_{ic}^{loss} = (1 - \lambda) I_{ec}^{loss} \quad , \tag{A.25}$$

the following expression can be seen as an equivalent statement of electron-particle balance:

$$(n\tau)_{ic} = \left(\frac{1}{1-\lambda}\right)\frac{1}{2} (n\tau)_{ee} g(R) \frac{\Phi_{ec}}{T_{ec}} \exp\left(\frac{\Phi_{ec}}{T_{ec}}\right) \tag{A.26}$$

with

$$(n\tau)_{ee} = 5 \times 10^8 T_e^{3/2}(\text{keV}) \text{ and } g(R) = \frac{2R + 1}{2R} \ln (4R + 2) \quad .$$

From Fig. 4 of Ref. A.-2, we find for $T_e/\mathcal{E}_{ic}^{end\ wall} = 0.12$ and $\mathcal{E}_{ic}^{end\ wall} = \phi_{ic} + \phi_{ec}$ that $\lambda = 0.75$. Equation A.26 for Case C, with $\lambda = 0.75$, implies

$$\frac{\phi_{ec}}{T_{ec}} \exp \frac{\phi_{ec}}{T_{ec}} = 420, \text{ which gives } \frac{\phi_{ec}}{T_{ec}} = 4.5 \quad .$$

Equation A.24 for $\lambda = 0.75$ and $I_{ic}^{loss} = 24$ atom amps gives 72 atom amps of secondary-electron current, $I_{secondary}$, and 96 atom amps of primary electron-current losses, I_{ec}^{loss}.

Electron-power balance between ion-electron drag input and power output associated with electron end losses is written as

$$\frac{n_{ic}^2 \frac{1}{3} \nu_{ce} \left(E_{ic} - \frac{3}{2} T_{ec}\right)}{10^{12} T_{ec}^{3/2}(keV)} = I_{ec}^{loss} \left(\phi_{ec} + T_{ec}\right) - I_{secondary}\, \phi_{ec} \ ,$$

$$= I_{ic}^{loss} \left(\phi_{ec} + T_{ec}\right) + I_{secondary}\, T_{ec} \ , \qquad \text{(A.27)}$$

with $I_{secondary} = \lambda\ I_{ec}^{loss}$. For the throttle reference case, Eq. A.27 becomes

$$\frac{21 \left(5.5 - \frac{3}{2} T_{ec}\right)}{T_{ec}^{3/2}} = 200\ T_{ec} \ , \qquad \text{(A.28)}$$

which gives $T_{ec} = 0.7$ keV and hence $\phi_{ec} = 3.1$ kV. Both calculated values of T_{ec} and ϕ_{ec} are close enough to the input values of 0.6 and 2.6 to confirm the validity of the ion parameters. However, Eq. A.22 implies that P_{Drag}^{loss} becomes 160 kW, $P_{particle}^{loss}$ becomes 150 kW and $E_{ic}^{loss} = 6.3$ keV.

These new power-balance values along with $T_{ec} = 0.7$ keV are used in Fig. A-2 to summarize the particle and power balance for Case C.

REFERENCES

A.-1. F. H. Coensgen, T. C. Simonen, A. K. Chargin, and B. G. Logan, TMX-U Major Project Proposal, LLNL Report, LLL-Prop-172, (April 1980).

A-2. G. D. Porter, Nucl. Fusion 22, 1279 (1982).

APPENDIX B

THRESHOLD IN NEUTRAL-BEAM PUMPING.

E. B. Hooper, Jr.

To illustrate the existence of thresholds in neutral beam pumping, a simple geometry was considered: a square, magnetic and electrostatic, potential well. Passing particles were trapped by Coulomb collisions and removed by uniform neutral-beam pumping. The pumping rate was varied and a threshold found above which the pumping efficiency increased dramatically. The effect apparently arises when the ion-energy diffusion time to the potential minimum is slower than the pumping rate.

A single region was analyzed by the bounce-averaged code[B.-1] run in the square-well mode (MIDPLANE = 1). An initial example analyzed by Futch had R = 10, T_i = 10 keV, and $n_{TH} = 1.38 \times 10^{14}$ cm^{-3} (sub/superscript "TH" refers to values at the mirror peak). The code was run both with potential $\phi = 10^{-6}$ (essentially $T_e = 0$) and with potential $\phi = T_e$ &n n with $T_e = T_i$. The results are plotted in Figs. B-1 and B-2. Note the sharp change in pumping character at $\nu_{pump}/\nu_{ii}^{TH} \sim 0.15$ ($\nu_{ii}^{TH} = n_{TH}$ &n $\Lambda/6.27 \times 10^{11}$ [T_i (keV)]$^{3/2}$). Futch has seen similar effects in pumping calculations.[B.-2]

From dimensional arguments we know that the trapped density, n_{Tr}, is given by

$$n_{Tr}/n_{TH} = f\ (\nu_{pump}/\nu_{ii}^{TH},\ R,\ T_e/T_i) \quad . \tag{B.1}$$

At low pumping rates the scaling with ν_{pump}/ν_{ii}^{TH} must be linear

$$n_{Tt}/n_{TH} = 1 - n^{pass}/n_{TH} - k\ (\nu_{pump}/\nu_{ii}^{TH}) \quad . \tag{B.2}$$

Comparison of the two cases shows that k is greater when the potential is turned on ($T_e = T_i$) than with zero potential ($T_e = 0$). Apparently the reduction in passing density by the potential opens up more phase space and thus permits larger n_{Tr}.

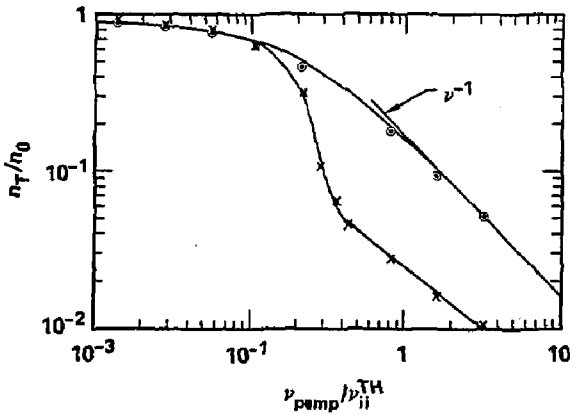

Fig. B-1. Pumping with (circles) and without (x) potential for R = 10, T_e = T_i.

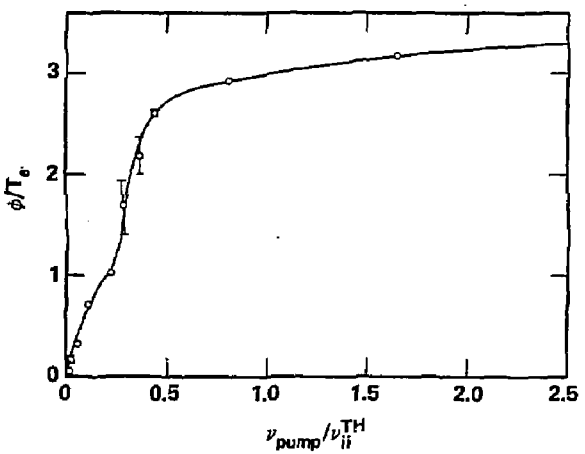

Fig. B-2. Potential for $T_e = T_i$, $\phi = T_e \ln (n/n^{TH})$. Error bars indicate the range of calculations.

At large pumping rates the scaling is given by

$$n_{Tr}/n_{TH} = k_1 \, (\nu_{pump}/\nu_{ii}^{TH})^{-1} \quad , \tag{B.3}$$

as shown, for example, by Futch and LoDestro.[B.-3] In this case, k_1 with $T_e = T_i$ is about 5 times less than with $T_e = 0$.

In the case of zero potential the results may be fitted by a simple model,

$$\frac{dn_{Tr}}{dt} = A\, n_{TH}^2 + B\, n_{TH}\, n_{Tr} - C\, n_{Tr}^2 - \nu_{pump}\, n_{Tr} = 0 \quad , \tag{B.4}$$

where C is found from the requirement that for $\nu_{pump} = 0$, $n_{Tr} + n_p = n_{TH}$. Also $n^{pass}/n_{TH} = 0.053$ for R = 10 and $\phi = 0$, so

$$C = A\, n_{TH}^2/(n_{TH} - n^{pass})^2 + B\, n_{TH}/(n_{TH} - n^{pass}) \, . \tag{B.5}$$

The fit shown has A = 0.174 and B = -0.021. (Note that the computer calculations extrapolate to $n_{Tr} + n^{pass} = 0.975\, n_o$ at $\nu_{pump} = 0$, presumably because of finite gridding or other problems in the code.)

The results for $T_e = T_i$ clearly cannot be fitted by the simple form Eq. B.4. We also tried the model

$$\frac{dn_{Tr}}{dt} = a\, n^{pass\,2} + b\, n^{pass}\, n_{Tr} - c n_{Tr}^2 - \nu_{pump}\, n_{Tr} = 0 \quad , \tag{B.6}$$

with[B.-4]

$$n^{pass}/n_{TH} = \exp\left(\frac{\phi}{T_i}\right) \operatorname{erfc}\left(\frac{\phi}{T_i}\right)^{1/2} - \left(1 - \frac{1}{R}\right)^{1/2} \exp\frac{\phi}{T_i}\frac{R}{R-1} \operatorname{erfc}\left(\frac{\phi}{T_i}\,\frac{R}{R-1}\right)^{1/2} \tag{B.7}$$

and

$$\phi = T_e \, \ell n \frac{n_{Tr} + n^{pass}}{n_{TH}} \, . \tag{B.8}$$

This could not reproduce the threshold effect.

The threshold, therefore, apparently is due to effects in phase space. Figures B-3 and B-4 show the changes (with $T_e = T_i$) of increasing

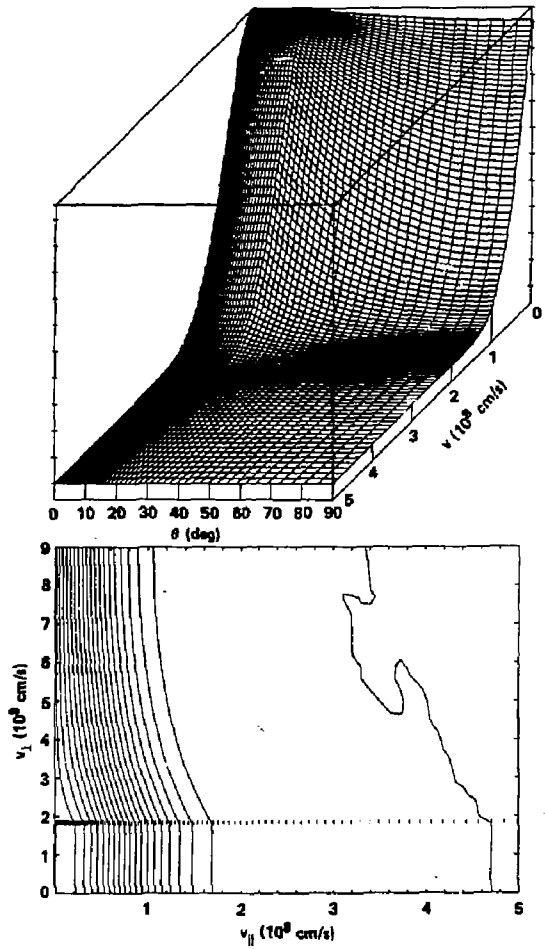

Fig. B-3. Phase space for $\nu_{pump}/\nu_{ii}^{TH} = 0.109$, $T_e = T_i = 10$ keV: (a) $f(v,\theta)$; (b) $f(v,\theta)$ = constant.

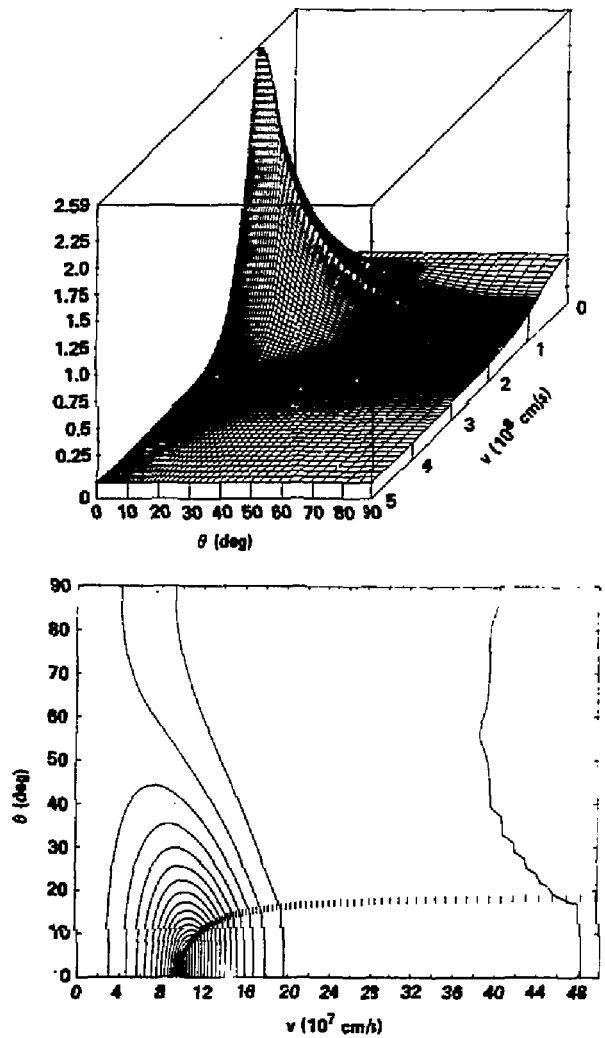

Fig. B-4. Phase space for $\nu_{pump}/\nu_{ii}^{TH} = 0.219$, $T_e = T_i = 10$ keV: (a) $f(v,\theta)$; (b) $f(v,\theta) = \text{constant}$.

ν_{pump}/ν_{ii} from 0.109 to 0.219. In the latter case the potential has increased enough so that the density at low kinetic energy is small, implying that the time for trapped particles to scatter to zero energy is longer than the pumping time.

The effect is illustrated in another way by Figs. B-5 and B-6, both with $\nu_{pump}/\nu_{ii}^{TH} = 0.437$. In Fig. B.5 $T_e = T_i$, and the effect of potential is even more pronounced than in Fig. B.4: The trapped ions are strongly sloshing. In Fig. B-6, $T_e = 0$, and the distribution has filled in to $E = 0$ and $\theta = 90^o$.

LoDestro[B-15] suggested that the drag between counter-streaming passing particles might be playing a critical role in the effect. To test this, we ran an extreme case: $\nu_{pump}/\nu_{ii}^{TH} = 0.0137$, $\phi/T_e = 3$. The result, shown in Fig. B-7, has not completely converged; the density n/n_{TH} of 8.4 is still considerably below $\exp(\phi/T_e) = 20.1$. It is clear that the equilibrium will be filled in. A similar effect is seen for $T_e = T_i$ cases at low pump frequencies when the trap fills up more than in the absence of potential. Interaction between the counter-streaming passing particles undoubtedly is important but is not required for the effect.

REFERENCES

B.-1. T. A. Cutler, L.D. Pearlstein, and M.E. Rensink, Computation of the Bounce-Average Code, LLNL Report, UCRL-52233 (1977).

B.-2. A. H. Futch, LLNL, private communication.

B.-3. A. H. Futch and L.L. LoDestro, A Simple Analytical Model for the Collisional Filling Rate in a Potential and Magnet Well, LLNL Report, UCRL-87249 (1982).

B.-4. R. Cohen, I. B. Bernstein, J. J. Doring, and G. Rowlands, Nucl. Fusion 20, 1421 (1980).

B.-5. L. L. LoDestro, LLNL, private communication.

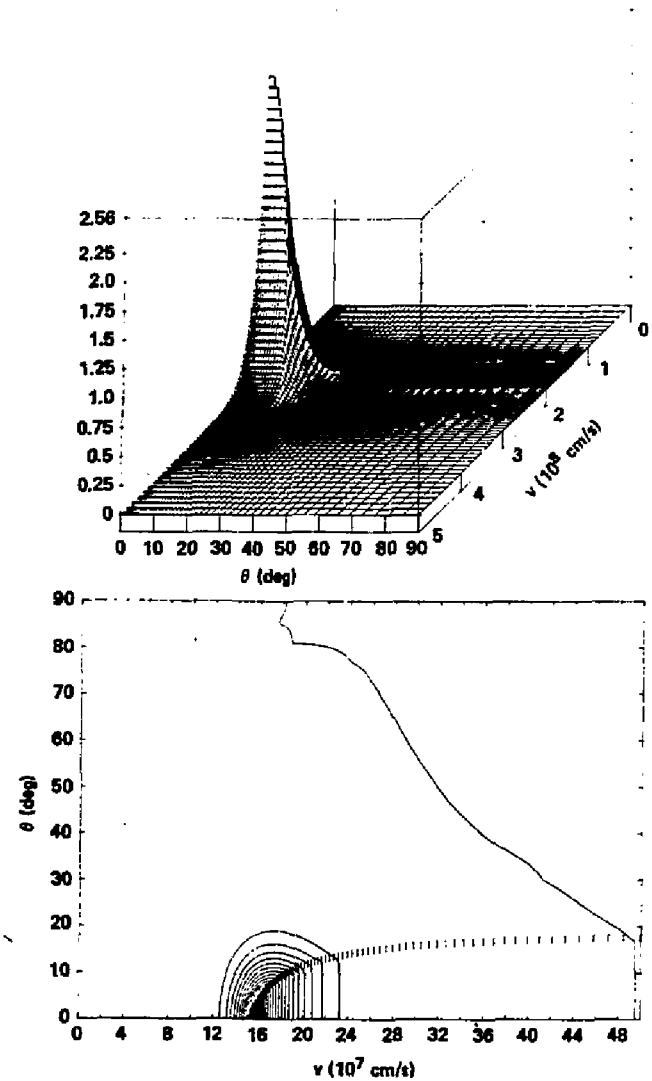

Fig. B-5. Phase space for ν_{pump}/ν_{ii}^{TH} = 0.437, $T_e = T_i$ = 10 keV. (a) $f(v,\theta)$; (b) $f(v,\theta)$ = constant.

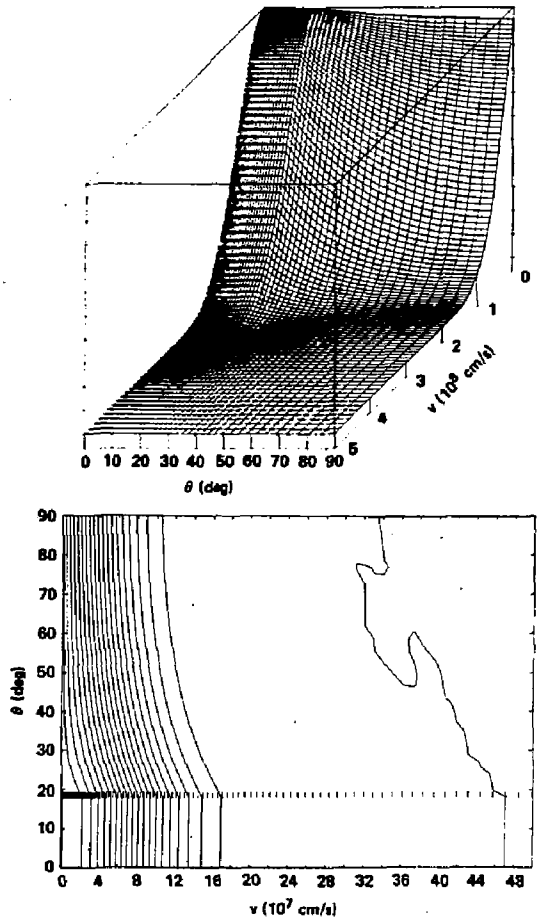

Fig. B-6. Phase space for $\nu_{pump}/\nu_{ii}^{TH} = 0.437$, $T_e = T_i = 10$ keV: (a) $f(v,\theta)$; (b) $f(v,\theta)$ = constant.

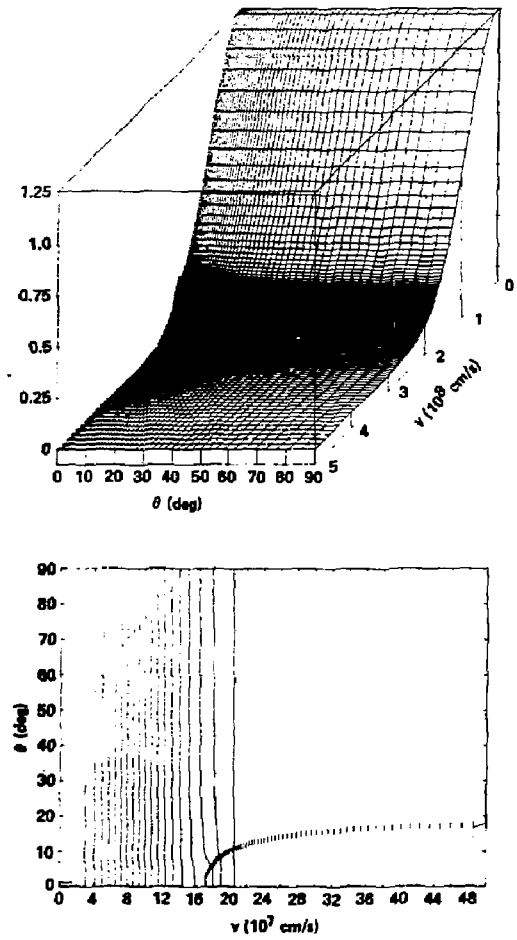

Fig. B-7. Phase space for $\nu_{pump}/\nu_{ii}^{TH} = 0.0273$, $\phi = 3\ T_e$ (numerical calculation not fully converged): (a) $f(v,\theta)$; (b) $f(v,\theta) =$ constant.

APPENDIX C

ALTERNATE PUMPING TECHNIQUES

J. A. Byers, W. F. Cummins, E. B. Hooper, Jr., and B. G. Logan

C.1. Rf Drift Pumping

Investigations are now underway to design a practical means of inducing sufficient controlled amounts of radial diffusion of trapped ions in the transitions to eliminate or reduce the pumping neutral-beam requirements in TMX-U, MFTF-B, and MARS axicell-plug transitions. This section describes a promising adaptation of Baldwin's original drift-pump scheme[C.-1] to the double-quadrupole type of transitions that have been incorporated in these devices. Rf applied near the bounce frequency of particles trapped in the transition and plug can drive strong radial transport, thereby providing good pumping. The resulting pumping technique is now used in the MARS reference case.

Figure C-1 shows axial profiles of the field B, geodesic curvature $\mathcal{K}$, and normal curvature $\mathcal{R}$ for one plug of TMX-U. The drift-pumping scheme relies on the presence of bounce harmonic resonances and exploits the geometric features of the extreme fanning of the flux surfaces that occur in the same z locations as the peaks in the curvatures $\mathcal{K}$, $\mathcal{R}$. Strong z structure (which gives rise to bounce harmonic resonances) appears in the rf field itself, E(z); in the magnetic field through E/B(z); and in the fanning structure of the field lines, $X_0(z)$, $Y_0(z)$.

The following arguments show that the effectiveness of the rf field is maximized when the induced $E_\perp$ vector is aligned parallel to the long direction of the flux surface fan. First, since Faraday's Law gives $E_\perp \cdot dl_\perp = \omega B\, dl_\perp \cdot dz$, we see that the length of the antenna leg, $dl_\perp$, parallel to the $E_\perp$ vector cancels out and so a requirement for a given $E_\perp$ strength is independent of the antenna size in the $E_\perp$ direction. Second, the radial distance from one flux surface to another is shorter across the thin direction of the fan and this results in a larger drift across flux surfaces for a given $E_\perp$ operating at the fanning peak compared to the same $E_\perp$ operating at the midplane circular flux surface. This results in a maximum enhancement factor of about 10 for TMX-U.

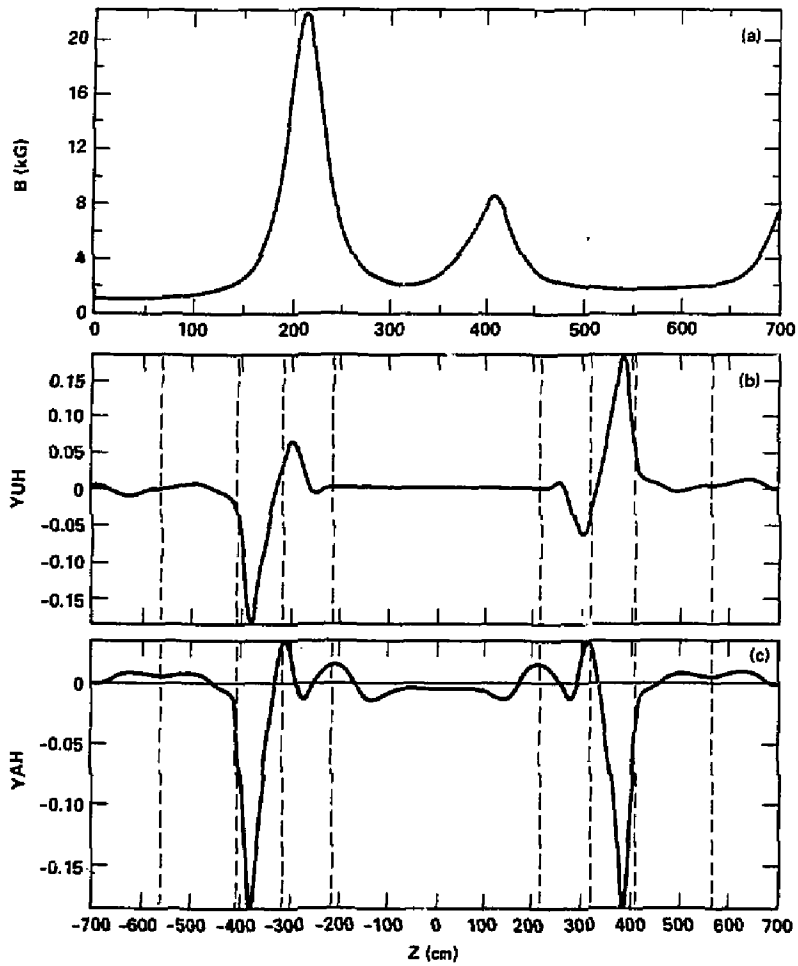

Fig. C-1. Axial profiles for TMX-U with a throttle coil: (a) Magnetic field, (b) geodesic curvature, and (c) normal curvature.

Thus, the rf $E_\perp$ field should have maximum value in the vicinity of the z location of the fanning peaks, and $E_\perp$ should be aligned parallel to the long direction of the fan so as to give $E_\perp/B$ displacements in the thin direction. An optimum coil design has the E field with sizeable value at the curvature (and fanning) peaks, and the orientation of the $E_\perp$ vector smoothly varying from approximately vertical in the vertical fan to horizontal in the horizontal fan. The most effective design would result if the E field could be maintained at peak values at the z location of the fanning peaks (see Fig. C-2).

The drift motion in response to an induced, E-time, varying field exhibits bounce harmonic resonances. Specifically if, for example, the bounce frequency ω_z were a constant independent of radius, an rf E field with $\omega \equiv \omega_z$ would cause a constant radial drift velocity with r(T) increasing linearly in time. The same result would occur if $\omega = n\,\omega_z$ although the strength of the resonant behavior would reduce to negligible strength at some harmonic n = N. The drift pumping idea is to supply an rf signal with frequency at one of these resonances and with sufficient bandwidth to extend over the following:

- The range of bounce frequencies encountered by a single particle in its radial motion, $\Delta\omega_z(r)$.
- The range of bounce frequencies dictated by the total spectrum of pitch angles and energies of the trapped-particle species.

There are further complications when one considers unperturbed motion that also has a azimuthal drift frequency ω_D. Since the rf signal is an M = 1 mode ($E_\perp = E$), the resonant frequencies will then be given by

$$\omega = n\,\omega_z \pm \omega_D \quad .$$

Prior work on the drift pumping concept concentrated on a simplified model with the frequency resonant at the drift frequency (n = 0 above). In that work we derived conditions for stochasticity given a model with $\omega_D(R)$. For a given E field strength, we derived for frequency $\delta\omega$ a condition for the minimum separation necessary between the individual signals to ensure island overlap from one resonant orbit to another. This stochasticity condition was confirmed by the following numerical orbit. The derived diffusion coefficient also checked out to within a factor of 2.

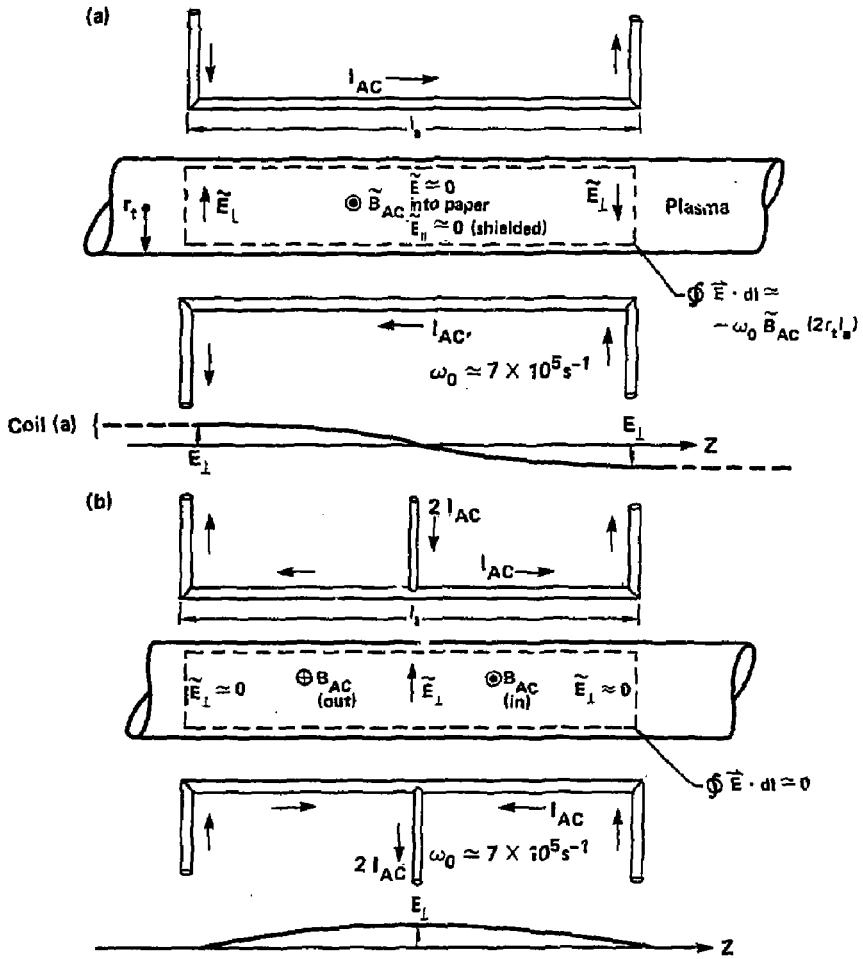

Fig. C-2. Schematic of single (a) and double (b) ac perturbation coils showing induced $\tilde{E}_\perp$.

It seems plausible that we can directly use the results of the prior work for the present case with the replacement of ω_D by ω_z and the replacement of $\tilde{E}^2$ by $\tilde{E}^2/n$, recognizing that the total signal is now roughly evenly divided into n different harmonics and we are resonant only at one.

The $\omega = \omega_D$ result was

$$D_r = \frac{\omega_D^2}{\Delta\omega_D}\left(\frac{\tilde{B}}{B_o}\right)^2 r^2 \quad .$$

generalizing to $\omega = \omega_z$, we now have

$$D_r = \frac{\omega_z^2}{\Delta\omega_z}\left(\frac{\tilde{B}_1}{B_o}\right)^2 L^2 \quad ,$$

where $\tilde{B}$ is the effective amplitude of the first harmonic resonance, and the factor L^2 instead of r^2 comes from the coil geometry (an effect not taken into account previously). We now let $\tilde{B}_1 = \tilde{B}/n$ and also take into account the previously discussed fanning factor enhancement factor, F. These factors combine to give

$$\frac{1}{\tau_{pump}} = \frac{D_r}{r^2} = \frac{L^2}{r^2}\frac{\omega_z^2}{\Delta\omega_z}\left(\frac{\tilde{B}}{B_o}\right)^2 \times \frac{1}{n} \times F \quad .$$

Compared to the prior work, we get an increased pumping rate because of the L^2/r^2 factor, the use of ω_z instead of ω_D, and the fanning enhancement factor F. The factor 1/n represents a reduction from the prior model result. Both the factor 1/n and the fanning factor F are complicated functions of the actual total configuration and have not been quantitatively evaluated yet.

The numerical work to date confirms that bounce resonance harmonics do occur and demonstrates that the fanning can be a strong enhancement. Stochastic orbits were also observed under some conditions. Remaining to be done are first, detailed calculations defining conditions for stochasticity and, second, detailed diffusion measurements using an ensemble of orbits. A preliminary result is that $\tilde{B}/B_o \approx 0.001$ is sufficient for effective pumping, but firm answers must await completion of diffusion studies.

C.2. ICRH Pumping

Description. One alternative to charge-exchange pumping of the transition region is ICRH pumping of the ions trapped between the throttle coil and the positive electrostatic barrier in the anchor cell[C.-2]. Figure C-3 shows the basic configuration for this scheme. Given an asymmetric-mirror configuration wherein the highest magnetic mirror is inboard (toward the central cell) of the electrostatic barrier, a fraction of the trapped ions (primarily electrostatically trapped) have turning points that lie between the inboard mirror peak and the field value of the next highest outboard mirror. If ion-cyclotron resonant zones can be established in the region of these turning points, the $V_\perp$ of this class of particles could be effectively incremented on each axial bounce since $\omega_{ci} >> \omega_{bi}$. In the lower B-field region of these end-cells, this energy increase translates into successive increases in parallel energy until the ions can escape over the electrostatic barrier. One must increment the ion energy by the difference in its turning-point potential and the peak barrier potential.

A velocity space diagram of the transition midplane (Fig. C-4) indicates the desired trapped-ion flow. If a rf diffusion zone is established near the boundary between the trapped and passing ion populations, ions that diffuse along this trajectory are lost from the system. This diffusion must be rapid enough to offset the trapping rate from the passing ions and the thermalization rate of the trapped ions. In the latter case insufficient resonant diffusion merely heats the trapped ions. In addition the resonant

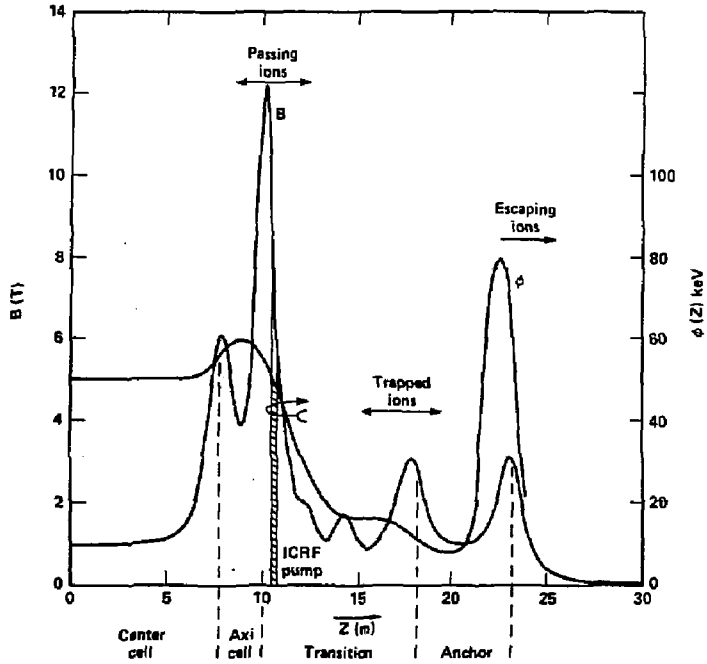

Fig. C-3. Magnetic and electrostatic potential for ICRH pumping showing MFTF-B fields. The TMX-U is similar except for the first (axicell) peak on the left. The ICRH pumping is done on the slope of the throttle field as shown.

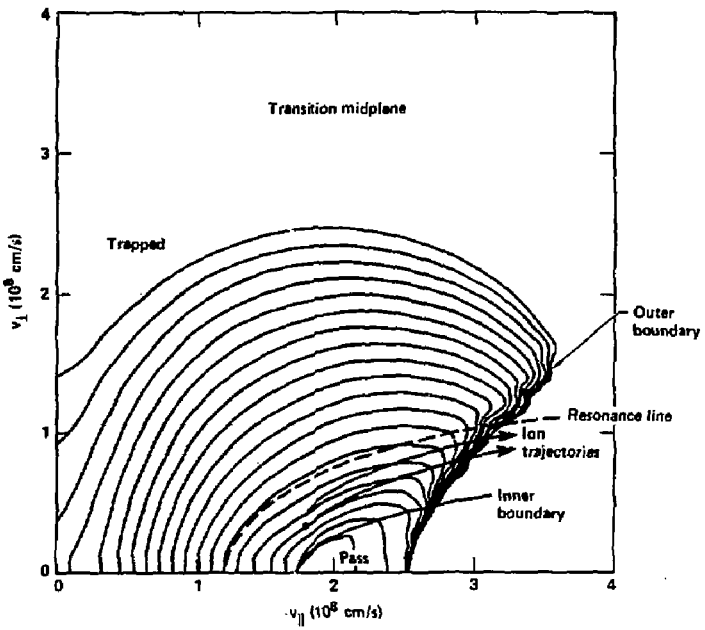

Fig. C-4. Phase space diagram at the transition midplane showing particle trajectories arising from the ICRH.

zone must not overlap or interact excessively with the passing-ion population. Otherwise, these may be trapped or pumped out.

A bounce-average Fokker-Planck code has been used to demonstrate the feasibility of this scheme for MFTF-B parameters.[C.-3] In that situation a power level of 700 W/cm^2 in a resonant zone located at $B(z)/B_{max} = 2/3$ was able to pump 86% of the trapped current. Since there is a slow diffusion of ions through any axially localized pump, some other method is generally required to remove this residual deeply-trapped group.

TMX-U Throttle. A test of this method on TMX-U would be to replace a significant fraction of the transition charge exchange pump with an rf pump. The problem that occurs in TMX-U is that the lower temperatures produce trapping rates for $n_{mirror}^{passing} \simeq 1 \times 10^{13}$ cm^{-3}, which are much greater than for MFTF-B.

Fokker-Planck calculations are being made for TMX-U throttle parameters. While data for a complete set of conditions is not yet available, our initial results, comparing ICRF with sloshing-ion pumping as opposed to sloshing-ion pumping alone, are summarized in Table C-1. There was no additional transition pumping. The pump strength was the same as used in the aforementioned MFTF-B calculations. Plasma parameters were as follows: $n_{passing}^{mirror} = 1.0 \times 10^{13}$, $T_{ec} = 1$ keV, $T_{ic} = 1$ keV, $\Delta\phi_m = 1.7$ keV, $I_{sloshing} = 120$ A, $B_{mirror} = 6.0$ T, and $B_o^{transition} = 0.5$ T. The rf diffusion zone was centered at B_r and was Gaussian with a characteristic length ΔB_r; $\Delta\phi_{mr}$ is the potential drop from the throttle mirror to the resonant zone; and g_b is the usual filling ratio.

Table C-1. Effect of ICRH Pumping on TMX-U with the throttle coil (B_r = 3.5 T, ΔB_r = 0.6 T, $\nu_{cx}^{sloshing}$ = 980 s^{-1}).

Potential drop, $\Delta\phi_{mr}$ (kV)	p_{rt}^{tot} (W/cm^2)	Filling ratio, g_b
0.35	0	4.37
0.35	0.290	4.74
0.96	0	4.64
0.96	0.217	3.05
1.2	0	4.80
1.2	0.198	2.95

The most striking result is the necessity of a minimum potential difference between the mirror and the resonant zone. If there is not such a difference, the diffusion zone begins to overlap the passing-trapped ion boundary near the inner potential cut-off ($v_{\perp i} << v_{\parallel c} \simeq (2e\Delta\phi_{tm}/m)^{1/2}$ in Fig. C-4); thus, feeding on the passing-ion population. This effect was not apparant in previous MFTF-B calculations since the positive, axicell-potential bump always produced a significant potential drop on the transition side.

Further evaluation of this effect in TMX-U with throttle coil will require more precise, self-consistent, potential calculations. However, if one starts up and maintains a well-pumped transition for the ICRF pumping experiment, there should be sufficient $\Delta\phi_{mr}$.

From Table C-1, it can be seen that a significant amount of ICRF pumping can occur with power fluxes of 0.217 kW/cm^2 referenced to the transition midplane. Calculations are continuing as follows:

- To clarify the $\Delta\phi_{mr}$ question.
- To determine optimum pump strength.
- To determine how much transition charge-exchange pumping can be replaced by ICRF for a nominal $g_b \approx 2$.
- To investigate the effect of $2\omega_{ic}$ pumping.

Implementation. For a parabolic density distribution, A power level of 217 W/cm^2 at the center of the plasma translates to 200 kW of absorbed power. Given achievable coupling efficiencies of 50%, a 400-kW rf generator would be required. If the resonant zone is located near the 3.5-T point of the throttle field, the frequencies involved would be 27 MHZ or 54 MHZ, depending on whether $\omega = \omega_{ci}$ or whether $2\,\omega_{ci}$ heating was employed. The latter choice is increasingly appealing because of the effective rf penetration of the plasma and the degree of absorption at $2\,\omega_{ci}$, which occurs when a field and density gradient are present.[C.-4, C.-5]

Diagnostics The primary measurements that relate to this pumping scheme are the following:

- The variation in end-plug parameters ($n_e(z)$, $\phi(Z)$) as rf is substituted for transition charge-exchange.

- *Differential end-loss energy analysis.* This peak should have a low energy cut-off $\sim \phi_b$ and a minimum spread $\sim \Delta\phi_{\Delta\ Br}$. The width should be on the order of the potential differential across the rf resonance zone. There is a spreading which depends on the thermalization rate of the trapped ions as they are being pumped. The portion of the spectrum with energy greater than $\phi_b - \phi_c$ is for passing ions, which are pumped.

Diamagnetic measurements coupled with density measurements in the transition should indicate the power going into trapped (pumped and retained) and passing ions. An increase in ion temperature in the central cell is indicative of the power going into passing ions.

A check should be made for the triggering of anchor instabilities under rf conditions. There will probably be some leakage of rf out of the pumping zone despite care in rf coupler design, particularly along the plasma periphery. This can couple to peripheral rf probes without triggering particularly disruptive instabilities.

REFERENCES

C.-1. D. E. Baldwin, "Drift Pumping of Thermal Barriers," Invited paper presented at meeting of Am. Phys. Soc., Div. Plasma Physics, New York (1981).

C.-2. D. E. Baldwin and B. G. Logan, Physics Basis for an Axicell Design for the End Plugs of MFTF-B, LLNL Report, UCID-19359 (1982).

C.-3. W. F. Cummins, and M. E. Rensink, Bull Am. Phys. Soc. 27 (8), Part II (Oct. 1982).

C.-4. P. L. Colestock and R. J. Kashuba, Bull Am. Phys. Soc. 27 (8), Part II (Oct. 1982).

C.-5. D. Q. Hwang et. al., Bull, Am. Phys. Soc. 17 (8), Part II (Oct. 1982).

U.S. Government Printing Office: 1983/3-687-002/8044